

---

# Effects of electronic correlations in $\text{BaOsO}_3$ and tetragonal $\text{CuO}$

Max Bramberger

---



München 2022



---

# Effects of electronic correlations in $\text{BaOsO}_3$ and tetragonal $\text{CuO}$

Max Bramberger

---

Dissertation  
an der Fakultät für Physik  
der Ludwig-Maximilians-Universität  
München

vorgelegt von  
Max Bramberger  
aus Dachau

München, den 12.05.2022

Erstgutachter: Prof. Dr. Ulrich Schollwöck  
Zweitgutachter: Prof. Dr. Dieter Vollhardt  
Tag der mündlichen Prüfung: 19.07.2022

# Zusammenfassung

Die Bezeichnung *stark korreliertes Material* beschreibt eine Klasse von Materialien, in denen die elektronische Struktur aufgrund von starker Coulomb Wechselwirkung nicht hinreichend durch die Annahme eines nicht-interagierenden Elektronengases beschrieben wird. Aufgrund von Abschirmungseffekten wird die Coulomb Wechselwirkung in typischen Modellen als lokal genähert und steht damit im Konflikt mit dem kinetischen Teil des Hamiltonians. Die aktuell führende Methode zur Behandlung von *stark korrelierten Materialien* ist die dynamische Molekularfeldtheorie (DMFT), die sowohl lokale Wechselwirkungseffekte, als auch nicht lokale kinetische Terme gleichermaßen in Betracht zieht.

Innerhalb dieser Arbeit führen wir unter Verwendung des effektiven Wirkungsformalismus das Konzept von DMFT und ihrer Cluster-Erweiterung, der zellulären dynamischen Molekularfeldtheorie (CDMFT) ein. Des Weiteren diskutieren wir das Konzept der Matrix Produkt Zustände (MPS) und erklären alle Schritte, die notwendig sind, um DMFT Rechnungen mit MPS als Störstellen-Löser durchzuführen. Ausgerüstet mit diesen Werkzeugen untersuchen wir die Effekte elektronischer Korrelationen in  $\text{BaOsO}_3$ , einem Material in dem sowohl Hund's Kopplung als auch Spin-Orbit Wechselwirkung signifikant sind. Wir erforschen das Zusammenspiel dieser Interaktionen mit einer van-Hove Singularität nahe der Fermikante und finden, dass Hund's Kopplung und Spin-Orbit Wechselwirkung miteinander im Wettbewerb stehen. Darüber hinaus verwenden wir CDMFT um die tetragonale Phase des binären Übergangsmetalloxides  $\text{CuO}$  zu untersuchen. Experimente zeigen, dass dieses sich verhält, wie zwei entkoppelte  $\text{CuO}_2$  Subgitter. Wir zeigen, dass diese Entkopplung durch elektronische Korrelationseffekte erheblich verstärkt wird. Ein Vergleich von impulsauflösenden Spektralfunktionen mit winkelauflösenden Photoemissionsspektren (ARPES) zeigt gute Übereinstimmung und stellt die Verbindung zum Experiment her. Durch Verwendung der variationellen Cluster Approximation (VCA) identifizieren wir die Symmetrie des Ordnungsparameters der supraleitenden Phase im lochdotierten Fall und schlussfolgern, dass sich die Entkopplung der Subgitter hindurchzieht bis hin zum supraleitenden Zustand.



# Abstract

The term *strongly correlated material* describes a class of materials in which the electronic structure is not sufficiently described by the assumption of a non-interacting electron gas, due to non-negligible Coulomb repulsion. Due to screening effects these interactions are within typical models approximated to be of local nature, which yields a competition with the non-local kinetic part of the Hamiltonian. To this date the leading method to treat *strongly correlated materials* is dynamical mean field theory (DMFT) as it treats the local interaction and non-local kinetic parts on essentially equal footing.

Within this thesis we introduce the concept of DMFT and its cluster extension cellular dynamic mean field theory (CDMFT) from the effective action formalism. Further, we will discuss the concept of matrix product states (MPS) and all the steps necessary to perform DMFT calculations with MPS as an impurity solver.

Equipped with these tools, we investigate the electronic correlation effects in  $\text{BaOsO}_3$ , a material that features both significant Hund's coupling and spin-orbit coupling. We thoroughly investigate the interplay between those and a van-Hove singularity close to the Fermi level and find a competition between Hund's and spin-orbit coupling. Furthermore, using CDMFT we investigate the tetragonal phase of the binary transition metal oxide  $\text{CuO}$ , which was found to behave as two weakly coupled  $\text{CuO}_2$  sublattices in experiment. We show that this decoupling is significantly enhanced by strong electronic correlation effects. The connection to experimental data is drawn by the comparison of momentum resolved spectra with angle resolved photoemission spectroscopy (ARPES) measurements, which yields good agreement. By the use of variational cluster approximation (VCA) we further identify the symmetry of the superconducting order parameter upon hole doping, concluding that the correlation induced sublattice decoupling even carries over to the superconducting state.



# Publications

On this page you can find a full list of the author's publications in peer reviewed journals and preprint servers [1–5] in inverse chronological order. This thesis is based on the two publications marked with an asterisk (\*).

**Formation of  $\text{CuO}_2$  sublattices by suppression of interlattice correlations in tetragonal  $\text{CuO}$  (\*)**

Max Bramberger, Benjamin Bacq-Labreuil, Martin Grundner, Silke Biermann, Ulrich Schollwöck, Sebastian Paeckel, and Benjamin Lenz  
arXiv:2203.07880 [1]

**$\text{BaOsO}_3$ : A Hund's metal in the presence of strong spin-orbit coupling (\*)**

Max Bramberger, Jernej Mravlje, Martin Grundner, Ulrich Schollwöck, and Manuel Zingl  
Phys. Rev. B. 103, 165133 (2021) [2]

**Open quantum systems in thermal non-ergodic environments**

Carlos A. Parra-Murillo, Max Bramberger, Claudius Hubig, and Inés de Vega  
Phys. Rev. A 103, 032204 (2021) [3]

**$\text{Sr}_2\text{MoO}_4$  and  $\text{Sr}_2\text{RuO}_4$ : Disentangling the Roles of Hund's and van Hove Physics**

Jonathan Karp, Max Bramberger, Martin Grundner, Ulrich Schollwöck, Andrew J. Millis, and Manuel Zingl  
Phys. Rev. Lett. 125, 166401 (2020) [4]

**Dephasing dynamics of an impurity coupled to an anharmonic environment**

Max Bramberger, and Inés de Vega  
Phys. Rev. A 101, 012101 (2020) [5]



# Table of Contents

<b>Zusammenfassung</b>	<b>v</b>
<b>Abstract</b>	<b>vii</b>
<b>Publications</b>	<b>ix</b>
<b>1 Introduction</b>	<b>1</b>
<b>2 Dynamical Mean Field Theory</b>	<b>5</b>
2.1 Effective action formalism . . . . .	5
2.1.1 General framework . . . . .	6
2.1.2 Single particle Green's function as observable . . . . .	7
2.2 Dynamical Mean Field equations . . . . .	8
2.3 Cellular Dynamical Mean Field Theory . . . . .	11
<b>3 Introduction to Matrix Product States</b>	<b>17</b>
3.1 The general concept . . . . .	17
3.2 Density Matrix Renormalization Group . . . . .	20
3.3 Krylov Time Evolution . . . . .	22
3.4 Time Dependent Variational Principle . . . . .	23
3.5 Symmetries . . . . .	27
<b>4 Matrix-Product-State based Impurity Solver</b>	<b>29</b>
4.1 Discretization . . . . .	30
4.1.1 The non-interacting Anderson Impurity Model . . . . .	30
4.1.2 Fitting the Hybridisation . . . . .	32
4.1.3 Block structure . . . . .	36
4.2 Ground State Search . . . . .	37
4.3 Time Evolution . . . . .	39

4.3.1	Degenerate Blocks . . . . .	41
4.3.2	Treatment of degenerate ground states . . . . .	42
4.3.3	Linear Prediction . . . . .	44
4.4	Self-Energy . . . . .	49
4.4.1	The $V$ -Correlator . . . . .	50
4.5	Calculations at fixed impurity occupation . . . . .	51
4.5.1	Tail fitting . . . . .	52
4.6	Analytic Continuation . . . . .	55
4.6.1	Continuation of Green's functions . . . . .	56
4.6.2	Continuation of self-energies . . . . .	58
4.6.3	Continuation of matrix-valued functions . . . . .	59
4.7	A word about interfacing new models . . . . .	60
4.7.1	Additional steps for $SU(2)$ symmetries . . . . .	62
<b>5</b>	<b>BaOsO<sub>3</sub>: A Hund's metal in the presence of strong spin-orbit coupling</b>	<b>65</b>
5.1	Model Hamiltonian . . . . .	66
5.1.1	Basis of total angular momentum . . . . .	69
5.1.2	Computational details . . . . .	72
5.2	Spectral functions . . . . .	73
5.3	Influence of the van-Hove singularity . . . . .	76
5.4	SOC, Hubbard and Hund's physics . . . . .	78
5.4.1	The atomic limit . . . . .	80
5.5	Classification of Phases in the $U$ - $\lambda$ -plane . . . . .	85
5.6	Summary . . . . .	88
<b>6</b>	<b>Formation of weakly coupled sublattices in thin films of tetragonal CuO</b>	<b>91</b>
6.1	Model Hamiltonian . . . . .	93
6.2	Sublattice decoupling . . . . .	95
6.2.1	Exact Diagonalization study . . . . .	97
6.2.2	Non-interacting limit . . . . .	99
6.3	Block construction and cluster orientation . . . . .	101
6.3.1	Block construction . . . . .	101
6.3.2	Cluster Orientation . . . . .	101
6.4	Spectral functions . . . . .	103
6.5	Finite Temperature Analysis . . . . .	105
6.5.1	Details on the estimation of the critical temperatures . . . . .	107

**Table of Contents** **xiii**

---

6.6 Superconductivity upon Hole-Doping . . . . .	108
6.7 Summary . . . . .	110
<b>7 Conclusion and Outlook</b>	<b>113</b>
<b>Acknowledgements</b>	<b>117</b>
<b>Bibliography</b>	<b>121</b>



# Chapter 1

## Introduction

The understanding of the electronic structure of solids is one of the main objectives of condensed matter physics. In situations where the atomic orbitals of a solid's constituents are strongly overlapping, the description of electrons as an essentially non-interacting gas is a reasonable approximation [6]. The nuclei are treated as fixed in space, spanning a periodic crystal structure and thereby contributing a periodic potential in which the electrons can move. Due to this translational invariance, the non-interacting electron gas assumption leads to well-defined bands. That is momentum states that the electrons are allowed to occupy. Starting from the band with the lowest energy, those bands are filled up according to Pauli's exclusion principle [7]. In terms of band structure it is straight forward to define insulators and metals [8, 9]. Namely, a material is insulating if all bands are either full or empty as then it costs a finite amount of energy to excite an electron. On the other hand a metal is a material where there exists a partially filled band. A further improvement of this single-particle description is to take into account the other electrons by the means of a self-consistently determined effective potential, e.g. by density functional theory (DFT) [10–12]. This still yields well-defined bands as DFT treats the problem on an effectively single particle level, which is sufficient to accurately describe many materials [13].

In real materials, the electronic structure consists of many bands most of which are either so favourable in energy, that they get filled up entirely or are so unfavourable that they stay completely empty whether or not electron-electron interactions are considered [14]. However, there may be bands that are partially occupied. If those bands stem from atomic orbitals that are strongly localized, their energy scales may be on par with those from electron-electron interaction as it becomes less favourable for them to delocalize [15]. Materials hosting such bands are called *strongly correlated*

*materials* as it becomes insufficient to only include the electron-electron interaction as an effective potential. When this is the case, the description by DFT may yield qualitatively wrong results, as electron-electron interaction can yield exotic effects like high-temperature superconductivity [16], Mott insulating states [17] and Hund's metallicity [18], which are not captured by band theory. Gaining an insight into the microscopic properties of *strongly correlated materials* is therefore of high interest. To this aim, it is desirable to extract low energy tight-binding models on top of which electron-electron interaction can be included explicitly. This can be achieved, for instance by the means of fitting localized Wannier functions [19] to the dispersion of the bands that are expected to host effects of strong electronic correlations. The extracted tight-binding model will then be an effective model for the orbitals the fitted bands originate from, which may also include contributions from orbitals the correlated orbitals hybridize with, e.g. oxygen p-orbitals.

Upon inclusion of electron-electron interaction, the resulting model can then be solved using Dynamical Mean Field Theory (DMFT) [14, 18, 20, 21]. In typical models for *correlated materials*, one approximates the interaction between electrons to be of local nature due to screening of the Coulomb potential and the small overlap of atomic orbitals with those of the neighbouring atoms [15]. This intrinsic competition between local and non-local degrees of freedom is the reason why models, like the Hubbard model [15, 22, 23], are still not completely solved. DMFT has become one of the most prominent methods to access dynamical quantities of interacting tight-binding models due to treating the non-local kinetic and local interaction degrees of freedom on equal footing [20]. This enables DMFT to capture e.g. the transition from a paramagnetic metal to a Mott insulating state [20, 24] in a half-filled band, which relies on electronic correlations to freeze out the electrons movement [17] and can not be explained within band theory. In particular, the successful combination of the two aforementioned methods (DFT + DMFT) has become the state of the art for electronic structure calculations [14, 21, 25, 26].

DMFT maps the interacting tight-binding model onto an impurity problem, where interactions between electrons are only included on the impurity cluster, while the dynamic exchange with the rest of the lattice is encoded in a bath of free electrons [14, 20]. Even though this problem is already far simpler than the full lattice problem, it is still an interacting many-body problem, which needs to be solved for its interacting single-particle Green's function. This is a very demanding task and therefore the main computational load of DMFT rests on the respective impurity solvers. Common solvers are continuous time quantum Monte Carlo (CTQMC) [27], exact diagonalisation (ED) [28], numerical renormalization group (NRG) [29, 30] and tensor network techniques such as matrix product states (MPS) [31, 32].

In this thesis, we implemented a MPS-based impurity solver working on the imaginary frequency axis [33–36]. The benefits of said solver are that it is able to work exactly at zero temperature without having to deal with a fermionic sign problem [27], a typical problem in CTQMC, while also being able to treat larger system sizes than possible in ED. As the implementation of said solver was a large part of this thesis we introduce the concept of MPS and give a detailed overview of all necessary steps to solve an impurity problem by the use of MPS as an impurity solver.

Further, we investigate the transition metal oxide  $\text{BaOsO}_3$ , which has four electrons in its 5d shell [37]. As the d orbitals are spatially not very extended, the material can be expected to be significantly correlated [15, 18]. Due to crystal field effects [38, 39], only three out of the five bands corresponding to the 5d shell cross the Fermi level, which is why we study an effective three band Hubbard-Kanamori model [22]. Furthermore due to the high principal quantum number, spin-orbit coupling (SOC) is sizeable and can be shown to favour exactly four total angular momentum orbitals [40]. Since the electron’s spin is already accounted for in those orbitals, one expects that large SOC introduces a tendency towards a band insulating state. The reason being that four electrons in four total angular momentum orbitals correspond to a completely filled shell.

In contrast to SOC, Hund’s coupling, a type of electron-electron interaction present in multi orbital Hubbard models, tends to lead to strong correlation effects [18]. This stands in competition with the band insulating state favoured by SOC as the latter is at its core a single-particle effect and therefore expected to show only weak correlation effects. Additionally, in DFT and without the inclusion of SOC we find that the material features a van Hove singularity [41] (vHs) directly at the Fermi surface. The presence of a vHs in the vicinity of the Fermi level leads to a high density of states (DOS) at low energies. This yields a larger active space for correlations, which tends to enhance the effects of the electron-electron interaction. On the other hand SOC splits the vHs and thereby competes with the correlation enhancing effect of the vHs. It is the competition of the vHs, SOC and Hund’s coupling together with the simple cubic structure that makes  $\text{BaOsO}_3$  an interesting material to study.

In addition to  $\text{BaOsO}_3$ , we study a highly symmetric tetragonal phase of  $\text{CuO}$ , which is quite exotic as in its bulk phase  $\text{CuO}$  crystallizes in a lower symmetric monoclinic structure [42]. This situation changes when thin films of  $\text{CuO}$  are grown on a  $\text{SrTiO}_3$  substrate [43–45]. It then crystallizes in its tetragonal phase. The material features well separated 2D layers [44], which yields a 2D character of the underlying physics making tetragonal  $\text{CuO}$  (t- $\text{CuO}$ ) an intriguing candidate to study the mechanisms behind superconductivity in similar cuprate materials [16, 46, 47]. Due to the position of the oxygen atoms, t- $\text{CuO}$  features an unconventional order of the magnitude of

hopping parameters [48]. Namely, the next nearest neighbour hopping is larger than the nearest neighbour one. Within a single layer of t-CuO this introduces a structure of two  $\text{CuO}_2$  sublattices that are intercalated and only connected by the nearest neighbour hopping. In angle resolved photoemission spectroscopy (ARPES) [45] and resonant inelastic x-ray scattering (RIXS) [49] experiments evidence was found that said sublattices are in fact only weakly coupled. Indeed a weak coupling of the sublattices explains why at half filling the material favours stripe order over the usual antiferromagnetic ordering (AFM) that is found in most cuprates [16, 46, 47] as a single layer of t-CuO can then be viewed as two intercalated AFM ordered sublattices, which automatically yields stripe order.

Within this thesis, we discuss what is the origin of this decoupling and how it influences the nature of the superconducting order parameter. To this aim, we consider a single band Hubbard model in Cellular Dynamical Mean Field Theory (CDMFT). CDMFT is an extension of DMFT, which allows to take into account also non-local correlations [50–52], enabling us to investigate the effects the interaction between electrons have on the decoupling of these  $\text{CuO}_2$  sublattices. We find that electronic correlations strongly enhance this decoupling effect and further investigate its robustness by studying the two limiting cases of an isolated cluster as well as the non-interacting case. We compare the spectra obtained from our simulations to the ARPES spectra, confirming the model. Furthermore, using a continuous time quantum Monte Carlo (CTQMC) solver [53–55] we give an estimate towards the critical temperature for the stripe ordering within our cluster calculations. Using Variational Cluster Approximation (VCA) [56–58], a complementary cluster technique, we identify the symmetry of the superconducting order parameter. We find that the sublattice decoupling carries over to the superconducting state and hope that those findings will trigger an experimental effort to dope t-CuO in an attempt to measure its order parameter.

The thesis is structured as follows: In Chap. 2 we give an introduction to DMFT and its cluster extension CDMFT as during the course of this work DMFT was the most prominently used method. In Chap. 3 we give an introduction to the concept of matrix product states (MPS) since our impurity solver is based on MPS techniques. In Chap. 4 we present an in depth discussion of the steps necessary to solve an impurity problem by the use of MPS. Chap. 5 deals with the real material study we conducted on  $\text{BaOsO}_3$ . In Chap. 6 we discuss our results on the weak coupling of sublattices in single layers of tetragonal CuO. Finally, in Chap. 7 we give a summary of the main findings achieved during this work.

# Chapter 2

## Dynamical Mean Field Theory

Due to the simultaneous importance of the non-local and local contributions to typical Hamiltonians of correlated materials the solution of ground state problems and questions about electronic structure are notoriously difficult. Over the last few decades DMFT [14, 20, 50, 51] has proven to be a valuable tool, when it comes to addressing these type of problems. Based on the works of Metzner and Vollhardt [59], Georges *et al.* [20, 60] solved the Hubbard model in infinite dimensions for its local Green's function and proposed that their solution could be modified as an approximate method in lower dimensions. This laid the foundation for DMFT, which treats the kinetic part of the Hamiltonian as coupling to one (or multiple) bands of free electrons, while the interaction is treated exactly on a single site.

In the following we first want to give a motivation for DMFT from the point of view of the effective action formalism, where it can be obtained as approximation to the Baym-Kadanoff functional [61]. This point of view has also been discussed by Kotliar *et al.* [14], where a similar derivation can be found. Afterwards, we are give an overview of the relations that are needed to setup a DMFT self-consistency circle.

### 2.1 Effective action formalism

In this section we are first going to discuss the general framework of the effective action formalism and then apply it using the single particle Green's function as an observable.

### 2.1.1 General framework

We start from the grand canonical potential

$$\Omega = -\ln \left( \int \mathcal{D}\psi \bar{\psi} e^{-S[\psi, \bar{\psi}]} \right) \quad (2.1)$$

for some action  $S$  given in terms of Grassmann fields  $\psi$  and  $\bar{\psi}$ . We can now choose an observable  $A$  and a source  $J$ , such that adding  $J \circ A[\psi, \bar{\psi}]$  to the action yields the generating functional of  $A$

$$\Omega[J] = -\ln \left( \int \mathcal{D}\psi \bar{\psi} e^{-S[\psi, \bar{\psi}] - J \circ A[\psi, \bar{\psi}]} \right). \quad (2.2)$$

Here the  $\circ$  denotes the contraction that is needed to make the term  $J \circ A[\psi, \bar{\psi}]$  a meaningful part of the action, while  $A[\psi, \bar{\psi}]$  denotes the operator given in terms of Grassmann variables, which yields  $A = \langle A[\psi, \bar{\psi}] \rangle_{J=0}$ . We want to stress the difference between  $A$  and  $A[\psi, \bar{\psi}]$  is that the former is an observable while the latter is the corresponding operator.

We can now introduce a Legendre Transformation to obtain a functional of the observable  $A$  instead of the source  $J$

$$\Gamma[A] = \Omega[J[A]] - J[A] \circ A. \quad (2.3)$$

Note that here again the  $\circ$  stands for the necessary contraction between  $J[A]$  and  $A$ , however this time that contraction is different from the one above as now  $A$  is the observable not its corresponding operator. Taking the variational derivative of the above expression with respect to  $A$  we obtain

$$\frac{\delta \Gamma[A]}{\delta A} = \frac{\delta \Omega}{\delta J[A]} \frac{\delta J[A]}{\delta A} - J[A] - \frac{\delta J[A]}{\delta A} \circ A = -J[A] \quad (2.4)$$

The last equality follows from the definition of  $J[A]$  as the source generating  $A$ . This equation tells us that at stationarity of the functional  $\Gamma[A]$  the source  $J[A]$  is equal to zero. We may now write the action as

$$S = S_0 + \lambda S_1 \quad (2.5)$$

with  $S_0$  and  $S_1$  being simple and difficult to treat parts of the action respectively. Here  $\lambda$  is a typical coupling parameter that comes with  $S_1$ , e.g.  $e^2$  for the Coulomb

interaction between electrons. We can carry out an expansion in the parameter  $\lambda$  [14, 62, 63]

$$J = J_0 + \lambda J_1 + \dots \quad (2.6)$$

$$\Gamma = \Gamma_0 + \lambda \Gamma_1 + \dots, \quad (2.7)$$

which yields a simpler reference system

$$\Omega_0[J_0] = -\ln \left( \int \mathcal{D}\psi \bar{\psi} e^{-S_0[\psi, \bar{\psi}] - J_0 \circ A[\psi, \bar{\psi}]} \right). \quad (2.8)$$

The goal is now to determine  $J_0$  such that  $\langle A[\psi, \bar{\psi}] \rangle_{J_0}$  still yields the exact value for  $A$ . We write  $\Gamma[A] = \Gamma_0[A] + \Delta\Gamma[A]$  absorbing all the higher order terms in  $\lambda$  into  $\Delta\Gamma[A]$ . Taking the variational derivative with respect to  $A$  we obtain

$$-J[A] = -J_0[A] + \frac{\delta\Delta\Gamma[A]}{\delta A}. \quad (2.9)$$

Thus, using that at the stationary point of  $\Gamma[A]$  the source  $J[A]$  vanishes, we obtain a set of equations for  $A$  and  $J_0$

$$A = \langle A[\psi, \bar{\psi}] \rangle_{J_0} \quad (2.10)$$

$$J_0[A] = \frac{\delta\Delta\Gamma[A]}{\delta A}. \quad (2.11)$$

Up to here all steps of the derivation were exact. However, obtaining  $\frac{\delta\Delta\Gamma[A]}{\delta A}$  in typical applications is extremely difficult if not impossible. Therefore, the practical approach is to approximate  $\frac{\delta\Delta\Gamma[A]}{\delta A}$  which also yields an approximate solution for  $A$ .

### 2.1.2 Single particle Green's function as observable

Now we want to apply the formalism derived above to the case where we have the action of a typical tight binding model with local interactions

$$S[\psi, \bar{\psi}] = S_0[\psi, \bar{\psi}] + S_1[\psi, \bar{\psi}] \quad (2.12)$$

$$S_0[\psi, \bar{\psi}] = \beta^{-1} \sum_n \sum_{\alpha\nu ij} \bar{\psi}_{i\alpha n} (-i\omega_n \delta_{ij} \delta_{\alpha\nu} + t_{ij}^{\alpha\nu} - \mu \delta_{ij} \delta_{\alpha\nu}) \psi_{j\nu n} \quad (2.13)$$

$$S_1[\psi, \bar{\psi}] = \beta^{-1} \sum_n \sum_i \sum_{\alpha\nu\rho\xi} V_{\alpha\nu\rho\xi} \bar{\psi}_{i\alpha n} \bar{\psi}_{i\nu n} \psi_{i\rho n} \psi_{i\xi n}. \quad (2.14)$$

Here the  $\psi_{i\alpha n} = \psi_{i\alpha}(i\omega_n)$  are the Grassmann variables corresponding to electrons on a site of the lattice denoted by  $i$ , in the active orbital  $\alpha$ , with Matsubara frequency  $i\omega_n$ . The spin was absorbed into the active orbital to not complicate the notation any further.  $\beta$  is the inverse temperature,  $\mu$  the chemical potential,  $t_{ij}^{\alpha\nu}$  the hopping matrix element and  $V_{\alpha\nu\rho\xi}$  the interaction tensor.

In this section we are interested in the single particle Green's function  $G$  as observable. Thus, we identify  $A$  from above with  $G_{i\alpha j\nu}(i\omega_n)$  which is given by

$$G_{i\alpha j\nu}(i\omega_n) = \langle \psi_{i\alpha}(i\omega_n) \bar{\psi}_{j\nu}(i\omega_n) \rangle_{J_0}. \quad (2.15)$$

Now we need to determine  $J_0$  formally as a source that yields the exact  $G$  and contracts with  $\psi_{i\alpha}(i\omega_n) \bar{\psi}_{j\nu}(i\omega_n)$ . Dyson's equation [64] for the self-energy  $\Sigma$  states

$$\Sigma_{i\alpha j\nu}(i\omega_n) = (G_0^{-1})_{i\alpha j\nu}(i\omega_n) - (G^{-1})_{i\alpha j\nu}(i\omega_n). \quad (2.16)$$

Writing  $S_0[\psi, \bar{\psi}] + J_0 \circ A[\psi, \bar{\psi}]$  as

$$S_0[\psi, \bar{\psi}] + J_0 \circ G[\psi, \bar{\psi}] = \beta^{-1} \sum_n \sum_{\alpha\nu ij} \bar{\psi}_{\alpha in} (-G_0^{-1} + J_0)_{i\alpha j\nu}(i\omega_n) \psi_{\nu jn} \quad (2.17)$$

we can identify  $J_0 = \Sigma$ . In the case at hand the functional  $\Gamma(G)$  from last section is the Baym-Kadanoff [61, 65] functional and  $\Delta\Gamma = \Phi$  is the so called interaction energy functional [14]. Neither the functional  $\Phi$  nor its derivative  $\Sigma = \frac{\delta\Phi}{\delta G}$  can be evaluated exactly, however it was shown by Metzner and Vollhardt [59] that in the limit of infinite dimensions the self-energy  $\Sigma$  not only becomes local, meaning

$$\Sigma_{i\alpha j\nu}(i\omega_n) \stackrel{d \rightarrow \infty}{\equiv} \delta_{ij} \Sigma_{\alpha\nu}(i\omega_n) \quad (2.18)$$

but also that all the diagrams contributing to  $\Sigma$  collapse to only consist of local Green's functions, while all other contributions are suppressed by at least an order of  $1/d$  [20, 59]. As the interaction we considered is purely local as well, in the  $d \rightarrow \infty$  limit it therefore suffices to solve a single site problem for its self-energy.

## 2.2 Dynamical Mean Field equations

In the last section we concluded that a single site problem is sufficient to describe the self-energy  $\Sigma(i\omega_n)$  of an interacting tight binding model in infinite dimensions. We therefore define an auxiliary impurity problem with the goal of computing  $\Sigma(i\omega_n)$  by

the action

$$S^{\text{imp}}[\psi, \bar{\psi}] = S_0^{\text{imp}}[\psi, \bar{\psi}] + S_1^{\text{imp}}[\psi, \bar{\psi}] \quad (2.19)$$

$$S_0^{\text{imp}}[\psi, \bar{\psi}] = \beta^{-1} \sum_n \sum_{\alpha\nu} \bar{\psi}_{\alpha n} (-\mathcal{G}^{-1})_{\alpha\nu}(i\omega_n) \psi_{\nu n} \quad (2.20)$$

$$S_1^{\text{imp}}[\psi, \bar{\psi}] = \beta^{-1} \sum_n \sum_{\alpha\nu\rho\xi} V_{\alpha\nu\rho\xi} \bar{\psi}_{\alpha n} \bar{\psi}_{\nu n} \psi_{\rho n} \psi_{\xi n}. \quad (2.21)$$

Note that here  $\mathcal{G}$  is not just the local part of  $G_0$  but some so far unknown function. It is the non-interacting Green's function of the impurity model and often called the *Weiss function* as it mimics the interchange of the single site with the rest of the lattice similar to a *Weiss field* in classical mean field theory [20]. However in contrast to the classical case  $\mathcal{G}$  is a dynamic quantity depending on frequency. From last section we know that it has to be chosen such that the interacting impurity Green's function  $G^{\text{imp}}$  mimics the local interacting Green's function  $G$  of the original model. This means

$$G_{\alpha\nu}^{\text{imp}}(i\omega_n) := \langle \psi_{\alpha n} \bar{\psi}_{\nu n} \rangle_{S^{\text{imp}}} \stackrel{!}{=} \langle \psi_{i\alpha n} \bar{\psi}_{i\nu n} \rangle_S =: G_{i\alpha i\nu}(i\omega_n). \quad (2.22)$$

Here the right side of the equation can be assumed to be independent of the position  $i$  as long as we are considering translationally invariant problems. Unfortunately, in general there is no closed formula to obtain  $\mathcal{G}$  from  $G_0$  without knowing  $G$  or  $\Sigma$ . It can however be determined self-consistently. The idea is to start from some guess for  $\mathcal{G}$  and use it to compute  $G^{\text{imp}}$ . We can then use the Dyson equation of the impurity problem to obtain the impurity self-energy

$$\Sigma_{\alpha\nu}^{\text{imp}}(i\omega_n) = \mathcal{G}^{-1}(i\omega_n) - (G^{\text{imp}})^{-1}(i\omega_n). \quad (2.23)$$

As explained in the last section, when  $\mathcal{G}$  is chosen correctly we should recover the self-energy  $\Sigma$  of the original interacting tight binding model. We can therefore insert it into the Dyson equation (2.23) of the original lattice system and obtain

$$(G^{-1})_{i\alpha j\nu}(i\omega_n) = (G_0^{-1})_{i\alpha j\nu}(i\omega_n) - \delta_{ij} \Sigma_{\alpha\nu}^{\text{imp}}(i\omega_n). \quad (2.24)$$

As we are treating a translationally invariant problem the above is diagonal in momentum space. Thus we apply a Fourier transform and obtain

$$(G^{-1})_{\alpha\nu k}(i\omega_n) = (G_0^{-1})_{\alpha\nu k}(i\omega_n) - \Sigma_{\alpha\nu}^{\text{imp}}(i\omega_n). \quad (2.25)$$

Note that due to its locality, the self-energy is constant in momentum. We may now obtain the local Green's function  $G^{\text{loc}}(i\omega_n)$  of the original lattice problem as

$$G_{\alpha\nu}^{\text{loc}}(i\omega_n) := G_{i\alpha i\nu}(i\omega_n) = \left( \frac{1}{2\pi} \right)^d v_d \int_{\text{BZ}} d^d k \left[ (G_{0k}^{-1} - \Sigma^{\text{imp}})^{-1} \right]_{\alpha\nu}(i\omega_n), \quad (2.26)$$

where we took the continuum limit and  $v_d$  is the volume of the  $d$ -dimensional unit cell. Please note that the matrix inversion corresponds to the orbital indices, while the momentum index is integrated over the first Brillouin zone (BZ). In practice this integral is often approximated by summing up a fine grid of points in the BZ. Having obtained  $G^{\text{loc}}(i\omega_n)$  we can now check for self-consistency by comparing it to  $G^{\text{imp}}(i\omega_n)$ , since when  $\mathcal{G}(i\omega_n)$  did describe the correct single particle problem, then  $G^{\text{loc}}(i\omega_n) = G^{\text{imp}}(i\omega_n)$ . We thus insert  $G^{\text{loc}}(i\omega_n)$  into the Dyson equation of the impurity problem (2.23) and obtain an update for the non-interacting impurity Green's function  $\mathcal{G}(i\omega_n)$

$$\left[ (\mathcal{G}')^{-1} \right]_{\alpha\nu}(i\omega_n) = \left[ (G^{\text{loc}})^{-1}(i\omega_n) + \Sigma^{\text{imp}}(i\omega_n) \right]_{\alpha\nu}. \quad (2.27)$$

In case the updated  $\mathcal{G}'(i\omega_n)$  still shows significant deviations from  $\mathcal{G}(i\omega_n)$  we repeat the above calculation iteratively until  $\mathcal{G}'(i\omega_n) = \mathcal{G}(i\omega_n)$ , in which case the impurity problem mimics the infinite dimensional lattice problem exactly.

For infinite dimensions the above procedure is exact, however it may also approximately be applied for a lattice problem of any dimension [59, 60]. As it turned out this procedure actually reproduces experimental results for real materials very accurately and has become one of the leading methods to include electron-electron interactions on top of existing electronic structure calculations [14, 21, 25, 26].

As a wrap up of this section in Fig. 2.1 we show a pictorial representation of an entire DMFT calculation. First we take a guess  $\mathcal{G}$ . A typical choice would be the non-interacting Green's function of the lattice system  $G_0^{\text{loc}}$ , but also other choices are possible, for example in cases where one wants to investigate whether spontaneous symmetry breaking occurs it might be interesting to initialize  $\mathcal{G}$  in a way that already has a broken symmetry and observe if the latter gets restored over multiple iterations. After the initial guess for  $\mathcal{G}$  was chosen we have to setup the impurity problem. Due to the fact that  $\mathcal{G}(i\omega_n)$  can in principle have any dependence on  $i\omega_n$ , we have to introduce a sufficient amount of degrees of freedom so that this dependence can be captured. The model of choice is often the Anderson impurity model (AIM) [66], which consists of a single site with interactions coupled to a non-interacting bath and is further discussed in Sec. 4.1. Having set up the impurity problem we perform the following steps until we reach convergence:

- a) Solve the impurity problem for  $G^{\text{imp}}$  using the impurity solver of our choice (cf. Chap. 4).
- b) Insert  $G^{\text{imp}}$  into the Dyson equation of the impurity problem (2.23) to obtain the impurity self-energy  $\Sigma^{\text{imp}}$ .

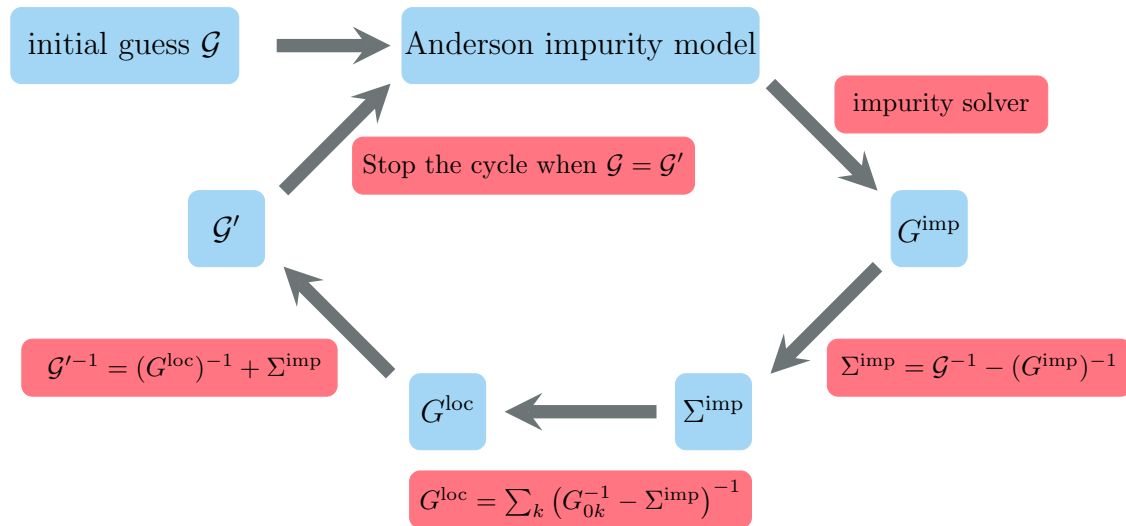


Figure 2.1: Schematic depiction of a DMFT self-consistency cycle. The blue boxes depict the objects that are inputs and outputs of the processes described by the red boxes.

- c) Perform the Brillouin zone integration (2.26) which yields the local Green's function of the lattice system  $G^{\text{loc}}$ .
- d) Identify the local Green's function  $G^{\text{loc}}$  with  $G^{\text{imp}}$  and put it into the impurity problems Dyson equation (2.27) to obtain an update for  $\mathcal{G}$ .
- e) Compare the updated  $\mathcal{G}'$  to  $\mathcal{G}$ . In case they show significant deviations setup a new impurity problem with  $\mathcal{G} \rightarrow \mathcal{G}'$ , then repeat steps a) - d) until  $\mathcal{G} = \mathcal{G}'$ .

Here we want to stress that the solution of the impurity problem (a) is the most time consuming part of the method as the impurity problem is still an interacting many-body problem. It therefore needs to be solved by the means of sophisticated many-body techniques. The method of our choice is a matrix product state (MPS) based impurity solver that is going to be introduced in more detail in Chap. 3 and Chap. 4.

## 2.3 Cellular Dynamical Mean Field Theory

In some situations longer ranged correlation effects may not be negligible after all, for which the standard single site DMFT may be insufficient to accurately obtain

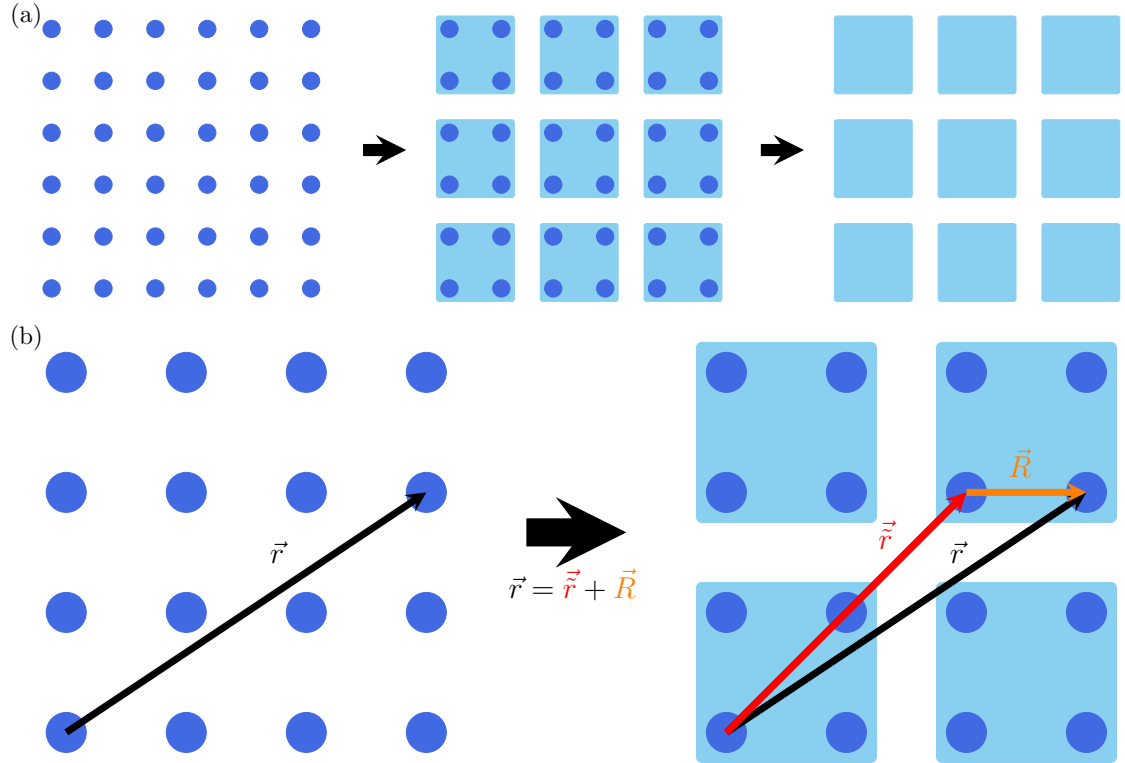


Figure 2.2: Construction of a super lattice consisting of clusters. (a) Graphical depiction of the identification of sets of sites as clusters and interpretation of those as sites on the super lattice. The circles represent the original sites, while sites on the same square form a cluster. (b) Graphical depiction of the unique decomposition of an arbitrary vector  $\vec{r}$  on the original lattice into an super lattice vector  $\vec{r}$  and a cluster vector  $\vec{R}$ .

the local Green's function  $G^{\text{loc}}$  and related observables. The most prominent methods that attempt to remedy this shortcoming are dynamical cluster approximation (DCA) [67, 68] and cellular dynamical mean field theory (CDMFT) [50, 51]. Both treat a cluster of sites as the impurity system instead of just a single site. However, the approach is fundamentally different.

While DCA works on clusters directly in momentum space, therefore fundamentally ensuring the translational invariance of the problem, CDMFT works on real space clusters, which leads to a breaking of translational symmetry that in the end has to be restored by a reperiodisation procedure [69]. The great benefit of CDMFT, however, is that as it works directly in real space, we can choose an arbitrary cluster

geometry. This makes it straight forward to also investigate symmetry broken phases like e.g. antiferromagnetic order without neglecting the non-local fluctuations. Since in the context of this thesis CDMFT was our cluster extension of choice we are going to introduce it here, while for an introduction to DCA we refer the reader to the original works [67, 68] and Ref. [52], a review of quantum cluster methods.

CDMFT can be derived just as DMFT was derived in Sec. 2.1.2 and Sec. 2.2. However, there are a few key differences. For single site DMFT one can show that the mapping to the impurity problem in infinite dimensions corresponds to integrating out all but one site of the lattice [14, 20]. It is the same for CDMFT, with the difference that we have to integrate out the entire lattice apart from one cluster. When considering the hopping matrix  $t_{ij}^{\alpha\nu}$  from Eq. (2.13) this means that the sites contained in the cluster have to be sorted into the local degrees of freedom  $\alpha, \nu$ . This corresponds to a super lattice construction [52], where every site on the super lattice actually is a cluster on the original one. This construction might sound complicated at first, but is actually rather straight forward as schematically shown in Fig. 2.2. The only constraint on the choice of clusters is that it has to be possible to span the full lattice by periodically repeating clusters.

As mentioned before we have to sort the hoppings contained on the cluster into the local degrees of freedom. To this aim we define

$$T_{\tilde{i}\tilde{j}}^{\alpha\nu} = t_{ij}^{\alpha\nu}, \quad (2.28)$$

where we choose  $I$  and  $J$  such that they are indices running over the positions within the cluster  $\vec{R}_I, \vec{R}_J$ , while  $\tilde{i}$  and  $\tilde{j}$  run over the super lattice vectors. This is to say any vector  $\vec{r}_i$  on the original lattice can be uniquely decomposed as  $\vec{r}_i = \vec{r}_{\tilde{i}} + \vec{R}_I$ , which is schematically shown in Fig. 2.2b. We demand that the super lattice is translational invariant, meaning that every cluster is supposed to be identical. Then we can regroup the indices of  $T$  such that  $(\alpha, I), (\nu, J) \rightarrow \alpha, \nu$  where the new  $\alpha, \nu$  now run over orbital as well as positional degrees of freedom as long as the position is contained on the cluster. We can perform a partial Fourier transform on the super lattice degrees of freedom  $\tilde{i}, \tilde{j}$  only, which yields

$$T_k^{\alpha\nu} = \frac{1}{V} \sum_{\tilde{i}\tilde{j}} T_{\tilde{i}\tilde{j}}^{\alpha\nu} e^{-i\vec{k}(\vec{r}_{\tilde{i}} - \vec{r}_{\tilde{j}})} = \sum_{\vec{d}} T_{\vec{d}}^{\alpha\nu} e^{-i\vec{k}\vec{d}}, \quad (2.29)$$

where we introduced the distance vector between clusters on the super lattice  $\vec{d}$  and used that due to translational invariance on the super lattice  $T_{\tilde{i}\tilde{j}}^{\alpha\nu} = T^{\alpha\nu}(\vec{r}_{\tilde{i}} - \vec{r}_{\tilde{j}})$ . Therefore the non-interacting Green's function of the super lattice can be obtained by

$$(G_{0k})_{\alpha\nu} = [(i\omega_n \mathbb{1} - T_k)^{-1}]_{\alpha\nu}. \quad (2.30)$$

Note that here the index  $k$  corresponds to some momentum within the reduced Brillouin zone (RBZ), as the unit vectors of the super lattice are larger than the ones of the original one. The interacting Green's function of the cluster on the original lattice can be obtained analogous to (2.26):

$$G_{\alpha\nu}^{\text{latt}}(i\omega_n) = \left(\frac{1}{2\pi}\right)^d v_d^{\text{SL}} \int_{\text{RBZ}} d^d k [((G_{0k})^{-1} - \Sigma^{\text{cluster}})^{-1}]_{\alpha\nu} \quad (2.31)$$

Note that here the integral again goes over the reduced Brillouin zone, the indices  $\alpha, \nu$  indicate orbital as well as positional degrees of freedom within the clusters and  $v_d^{\text{SL}}$  is the volume of a unit cell on the super lattice. The cluster self-energy  $\Sigma^{\text{cluster}}$  in the above equation has to be computed via mapping the lattice problem onto an impurity model as before. The impurity action is given analogous to (2.19-2.21) by

$$S^{\text{cluster}}[\psi, \bar{\psi}] = S_0^{\text{cluster}}[\psi, \bar{\psi}] + S_1^{\text{cluster}}[\psi, \bar{\psi}] \quad (2.32)$$

$$S_0^{\text{cluster}}[\psi, \bar{\psi}] = \beta^{-1} \sum_n \sum_{\alpha\nu} \bar{\psi}_{\alpha n} (-\mathcal{G}^{-1})_{\alpha\nu}(i\omega_n) \psi_{\nu n} \quad (2.33)$$

$$S_1^{\text{cluster}}[\psi, \bar{\psi}] = \beta^{-1} \sum_n \sum_{\alpha\nu\rho\xi} V_{\alpha\nu\rho\xi} \bar{\psi}_{\alpha n} \bar{\psi}_{\nu n} \psi_{\rho n} \psi_{\xi n}. \quad (2.34)$$

The only difference is that  $\alpha, \nu$  now also run over some positional degrees of freedom contained in the impurity cluster. As the interaction is still local the entire construction has no influence on the shape of  $V$  and therefore there are no non-local components.

Solving the cluster problem in a self-consistent manner, as described for the single-site case in the last section, we obtain the cluster Green's function for the super lattice.

For this rather quick derivation we essentially went back to approximating the Baym-Kadanoff functional [61, 65] by finite ranged self-energies instead of local ones (c.f. 2.18). This same approach is discussed also in the review by Kotliar *et al.* [14], while in Ref. [51] the derivation relies on integrating out all degrees of freedom not contained on the cluster akin to the cavity construction for single site DMFT [20]. We can now attempt to go back to the Green's function of the original lattice  $G(\vec{r}, \vec{r}')$ . To this aim we compute the complete Fourier transform (instead of the partial one from before) of the cluster Green's function  $G(\vec{K}, \vec{K}', \vec{k})$

$$G(\vec{K}, \vec{K}', \vec{k})_{\vec{\alpha}, \vec{\nu}} = \frac{1}{N_C V} \sum_{IJij} G_{i,I,j,J,\vec{\alpha},\vec{\nu}}^{\text{latt}} e^{-i(\vec{K}+\vec{k})(\vec{R}_I+\vec{r}_i)} e^{i(\vec{K}'+\vec{k})(\vec{R}_J+\vec{r}_j)}. \quad (2.35)$$

Here  $\vec{k}$  stands for a super lattice momentum while the  $\vec{K}$  ( $\vec{K}'$ ) are cluster momenta,  $\tilde{\alpha}$  ( $\tilde{\nu}$ ) are orbital degrees of freedom and  $N_C$  is the number of sites per cluster. The reason why we denoted only one super lattice momentum vector is that we explicitly constructed the super lattice to be translationally invariant and therefore the above expression is diagonal in  $\vec{k}$ . This also means that  $G^{\text{latt}}$  does only depend on the distance  $\vec{d} = \vec{r}_j - \vec{r}_i$ , which enables us to reformulate the above as

$$\begin{aligned} G(\vec{K}, \vec{K}', \vec{k})_{\tilde{\alpha}, \tilde{\nu}} &= \frac{1}{N_C V} \sum_{IJi\vec{d}} G_{IJ, \tilde{\alpha}, \tilde{\nu}, \vec{d}}^{\text{latt}} e^{-i(\vec{K} - \vec{K}')\vec{r}_i} e^{i(\vec{K}' + \vec{k})\vec{d}} e^{-i(\vec{K} + \vec{k})\vec{R}_I + i(\vec{K}' + \vec{k})\vec{R}_J} \\ &= \frac{1}{N_C} \sum_{IJi\vec{d}} G_{IJ, \tilde{\alpha}, \tilde{\nu}, \vec{d}}^{\text{latt}} e^{i(\vec{K}' + \vec{k})\vec{d}} e^{-i(\vec{K} + \vec{k})\vec{R}_I + i(\vec{K}' + \vec{k})\vec{R}_J}. \end{aligned} \quad (2.36)$$

In the second step we used that the cluster momenta  $\vec{K}$  and  $\vec{K}'$  are elements of the reciprocal super lattice and therefore the scalar product with an element of the super lattice gives multiples of  $2\pi$ . Resolving the Fourier transform of the super lattice first, this yields

$$\begin{aligned} G(\vec{K}, \vec{K}', \vec{k})_{\tilde{\alpha}, \tilde{\nu}} &= \frac{1}{N_C} \sum_{IJ} \left[ \left( \left( G_{0, \vec{k} + \vec{K}'} \right)^{-1} - \Sigma^{\text{cluster}} \right)^{-1} \right]_{I, J, \tilde{\alpha}, \tilde{\nu}} \\ &\times e^{-i(\vec{K} + \vec{k})\vec{R}_I + i(\vec{K}' + \vec{k})\vec{R}_J}. \end{aligned} \quad (2.37)$$

As the original problem is translationally invariant we would like to obtain a quantity diagonal also in the cluster momenta. However, the clustering introduces a breaking of translational invariance on the original lattice, as effects of electronic correlations are only taken into account within the clusters not between them.

As this spatial symmetry breaking is purely artificial we have to come up with a method to restore the symmetry. The reperiodisation prescription we use was originally proposed by S en echal *et al.* [69] in the context of cluster perturbation theory [52], but can also be applied to CDMFT and other cluster methods [70]. The key idea is to simply discard all matrix elements of  $G(\vec{K}, \vec{K}', \vec{k})_{\tilde{\alpha}, \tilde{\nu}}$  with  $\vec{K} \neq \vec{K}'$ . Using this we obtain

$$\begin{aligned} G(\vec{k})_{\tilde{\alpha}, \tilde{\nu}} &= \frac{1}{N_C} \sum_{IJ} \left[ \left( \left( G_{0, \vec{k} + \vec{K}} \right)^{-1} - \Sigma^{\text{cluster}} \right)^{-1} \right]_{I, J, \tilde{\alpha}, \tilde{\nu}} e^{-i(\vec{K} + \vec{k})(\vec{R}_I - \vec{R}_J)} \\ &= \frac{1}{N_C} \sum_{IJ} \left[ \left( \left( G_{0, \vec{k}} \right)^{-1} - \Sigma^{\text{cluster}} \right)^{-1} \right]_{I, J, \tilde{\alpha}, \tilde{\nu}} e^{-i\vec{k}(\vec{R}_I - \vec{R}_J)}, \end{aligned} \quad (2.38)$$

where we used that for every momentum of the original lattice  $\vec{k}$  there is a unique decomposition in cluster momenta  $\vec{K}$  and super lattice momenta  $\vec{\tilde{k}}$  such that  $\vec{k} = \vec{\tilde{k}} + \vec{K}$ . Eq. (2.38) can now be used to compute, e.g. momentum resolved spectral functions or other observables of interest on the original lattice.

Concluding this chapter we want to stress that in both CDMFT and single-site DMFT the solution of the impurity (cluster) problem is the most cost intensive operation within the self-consistency loop. The optimization of a Matrix Product State (MPS) based impurity solver working on the imaginary frequency axis was a large part of this work. For this reason we want to give an introduction into the workings of said solver. Due to the fact that it is largely based on MPS methods the next chapter will concern itself with an repetition of those, preparing the reader for Chap. 4, where the most important steps of the impurity solver will be explained.

# Chapter 3

## Introduction to Matrix Product States

Even though the impurity problem that is obtained via the mapping introduced by DMFT is far less complicated than the full lattice problem from which it is obtained, it is still a quantum many body problem and as such finding its interacting Green's function  $G(i\omega_n)$  is a difficult task.

As mentioned in Chap. 1, our impurity solver of choice is an MPS-based solver [33–36] on the imaginary frequency axis as it works directly at zero temperature, has no sign problem compared to CTQMC [27] and can tackle rather large impurity systems as compared to ED. Therefore in this section we want to give a short introduction to the main algorithms that are used to obtain  $G(i\omega_n)$ .

### 3.1 The general concept

This section features a rather superficial introduction to the concepts of matrix product states/operators (MPS/MPO). The interested reader may find a more in depth discussion in Ref. [32]. We start from a one dimensional lattice system of size  $L$ , in which an arbitrary quantum state can be written as

$$|\psi\rangle = \sum_{\underline{\sigma}} c_{\sigma_1, \dots, \sigma_L} |\underline{\sigma}\rangle. \quad (3.1)$$

Here  $\sigma_i$  is a label for the local basis states at site  $i$ , while  $c_{\sigma_1, \dots, \sigma_L}$  are some, possibly complex, coefficients and  $|\underline{\sigma}\rangle = |\sigma_1\rangle \otimes \dots \otimes |\sigma_L\rangle$ . The coefficients  $c_{\sigma_1, \dots, \sigma_L}$  can in principle have an arbitrary form (up to normalization), but for this discussion it will

be useful to consider some special cases. Namely, assume that  $c_{\sigma_1, \dots, \sigma_L}$  factorizes into products of simple scalars

$$c_{\sigma_1, \dots, \sigma_L}^{\text{product}} = \prod_i c_{\sigma_i}^{[i]}. \quad (3.2)$$

Here the bracketed index refers to the site of the coefficient vector, as it may in principle be different on every site. In this case the state  $|\psi\rangle$  would be a product state, as it factorizes into tensor products of local states. An example for situations in which a product state can be a solution to a many-electron problem is when there is no interaction as then the eigenstates of the Hamiltonian can be written as tensor products of single particle eigenstates [71].

However, in many-body physics and specifically when considering strongly correlated electrons, a product state can usually not capture the physics of interest. As the name suggests a matrix product state is similar to Eq. (3.2) in that the coefficient is factorized. However for an MPS the factors are matrices and the multiplication is a matrix multiplication

$$c_{\sigma_1, \dots, \sigma_L}^{\text{MPS}} = \sum_{\underline{a}} M_{1, a_1}^{[1]\sigma_1} M_{a_1, a_2}^{[2]\sigma_2} \dots M_{a_{L-1}, 1}^{[L]\sigma_L}. \quad (3.3)$$

Here we introduced the bond indices labelled by  $a_i$ . The contraction of these bond indices is in essence nothing else than a matrix multiplication. Again the bracketed indices denote that the  $M$  tensor on every site may be different, however in order to not overload the notation we are going to drop this index from now on. We want the reader to note that this is only to make the notation simpler not because we assume the  $M$  tensors to be site independent.

In theory any arbitrary state can be expressed as an MPS, however, the bond dimension  $D$  can be exponentially large for an arbitrary state. In practice we restrict the dimension of the bond indices as follows. We can merge two neighbouring tensors of the MPS by contracting their intermediate bond index, i.e.

$$\tilde{M}_{a_{i-1}, a_{i+1}}^{\sigma_i \sigma_{i+1}} = \sum_{a_i} M_{a_{i-1}, a_i}^{\sigma_i} M_{a_i, a_{i+1}}^{\sigma_{i+1}}. \quad (3.4)$$

This two-site tensor can then again be split into two single-site tensors by the virtue of singular value decomposition

$$\tilde{M}_{a_{i-1}, a_{i+1}}^{\sigma_i \sigma_{i+1}} = \tilde{M}_{(\sigma_i a_{i-1}), (\sigma_{i+1} a_{i+1})} = U_{(\sigma_i a_{i-1}), a_i} S_{a_i} V_{a_i, (\sigma_{i+1} a_{i+1})}^\dagger. \quad (3.5)$$

Here one does usually only keep singular values  $S_a$  greater than some truncation threshold  $\epsilon$  so that insignificant contributions are discarded. This truncation is what

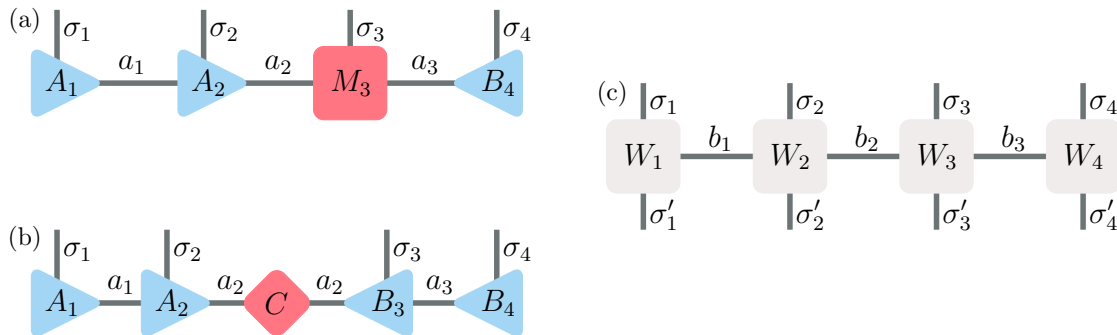


Figure 3.1: Pictorial representation of an MPS for a lattice of size  $L = 4$  in mixed canonical representation with respect to site 3 (a) and with respect to the bond in between site 2 and 3 respectively (b). Graphical depiction of an MPO (c) for a lattice of the same size.

makes MPS an efficient method, as the states, that one does usually treat (e.g. ground states) do have a singular value spectrum that is decaying rather fast and therefore many can be discarded with close to no loss of accuracy [32].

In the following sections, we will commonly use the so called canonical representations of MPS, namely every MPS can be brought into one of the following forms by applying successive merges and SVDs:

- a) Mixed canonical representation with respect to site  $i$

$$c_{\sigma_1, \dots, \sigma_L}^{\text{MPS}} = \sum_{\underline{a}} A_{1, a_1}^{\sigma_1} \cdots A_{a_{i-2}, a_{i-1}}^{\sigma_{i-1}} M_{a_{i-1}, a_i}^{\sigma_i} B_{a_i, a_{i+1}}^{\sigma_{i+1}} \cdots B_{a_{L-1}, 1}^{\sigma_L}. \quad (3.6)$$

- b) Mixed canonical representation with respect to the bond in between site  $i$  and  $i + 1$

$$c_{\sigma_1, \dots, \sigma_L}^{\text{MPS}} = \sum_{\underline{a}} A_{1, a_1}^{\sigma_1} \cdots A_{a_{i-2}, a_{i-1}}^{\sigma_{i-1}} A_{a_{i-1}, a_i}^{\sigma_i} C_{a_i} B_{a_i, a_{i+1}}^{\sigma_{i+1}} \cdots B_{a_{L-1}, 1}^{\sigma_L}. \quad (3.7)$$

In principle, we can also have mixed canonical representations with respect to multiple sites by merging more tensors into the center tensor in Eq. (3.6). The tensors  $A$  ( $B$ ) are called left (right) normalized which means they have the properties

$$\sum_{\sigma} (A^{\sigma\dagger} A^{\sigma})_{a,b} = \delta_{a,b} \quad (3.8)$$

$$\sum_{\sigma} (B^{\sigma} B^{\sigma\dagger})_{a,b} = \delta_{a,b}. \quad (3.9)$$

Analogous to states operators can also be written in matrix product form these are then called matrix product operators (MPO)

$$\begin{aligned}\mathcal{O} &= \sum_{\underline{\sigma}, \underline{\sigma}'} c_{\sigma_1, \dots, \sigma_L}^{\sigma'_1, \dots, \sigma'_L} |\underline{\sigma}'\rangle \langle \underline{\sigma}| \\ c_{\sigma_1, \dots, \sigma_L}^{\sigma'_1, \dots, \sigma'_L} &= \sum_{\underline{a}} W_{1, a_1}^{\sigma_1, \sigma'_1} \dots W_{a_{L-1}, 1}^{\sigma_{L-1}, \sigma'_{L-1}}.\end{aligned}\quad (3.10)$$

As all the tensor contractions in this section may seem complicated and overwhelming to a first time reader we present a pictorial representation of both a MPS and a MPO in Fig. 3.1. Here connected tensor legs correspond to contracted indices. In order to not overload the figures in the following sections with indices we are from now on only going to label uncontracted legs.

## 3.2 Density Matrix Renormalization Group

One of the core applications of MPS is the computation of ground states for interacting many body systems. The main algorithm that is used to this aim is the density matrix renormalization group [72] (DMRG). As before this section should rather be thought of as a quick overview than an extensive review, which should instead be found in Ref. [32]. In essence DMRG corresponds to minimizing the following function:

$$\mathcal{F}(|\psi\rangle, \lambda) = \langle \psi | H | \psi \rangle - \lambda (\langle \psi | \psi \rangle - 1) \quad (3.11)$$

Here  $H$  is the Hamiltonian and  $\lambda$  is a Lagrange multiplier guaranteeing normalization. Soon we will identify  $\lambda$  as the ground state energy of the reduced eigenvalue problem.

Depending on whether the minimization happens with respect to a single-site tensor or a two-site tensor the algorithm is called two-site or single-site DMRG. Here, we will focus on two-site DMRG thus we bring the MPS into the mixed canonical representation with respect to two sites and take the derivative with respect to the corresponding tensor  $M_{a_{i-1}, a_{i+1}}^{\sigma_i, \sigma_{i+1}^*}$

$$\begin{aligned}\frac{\partial \mathcal{F}}{\partial M_{a_{i-1}, a_{i+1}}^{\sigma_i, \sigma_{i+1}^*}} &= \sum_{a'_{i-1}, a'_{i+1}} \sum_{b_i, b_{i+1}, b_{i-1}} L_{b_{i-1}}^{a_{i-1}, a'_{i-1}} W_{b_{i-1}, b_i}^{\sigma_i, \sigma'_i} W_{b_i, b_{i+1}}^{\sigma_{i+1}, \sigma'_{i+1}} R_{b_{i+1}}^{a_{i+1}, a'_{i+1}} M_{a'_{i-1}, a'_{i+1}}^{\sigma'_i, \sigma'_{i+1}} \\ &- \lambda M_{a_{i-1}, a_{i+1}}^{\sigma_i, \sigma_{i+1}} \stackrel{!}{=} 0,\end{aligned}\quad (3.12)$$

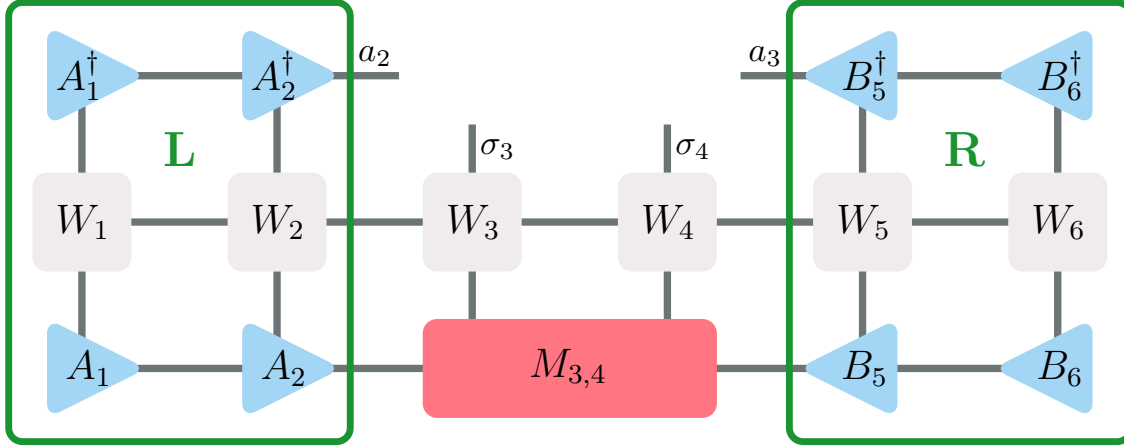


Figure 3.2: Graphical depiction of the left side of (3.13) for a lattice of size 6 and  $i = 3$ . All contracted indices are suppressed. The left and right contractions  $L$  and  $R$  are depicted by the green encircled tensors.

where  $W_{b_{i-1}, b_i}^{\sigma_i, \sigma'_i}$  is the MPO tensor of  $H$  at site  $i$  and we used that all tensors in the MPS are left (right) normalized for sites left (right) to site  $i$  ( $i + 1$ ).  $L$  and  $R$  are defined as:

$$L_{b_{i-1}}^{a_{i-1}, a'_{i-1}} = \sum_{\substack{a_l, a'_l, b_l \\ l < i-1}} \sum_{\substack{\sigma_l, \sigma'_l \\ l < i}} A_{1, a'_1}^{\sigma'_1} W_{1, b_1}^{\sigma'_1, \sigma_1} A_{1, a_1}^{\sigma_1*} \dots A_{a'_{i-2}, a'_{i-1}}^{\sigma'_{i-1}} W_{b_{i-2}, b_{i-1}}^{\sigma'_{i-1}, \sigma_{i-1}} A_{a_{i-2}, a_{i-1}}^{\sigma_{i-1}*}$$

$$R_{b_{i+1}}^{a_{i+1}, a'_{i+1}} = \sum_{\substack{a_l, a'_l, b_l \\ l > i+1}} \sum_{\substack{\sigma_l, \sigma'_l \\ l > i+1}} B_{a'_{i+1}, a'_{i+2}}^{\sigma'_{i+2}} W_{b_{i+1}, b_{i+2}}^{\sigma'_{i+2}, \sigma_{i+2}} B_{a_{i+1}, a_{i+2}}^{\sigma_{i+2}*} \dots B_{a'_{L-1}, 1}^{\sigma'_L} W_{b_L, 1}^{\sigma'_L, \sigma_L} B_{a_{L-1}, 1}^{\sigma_L*}.$$

Now Eq. (3.12) can be understood as eigenvalue problem for a matrix  $H^{\text{eff}}$  defined as

$$H^{\text{eff}} v = \lambda v \quad (3.13)$$

$$H_{(\sigma_i, \sigma_{i+1}, a_{i-1}, a_{i+1}), (\sigma'_i, \sigma'_{i+1}, a'_{i-1}, a'_{i+1})}^{\text{eff}} = \sum_{\underline{b}} L_{b_{i-1}}^{a_{i-1}, a'_{i-1}} W_{b_{i-1}, b_i}^{\sigma_i, \sigma'_i} W_{b_i, b_{i+1}}^{\sigma_{i+1}, \sigma'_{i+1}} R_{b_{i+1}}^{a_{i+1}, a'_{i+1}}$$

$$v_{(\sigma_i, \sigma_{i+1}, a_{i-1}, a_{i+1})} = M_{a_{i-1}, a_{i+1}}^{\sigma_i, \sigma_{i+1}}.$$

Thus solving the eigenvalue problem (3.13) with respect to its ground state we find a new optimized tensor  $\tilde{M}$ . A graphical depiction of the left side of (3.13) can be seen in Fig. 3.2.

By the use of a singular value competition the MPS can be brought into a mixed canonical representation with respect to the two sites on the right (left). The new tensor will in practice have a singular value spectrum that yields an increase in bond dimension between the sites  $i$  and  $i+1$  up to a maximum of  $dD$  with  $D$  the maximal bond dimension of the old tensor. In order to keep the computation feasible we will usually truncate the bond dimension at some maximal value  $D$  thus keeping only the  $D$  most important states of the local eigenvalue problem.

Once the representation has been shifted to the mixed canonical form with respect to the next sites we can repeat the process described above to obtain another two-site update. Since the optimization is only done rather locally, in order to make sure that we converge to the overall ground state, we have to repeat this process, sweeping back and forth through the MPS, until convergence is reached [32].

### 3.3 Krylov Time Evolution

In this section we briefly introduce the global Krylov time evolution method. As before our goal is to convey to the reader the idea of the method rather than go into every detail. For a more detailed review please refer to Ref. [73].

As the name suggests the global Krylov method is a global method that does in principle not depend on the MPS structure and can also be applied to non-MPS specific problems.

The key idea is to reduce the dimensionality of the problem by projecting the time-evolution operator into a so called Krylov subspace. The Krylov subspace of dimension  $n$  with respect to a state  $|\Psi\rangle$  and Hamiltonian  $H$  is defined as  $\mathcal{K}_n = \text{span}(|\Psi\rangle, \dots, H^{n-1}|\Psi\rangle)$ . In order to write the projector it is useful to define an orthonormal basis of  $\mathcal{K}_n$  by  $\{|\xi_1\rangle, \dots, |\xi_n\rangle\}$  where  $|\xi_i\rangle$  is obtained by successively orthonormalizing  $H^{i-1}|\Psi\rangle$  against every other  $|\xi_j\rangle$  with  $j < i$ . The best approximation to the exact time evolved state that can be made in  $\mathcal{K}_n$  is the projection of the exact state onto  $\mathcal{K}_n$ . Therefore, when we start from  $|\Psi\rangle$  and want to make a time step of  $\delta t$  our best approximation reads:

$$|\Psi(\Delta t)\rangle = P_{\mathcal{K}_n} e^{-i\Delta t H} |\Psi\rangle = P_{\mathcal{K}_n} e^{-i\Delta t H} P_{\mathcal{K}_n} |\Psi\rangle \quad (3.14)$$

$$= \sum_{k=0}^{\infty} P_{\mathcal{K}_n} \frac{(-i\Delta t)^k}{k!} H^k P_{\mathcal{K}_n} |\Psi\rangle \quad (3.15)$$

$$\approx \sum_{k=0}^{\infty} \frac{(-i\Delta t)^k}{k!} (P_{\mathcal{K}_n} H P_{\mathcal{K}_n})^k |\Psi\rangle. \quad (3.16)$$

Here we introduced the projector onto  $\mathcal{K}_n$  as  $P_{\mathcal{K}_n} = \sum_{i=1}^n |\xi_i\rangle \langle \xi_i|$ . Note that the first line is exact, as  $|\Psi\rangle$  is already within  $\mathcal{K}_n$ . The approximation in the third line consists in the insertion of the projector in between each  $H$ . This would only be exact if  $\mathcal{K}_n$  would span the entire Hilbert space. Continuing from here we obtain

$$|\Psi(\Delta t)\rangle \approx e^{-i\Delta t P_{\mathcal{K}_n} H P_{\mathcal{K}_n}} |\Psi\rangle \quad (3.17)$$

$$= \sqrt{\langle \Psi | \Psi \rangle} \sum_j |\xi_j\rangle (e^{-i\Delta t P_{\mathcal{K}_n} H P_{\mathcal{K}_n}})_{j,1}. \quad (3.18)$$

Here we used that  $|\xi_1\rangle = |\Psi\rangle / \sqrt{\langle \Psi | \Psi \rangle}$ . Note that the exponentiation of  $P_{\mathcal{K}_n} H P_{\mathcal{K}_n}$  is numerically comparably easy as its matrix dimension is equal to  $\dim(\mathcal{K}_n) = n$ . The main computational weight rests on the repeated application of  $H$  when building up the Krylov subspace. In practice, one needs to include enough Krylov vectors  $|\xi_i\rangle$  such that the inclusion of a further vector does not change the state in a significant way. A reasonable criterion for convergence in the dimension of  $\mathcal{K}_n$  is therefore  $|(e^{-i\Delta t P_{\mathcal{K}_n} H P_{\mathcal{K}_n}})_{n,1}|$ . Once the last element of the exponential is smaller than some threshold value the krylov subspace expansion can be considered converged.

### 3.4 Time Dependent Variational Principle

The Time Dependent Variational Principle (TDVP) is a rather general procedure [74, 75] that can be used in order to evolve states in time given any variational ansatz. The idea is to project the evolution onto the tangent space of the variational manifold. In practice we are going to apply TDVP to MPS [76, 77] defining it as our variational manifold. In principle one can allow the variation of single-site, two-site or even multi-site tensor, however the computational complexity rises significantly the more sites are allowed to vary at once. For the sake of simplicity in this section we are going to discuss single-site TDVP only, as before the goal of this section is to give the reader an intuitive understanding of TDVP rather than give an in depth review. The latter can be found in Ref. [73].

Our starting point is the time dependent Schrödinger equation (TDSE)

$$\frac{\partial}{\partial t} |\Psi(t)\rangle = -iH |\Psi(t)\rangle. \quad (3.19)$$

The projector onto the tangent space of our variational manifold ( $M$ ) can be written as [73]

$$P_{T_{|\Psi\rangle}M} = \sum_{i=1}^L P_{i-1}^l \otimes \mathbb{1} \otimes P_{i+1}^r - \sum_{i=1}^L P_i^l \otimes P_{i+1}^r, \quad (3.20)$$

where  $L$  is the number of sites. It is instructive to define  $P^{l/r}$  in terms of the left and right bases of the MPS in mixed canonical representation

$$|a\rangle_i^l = \sum_{\substack{\sigma_k \\ k \leq i}} (A^{\sigma_1} \dots A^{\sigma_i})_{1,a} |\sigma_1\rangle \otimes \dots \otimes |\sigma_i\rangle \quad (3.21)$$

$$|b\rangle_i^r = \sum_{\substack{\sigma_k \\ k \geq i}} (B^{\sigma_i} \dots B^{\sigma_L})_{b,1} |\sigma_i\rangle \otimes \dots \otimes |\sigma_L\rangle. \quad (3.22)$$

Note that  $\langle a|a'\rangle_i^{l/r} = \delta_{a,a'}$  due to the left (right) normalisation properties of the  $A$  ( $B$ ) tensors. With the help of these basis states, the mixed canonical representation introduced in Sec. 3.1 can be written as

$$|\Psi\rangle = \sum_{a,b,\sigma_i} M_{a,b}^{\sigma_i} |a\rangle_{i-1}^l \otimes |\sigma_i\rangle \otimes |b\rangle_{i+1}^r. \quad (3.23)$$

The projectors from Eq. 3.20 can then be defined as:

$$P_i^l = \sum_a |a\rangle_i^l \langle a|_i^l \quad (3.24)$$

$$P_i^r = \sum_b |b\rangle_i^r \langle b|_i^r \quad (3.25)$$

$$P_0^l = 1 \quad \wedge \quad P_{L+1}^r = 1. \quad (3.26)$$

With these definitions in place we can intuitively understand the definition of the tangent space projector  $P_{T_{|\Psi\rangle}M}$  in Eq. 3.20. Namely, the first term allows the variation of a single site tensor on any site, while the second term projects out changes parallel to  $|\Psi\rangle$  in order to ensure norm conservation. Thus, if one wanted to derive two-site TDVP one would have to allow for the variation of two neighbouring sites in the first term.

Applying the above projector onto the TDSE we obtain

$$\frac{\partial}{\partial t} |\Psi(t)\rangle \approx -i P_{T_{|\Psi\rangle}M} H |\Psi(t)\rangle. \quad (3.27)$$

This can be solved by exponentiating the operator on the right:

$$|\Psi(\Delta t)\rangle \approx e^{-i P_{T_{|\Psi\rangle}M} H \Delta t} |\Psi\rangle \quad (3.28)$$

Now even after the projection on the tangent space Eq. 3.28 is still not solvable, however we can write

$$P_{T_{|\Psi\rangle}M}H = \sum_k h_{1,k} - \sum_k h_{2,k} \quad (3.29)$$

$$h_{1,k} = P_{k-1}^l \otimes \mathbb{1} \otimes P_{k+1}^r H \quad (3.30)$$

$$h_{2,k} = P_k^l \otimes P_{k+1}^r H \quad (3.31)$$

and apply a second order symmetric Trotter-Suzuki decomposition [78, 79]:

$$\begin{aligned} |\Psi(\Delta t)\rangle &\approx e^{-ih_{1,1}\frac{\Delta t}{2}} e^{ih_{2,1}\frac{\Delta t}{2}} \dots e^{-ih_{1,L}\Delta t} e^{ih_{2,L}\Delta t} \dots e^{ih_{2,1}\frac{\Delta t}{2}} e^{-ih_{1,1}\frac{\Delta t}{2}} |\Psi\rangle \\ &+ \mathcal{O}(\Delta t^3) \end{aligned} \quad (3.32)$$

This is equivalent to performing all the evolutions above successively. Thus one ends up with equations of the following form

$$\frac{\partial}{\partial t} |\tilde{\Psi}_{1,k}(t)\rangle = -\frac{i}{2} h_{1,k} |\tilde{\Psi}_{1,k}\rangle \quad (3.33)$$

$$\frac{\partial}{\partial t} |\tilde{\Psi}_{2,k}(t)\rangle = \frac{i}{2} h_{2,k} |\tilde{\Psi}_{2,k}\rangle. \quad (3.34)$$

Here we denoted the intermediate state that already had some evolutions performed on top of it by  $|\tilde{\Psi}_{1/2,k}\rangle$ . Contracting the above equations from the left with  $|a\rangle_{k-1}^l \otimes |\sigma_k\rangle \otimes |b\rangle_{k+1}^r$  and  $|a\rangle_k^l \otimes |b\rangle_{k+1}^r$  respectively we obtain

$$\frac{\partial}{\partial t} M_{a,b}^{\sigma_k}(t) = -\frac{i}{2} \sum_{a',b',\sigma'_k} (H_1^{\text{eff}})_{a',b',\sigma'_k}^{a,b,\sigma_k} M_{a',b'}^{\sigma'_k}(t) \quad (3.35)$$

$$\frac{\partial}{\partial t} C_a(t) = \frac{i}{2} \sum_{a'} (H_2^{\text{eff}})_{a'}^a C_{a'}(t), \quad (3.36)$$

where  $M_{a,b}^{\sigma_k}$  is the center tensor in the mixed canonical representation with respect to site  $k$  and  $C_a$  is the center matrix in the mixed canonical representation with respect to the bond between site  $k$  and  $k+1$ . The effective Hamiltonians  $H_{1/2}^{\text{eff}}$  are given as

$$(H_1^{\text{eff}})_{a',b',\sigma'_k}^{a,b,\sigma_k} := \langle a|_{k-1}^l \otimes \langle \sigma_k| \otimes \langle b|_{k+1}^r H |a'\rangle_{k-1}^l \otimes |\sigma'_k\rangle \otimes |b'\rangle_{k+1}^r \quad (3.37)$$

$$(H_2^{\text{eff}})_{a'}^a := \langle a|_k^l \otimes \langle a|_{k+1}^r H |a'\rangle_k^l \otimes |a'\rangle_{k+1}^r. \quad (3.38)$$

As these equations are a bit complicated we show a pictorial representation of (3.37) and (3.38) in Fig. 3.3(a) and (b), respectively.

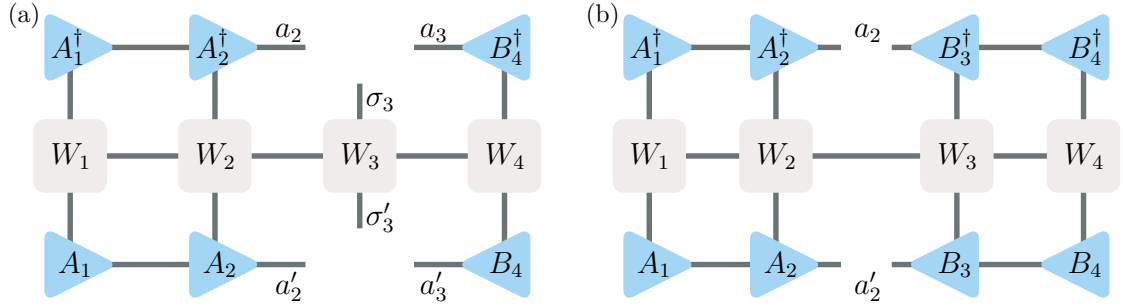


Figure 3.3: Graphical depiction of the effective Hamiltonians (3.37, 3.38) for a single site (a) and a single bond update (b) respectively. The depicted tensor networks correspond to a lattice of size 4. The effective Hamiltonian is the one for site 3 (a) and the bond in between sites 2 and 3 (b).

There are four sources of error for TDVP, namely, the error of the projection onto the tangent space, the time step error stemming from the Trotter-Suzuki decomposition, the error of the local exponentiation of  $H_{1/2}^{\text{eff}}$  and the error stemming from the successive truncation of the MPS. All of those errors can in principle be controlled. The Trotter-Suzuki error is usually rather small because it scales cubically with the time step and the local exponentiation is usually also exact (depending on the settings of the local solver). The projection error however depends on the bond dimension as the projectors are built from the state, thus having large bond dimension keeps the projection error in check. The inherent problem of single-site TDVP is that it does not allow for an increase in bond dimension from time step to time step which leads to an increasing projection error. Were we to do the same derivation for two-site TDVP, we would obtain similar equations with the difference, that we also obtain updates for two-site tensors. This difference is quite important as it means that in two-site TDVP one can allow for increasing bond dimensions, which may be necessary in order to correctly describe the time evolution. In the case where one allows for increasing bond dimension, the main remaining error is the truncation error. It can be controlled as described before by truncating only weakly, but depending on the complexity of the problem at hand the increasing bond dimension may lead to long runtimes. Overall it has to be noted that given a certain maximal bond dimension  $D$ , TDVP is bound to be faster than the global Krylov method, as it largely profits from the locality of its formulation.

## 3.5 Symmetries

Let  $H$  be the Hamiltonian of our system of interest,  $O$  any observable and  $\mathcal{H}$  the Hilbert space. If  $H$  commutes with  $O$  this means that there exists a basis in which both of them are diagonal. Now assume that  $O$  has a set of distinct eigenvalues  $\sigma = \{\lambda_i : \lambda_i \neq \lambda_j, \forall i, j\}$ . Then if  $|\sigma| < \dim(\mathcal{H})$  there are multiple bases in which  $O$  is diagonal. Picking an arbitrary one of those and expressing  $H$  in it, yields a block diagonal form. This means in order to find the eigenstates of  $H$  one only has to find the eigenstates for every block.

Moreover assume  $|\Psi, \lambda\rangle$  is a state such that  $O|\Psi, \lambda\rangle = \lambda|\Psi, \lambda\rangle$ , then

$$Of(H)|\Psi, \lambda\rangle = \lambda f(H)|\Psi, \lambda\rangle, \quad (3.39)$$

where  $f(H)$  is some analytic function of  $H$ . This statement might seem trivial, but it has quite a few important consequences when doing DMFT. First of all it means that when one starts DMRG from a state with a given set of quantum numbers, that are conserved by the Hamiltonian then DMRG will not change those quantum numbers as it is a variational approach that works by application of the Hamiltonian. Thus if one wants to consistently find the global ground state of the Hamiltonian one needs to identify all the conserved quantum numbers and start a DMRG within each of the different quantum number sectors.

More importantly a conserved quantum number always corresponds to a symmetry of the Hamiltonian, which can and should be implemented on a tensor network level. In this work we are not going into detail about how to do this, we instead refer to Claudius Hubig's PhD thesis<sup>1</sup> [81]. We want to stress that if one does not implement all the symmetries of the Hamiltonian into ones lattice, then the DMRG may get stuck in a quantum number sector unknowingly [82]. This would mean that one might find a local minimum of the Hamiltonian instead of a global one and thus obtains wrong results for all the correlators computed from said faulty ground state. Another important consequence is that if the quantum numbers are such that the particle creation operators  $c_i^\dagger$  of the problem change the quantum numbers in a well defined way then this leads to a block structure for the correlators computed from the ground state within DMFT. Assume that the  $c_i^\dagger$  are such that:

$$Oc_i^\dagger|\Psi, \lambda\rangle = \lambda'c_i^\dagger|\Psi, \lambda\rangle \quad (3.40)$$

---

<sup>1</sup>Claudius Hubig is the original author of the tensor network toolkit SYTEN [80] that was used during this thesis and his thesis gives an extensive introduction about symmetries in tensor networks.

with  $\lambda' = \lambda + \Delta\lambda_i$  and  $|\Psi, \lambda\rangle$  defined as a above. Then a given correlator

$$\langle \Psi, \lambda | c_j e^{-\tau(H-E_0)} c_i^\dagger | \Psi, \lambda \rangle \quad (3.41)$$

can only be finite if  $\Delta\lambda_i = \Delta\lambda_j$ . This is rather important as it explains, why often times within DMFT all dynamical quantities like local Green's functions and self energies have identical block structure. In addition treating the quantum numbers correctly is a key ingredient necessary to properly account for degenerate ground states present in some models as we will introduce in Sec. 4.2.

# Chapter 4

## Matrix-Product-State based Impurity Solver

In this chapter we want to introduce the MPS-based impurity solver most of the DMFT results in this work were obtained with. The impurity solver we used is called the *Optimized Basis Tensor Network Impurity Solver* (OTIS) and was developed in equal parts by the author of this work and Martin Grundner. Previous versions of this solver have already successfully been applied in the context of DFT+DMFT [4, 35] as well as model calculations [34]. All MPS calculations included in the solver are performed using the SYTEN toolkit [80, 81]. To this date our solver is able to perform calculations on both the real and the imaginary frequency axis. However as the author of this thesis mainly focussed on the imaginary frequency part the real frequency version was mainly implemented by Martin Grundner. Thus for details on the real frequency implementation we refer the reader to his works [83, 84]. The goal of this chapter is to guide the reader through all the steps necessary to perform successful DMFT calculations. Namely in Secs. 4.1-4.4 we are going to explain in detail how given an hybridisation one can obtain the self-energy of the impurity problem by the use of MPS. As DMFT usually works at fixed chemical potential further steps are needed to perform computations at fixed density. Those are explained in Sec. 4.5. When we are interested in real frequency quantities, but our results were obtained on the imaginary axis, we have to resort to numerical analytic continuation a topic which is covered in Sec. 4.6. Finally, in Sec. 4.7 we are going to explain how to interface new models into our solver.

## 4.1 Discretization

As mentioned in Chap. 2 the starting point for the impurity solver is some non-interacting Green's function  $\mathcal{G}(i\omega_n)$  for the impurity model. The task of the solver is to find the interacting Green's function  $G(i\omega_n)$  for a system that features local interactions given that the non-interacting model is described by  $\mathcal{G}(i\omega_n)$ . Now the first step is to define a model that behaves like  $\mathcal{G}(i\omega_n)$  in the absence of interactions. The usual choice is the Anderson Impurity Model (AIM) [66]. Therefore, we want to start with a discrete version of the AIM and derive its non-interacting Green's function, from which we will identify how to properly determine the AIM's parameters such that it mimics  $\mathcal{G}(i\omega_n)$ .

### 4.1.1 The non-interacting Anderson Impurity Model

The Hamiltonian of the discrete AIM for a system consisting of a bath and multiple impurities is given by:

$$H = H_{\text{imp}} + H_{\text{hyb}} + H_{\text{bath}} \quad (4.1)$$

$$H_{\text{imp}} = \sum_{i,j \in I} \xi_{i,j} c_i^\dagger c_j + \sum_{i,j,n,m \in I} V_{ijnm} c_i^\dagger c_j^\dagger c_n c_m \quad (4.2)$$

$$H_{\text{hyb}} = \sum_{i \in I} \sum_{k \in B} \gamma_{ik} c_i^\dagger c_k + h.c. \quad (4.3)$$

$$H_{\text{bath}} = \sum_{k \in B} \epsilon_k c_k^\dagger c_k. \quad (4.4)$$

Here  $\xi$  are single-particle terms on the impurity cluster,  $V$  is the interaction on the impurity cluster,  $\gamma$  are the hopping elements between bath and impurity cluster and  $\epsilon$  are the on-site potentials in the bath. We denoted the set of impurity orbitals by  $I$  and the set of bath orbitals by  $B$ . For this section we will assume that there is no interaction ( $V = 0$ ) since we want to determine the non-interacting Green's function for the AIM. The approach we pursue is based on the derivation of an equation of motion for the Green's function. This is similar to the solution presented in Ref. [85], but while their derivation is given on the real frequency axis, here we focus on the imaginary axis. The time ordered non-interacting Green's function  $G_{ij}^0(\tau)$  with  $i, j \in I$  is given as follows:

$$G_{ij}^0(\tau) = -\Theta(\tau) \langle 0 | c_i(\tau) c_j^\dagger | 0 \rangle + \Theta(-\tau) \langle 0 | c_j^\dagger c_i(\tau) | 0 \rangle, \quad (4.5)$$

where we denoted the ground state as  $|0\rangle$ . Taking the derivative of (4.5) with respect to  $\tau$  we obtain

$$\begin{aligned} \frac{\partial G_{ij}^0}{\partial \tau}(\tau) = & -\delta(\tau) \langle 0 | c_i(\tau) c_j^\dagger | 0 \rangle - \Theta(\tau) \langle 0 | [H, c_i](\tau) c_j^\dagger | 0 \rangle \\ & -\delta(-\tau) \langle 0 | c_j^\dagger c_i(\tau) | 0 \rangle + \Theta(-\tau) \langle 0 | c_j^\dagger [H, c_i](\tau) | 0 \rangle. \end{aligned} \quad (4.6)$$

The commutator  $[H, c_i](\tau)$  yields

$$[H, c_i](\tau) = -\sum_k \gamma_{ik} c_k(\tau) - \sum_{l \in I} \xi_{il} c_l. \quad (4.7)$$

Inserting this expression into (4.6) we find

$$\frac{\partial G_{ij}^0}{\partial \tau}(\tau) = -\delta(\tau) \delta_{ij} - \sum_{k \in B} \gamma_{ik} G_{kj}^0(\tau) - \sum_{l \in I} \xi_{il} G_{lj}^0(\tau), \quad (4.8)$$

which defines an equation of motion for  $G^0(\tau)$ . Repeating the same steps for  $G_{kj}^0(\tau)$  with  $i \in I$  and  $k \in B$  we obtain

$$\frac{\partial G_{kj}^0}{\partial \tau}(\tau) = -\Theta(\tau) \langle 0 | [H, c_k](\tau) c_j^\dagger | 0 \rangle + \Theta(-\tau) \langle 0 | c_j^\dagger [H, c_k](\tau) | 0 \rangle. \quad (4.9)$$

Here the terms going with  $\delta(\tau)$  immediately vanished as  $\delta_{jk} = 0$ . The commutator yields

$$\begin{aligned} [H, c_k](\tau) &= \sum_{i \in I} \gamma_{ik}^* [c_k^\dagger c_i, c_k] + \epsilon_k [c_k^\dagger c_k, c_k] \\ &= -\sum_{i \in I} \gamma_{ik}^* c_i - \epsilon_k c_k. \end{aligned} \quad (4.10)$$

Inserting this into (4.9) we obtain

$$\frac{\partial G_{kj}^0}{\partial \tau}(\tau) = -\sum_{i \in I} \gamma_{ik}^* G_{ij}^0(\tau) - \epsilon_k G_{kj}^0(\tau). \quad (4.11)$$

It is now useful to insert the Fourier transform of  $G(\tau) = \sum_n G(i\omega_n) e^{-i\omega_n \tau}$  into (4.8) and (4.11). This lets us obtain the following equations in frequency domain:

$$-i\omega_n G_{ij}^0(i\omega_n) = -\delta_{ij} - \sum_{k \in B} \gamma_{ik} G_{kj}^0(i\omega_n) - \sum_{l \in I} \xi_{il} G_{lj}^0(i\omega_n) \quad (4.12)$$

$$-i\omega_n G_{kj}^0(i\omega_n) = -\sum_{l \in I} \gamma_{lk}^* G_{lj}^0(i\omega_n) - \epsilon_k G_{kj}^0(i\omega_n) \quad (4.13)$$

It follows that

$$G_{kj}^0(i\omega_n) = \sum_{l \in I} \frac{\gamma_{lk}^*}{i\omega_n - \epsilon_k} G_{lj}^0(i\omega_n). \quad (4.14)$$

Now we can insert this into the upper equation and obtain

$$-i\omega_n G_{ij}^0(i\omega_n) = -\delta_{ij} - \sum_{l \in I} \sum_{k \in B} \frac{\gamma_{lk}^* \gamma_{ik}}{i\omega_n - \epsilon_k} G_{lj}^0(i\omega_n) - \sum_{l \in I} \xi_{il} G_{lj}^0(i\omega_n). \quad (4.15)$$

Finally, we can identify the so called discrete Hybridisation function  $\Delta^D(i\omega_n)$

$$\Delta_{ij}^D(i\omega_n) = \sum_{k \in B} \frac{\gamma_{ik} \gamma_{jk}^*}{i\omega_n - \epsilon_k} \quad (4.16)$$

and write the above as a matrix equation

$$-i\omega_n G^0(i\omega_n) = -\mathbb{1} - \Delta^D(i\omega_n) G^0(i\omega_n) - \xi G^0(i\omega_n). \quad (4.17)$$

Thus we obtain

$$i\omega_n \mathbb{1} - \xi - \Delta^D(i\omega_n) = (G^0(i\omega_n))^{-1}. \quad (4.18)$$

Replacing  $G^0(i\omega_n)$  by the Weiss field  $\mathcal{G}(i\omega_n)$  we obtain

$$\Delta(i\omega_n) = i\omega_n \mathbb{1} - \xi - (\mathcal{G}(i\omega_n))^{-1}. \quad (4.19)$$

Here we introduced the hybridisation  $\Delta(i\omega_n)$  that the AIM has to mimic so that it is the single site problem described by  $\mathcal{G}(i\omega_n)$ . Thus starting with some non-interacting Green's function  $\mathcal{G}(i\omega_n)$  we can set up our discrete AIM to reproduce the correct non-interacting behaviour by fitting the parameters  $\gamma_{ik}$  and  $\epsilon_k$  such that  $\Delta^D(i\omega_n) \approx \Delta(i\omega_n)$ .

Note that all local terms should be absorbed into  $\xi$  as otherwise  $\Delta(i\omega_n)$  does not decay to 0 as  $i\omega_n$  increases, making it impossible to fit with the shape of  $\Delta^D(i\omega_n)$ , which will in practice yield wrong results as the fits become unfaithful.

### 4.1.2 Fitting the Hybridisation

In the most general case  $\Delta(i\omega_n)$  is a matrix valued function and the parameters  $\gamma_{ik}$ ,  $\epsilon_k$  are obtained by optimizing the cost function

$$\chi(\gamma_{ik}, \epsilon_k) = \frac{1}{N_{\text{cut}}} \sum_n^{\omega_n^{-\alpha}} \sum_{ij} \left| \Delta_{ij}(i\omega_n) - \sum_k \frac{\gamma_{ik} \gamma_{jk}^*}{i\omega_n - \epsilon_k} \right|^2. \quad (4.20)$$

Here  $N_{\text{cut}}$  is a cut off that is introduced because points at high frequencies only contain little information due to the decaying  $\frac{1}{i\omega_n - \epsilon_k}$  terms. In all applications of this thesis we chose  $N_{\text{cut}}$  such that the fitting interval includes Matsubara frequencies up to  $\omega_n = 6 \text{ eV}$ , which is fairly high. Therefore, it is fair to assume that not much more information is contained in higher frequencies.

$\alpha$  is a parameter that can be used to weight different regions of the fit. In general we found it to be good practice to use  $\alpha = 1$  for metals and  $\alpha = 0$  for insulators. The reason for this choice is that in the case of a metal  $\Delta(i\omega_n)$  tends to be finite in the limit of  $\omega_n \rightarrow 0$ . As the low Matsubara frequencies are closest to the real axis one should try to fit them most accurately. The reason for choosing  $\alpha = 0$  for insulators is that in the limit of  $\omega_n \rightarrow 0$  the hybridisation  $\Delta(i\omega_n)$  is zero as there is a gap around  $\omega = 0$  on the real axis. This tends to make the hardest to fit region quite simple, as it is not necessary to put an energy  $\epsilon_k$  close to 0 and therefore insulators are far easier to fit. Thus in our applications we found that it was not necessary to emphasize the importance of low frequencies through the weighting function to obtain a satisfactory fit.

We only recently became aware that in Ref. [86] it was proposed to use  $\text{Tr}|\Sigma(i\omega_n)|^2$  as a weighting function instead of  $\omega_n^{-\alpha}$ , where  $\Sigma(i\omega_n)$  is the impurity self-energy of the last iteration and  $\text{Tr}$  denotes a matrix trace. While originally introduced in the context of ED, the arguments in Ref. [86] are based on the minimization of the self-energy functional [56, 58], which may also be interesting in the context of MPS, where small baths are not as much of a problem. Since insulators are however already well fit with a few bath sites this would likely only be useful, when fitting metallic states. However during this thesis the use of this alternative weighting function was not benchmarked which is why we leave its investigation for further studies.

Note that in principle as we are working at zero temperature  $\omega_n$  should be continuous, however we have to choose some discretization of the frequency axis. We believe it is reasonable to choose the frequencies as if they were Matsubara frequencies at some fictitious inverse temperature  $\beta$ , i.e.  $\omega_n = \frac{(2n+1)\pi}{\beta}$ . Here  $\beta$  should be chosen sufficiently high as to ensure good resolution. In practice fits become harder the higher  $\beta$ . In most of the applications within the context of this thesis we were using  $\beta = 200 \text{ eV}^{-1}$ .

This procedure to obtain the parameters for the discrete impurity problem was first introduced by M. Caffarel and W. Krauth [28] in the context of ED solvers. In general it is safe to say that we will be using far more sites than ED and therefore the above mentioned cost function optimization is more complicated.

For this reason we use a two step optimization procedure. In both steps we use the basinhopping algorithm [87, 88] implementation of SciPy [89]. The basinhopping

algorithm starts with an initial guess for the parameters  $\gamma_{ik}, \epsilon_k$  and then takes a step with a specified step size in parameter space. At position of the new parameters a local optimizer [90] is called which finds a local minimum close to those new parameters. Similar to simulated annealing [91] this step is accepted if the local minimum has a lower cost function than the previous parameters or otherwise with a probability  $e^{-\frac{1}{T}(\chi_{\text{old}} - \chi_{\text{new}})}$ , where  $T$  is a parameter that can be tuned to control how likely new steps are accepted. This search runs until a specified maximal number of steps has been completed, after which the optimal parameter set is returned.

The first step of our two step procedure starts parallel on every core with separate random initial guesses. The control parameter  $T$  is usually set to 1 so that the search is not restricted to a too small region of the parameter space. While in principle one may use any of the local optimizers implemented within SciPy [90] in conjunction with their basinhopping algorithm, we have implemented an analytic version of the gradient and Hessian of the cost function. It is therefore reasonable to use local optimizers that make use of both.

In the second step we take as initial guess the best parameter set we found in the first step, but start calculations in parallel at varying step sizes. We then run basinhopping again with gradually decreasing  $T$  until the optimal parameter set does not change or a timeout condition is reached. In practice we tend to use the `trust-krylov` [92] method for the initial search and the `dogleg` [93] method for the refined optimization. The reason for this choice is that dogleg seemed to be the fastest and therefore most suited for the refined search, while it sometimes seemed to get stuck in local minima when used for the global search where the trust region krylov method performed best.

In Fig. 4.1 we show a comparison of fits with different number of sites for a both a typical metallic and a typical insulating system. The first observation that should be made is that indeed as mentioned above the insulating hybridisation on the imaginary axis (b2) tends to zero, while the metallic one (a2) does not. This is the case because  $\Delta(i\omega_n)$  is an analytic function which means that  $\lim_{i\omega_n \rightarrow 0} \Delta(i\omega_n)$  coincides with  $\lim_{\omega \rightarrow 0} \Delta(\omega)$ . The fact that the real part of  $\Delta(i\omega_n)$  in Fig. 4.1 is zero is special to the displayed case, as the system shown is particle hole symmetric. However, the behaviour of the fits is similar also in non-particle hole symmetric cases. Inspecting the deviation from the exact hybridisation (a3, b3) we find that in the metallic case  $L_b = 8$  bath sites seem to be sufficient to describe the system as errors are dropping to  $\leq 10^{-3}$ . Comparing this to the insulating case we find that the fits are already rather well converged with only  $L_b = 4$  bath sites.

In practice, how many bath sites have to be used to describe the problem with a certain accuracy is very much problem dependent. In principle, one should always

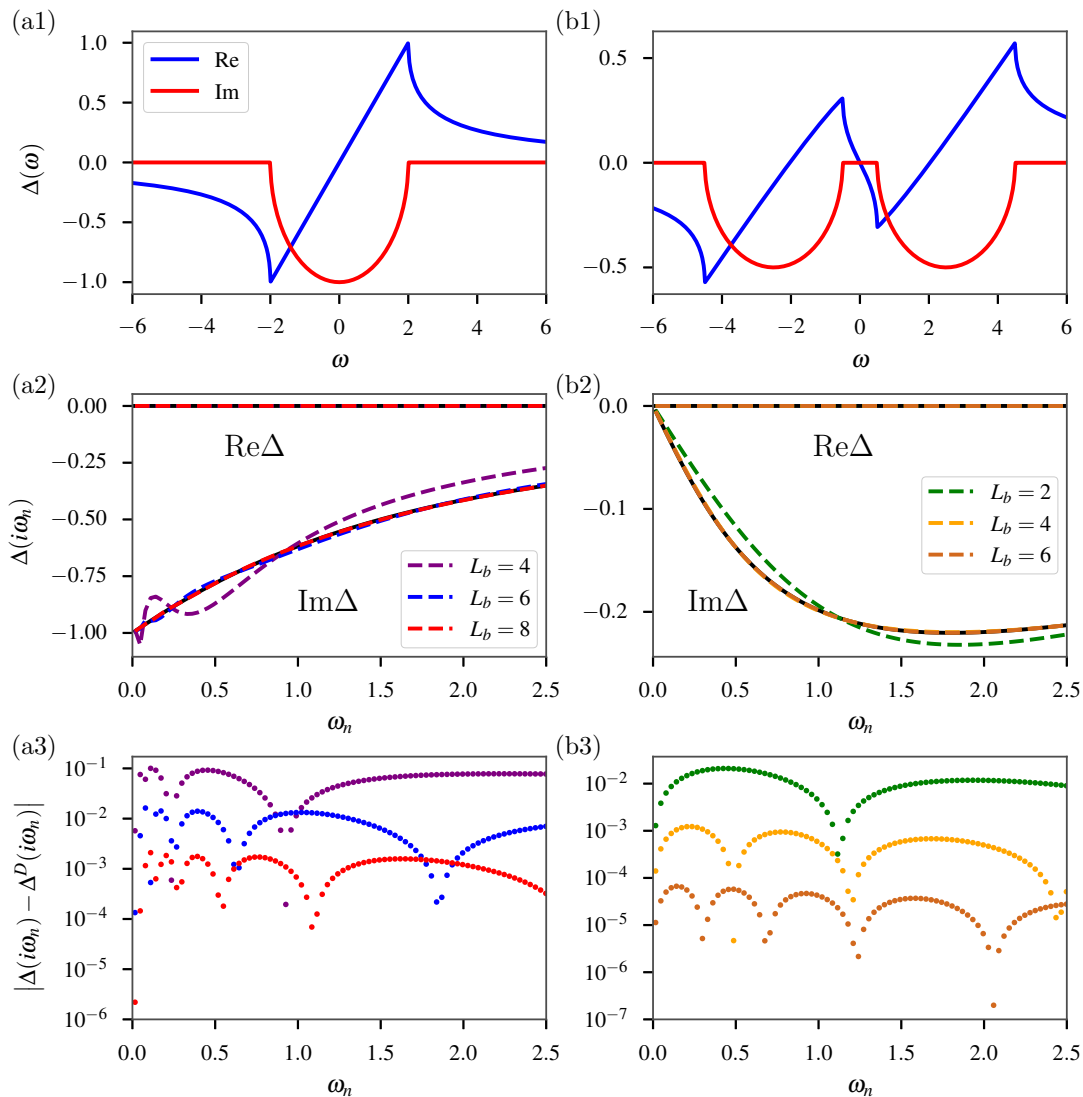


Figure 4.1: (a) Hybridisation for a semi circular density of states on the real axis (a1), when fit on the imaginary axis (a2) with varying number of bath sites  $L_b$  and the deviation from the exact hybridisation on the imaginary axis (a3). Panels (b1,b2,b3) show the same for a gapped hybridisation that consists of twice the hybridisation of a semi circular density of states once shifted to positive and once to negative frequencies. The fits have been made with  $\alpha = 1$  (a) and  $\alpha = 0$  respectively. Hybridisations with gap (b) are the typical case for insulators while gapless hybridisations (a) are the usual case for metals. The exact hybridisation in panels (a2, b2) is depicted by a black line, however as the higher accuracy fits are essentially on top it can not be seen.

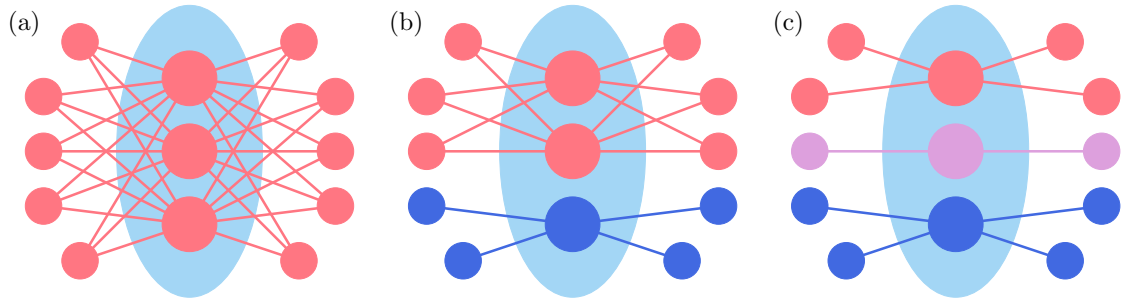


Figure 4.2: Pictorial representation of an impurity model with three impurities for the case of (a) a full matrix, (b) a block diagonal (one  $2 \times 2$  and one  $1 \times 1$  block) and (c) a diagonal hybridisation respectively. The big circles depict the impurity sites, while the small ones represent bath sites. Hopping is only allowed in between sites that are connected by a line.

use as many bath sites as possible to arrive at the best possible description. It should be noted at this point that there may be systems that are extremely complicated to compute on a tensor network level and do not allow for a large amount of bath sites. If one is faced with such a problem the algorithm can still be run with fewer number of bath sites, but special care should be given to the interpretation of results.

### 4.1.3 Block structure

As mentioned in the above section in the general case the hybridisation will be matrix-valued. However in almost all cases it will have a block diagonal form that is protected by the symmetry of the problem, e.g. a problem which is spin conserving will not have entries in the hybridisation that connect electrons with spin up and spin down character. This can and should be used as it is computationally far less demanding to fit multiple hybridisation functions with smaller matrix dimension. Also if the block structure is ignored, numerical errors might introduce small hopping elements that connect symmetry protected sectors, therefore destroying the initial symmetry of the system. This is especially detrimental when one afterwards wants to exploit the symmetry on a tensor network level.

In order to make this more clear we show a pictorial representation of the impurity models structure for the cases of a fully diagonal, a block diagonal and a full matrix hybridisation in Fig. 4.2. As can be seen from comparing the panels (a,b,c) the connectivity of the impurity problem largely depends on the shape of the hybridisation and it should therefore be accounted for by fitting disconnected blocks separately.

In fact a large class of problems has fully diagonal hybridisations allowing for every element to be fit separately which largely reduces the computational effort in the cost function optimization.

## 4.2 Ground State Search

Now that we have setup the Hamiltonian by determining the bath parameters  $\gamma_{ik}, \epsilon_k$  we can turn towards solving the impurity model. Our goal is to compute the Matsubara Green's function  $G(i\omega_n)$  which is the Fourier transform of the time ordered Green's function in imaginary time

$$G_{ij}(\tau) = -\Theta(\tau) \langle 0 | c_i(\tau) c_j^\dagger | 0 \rangle + \Theta(-\tau) \langle 0 | c_j^\dagger c_i(\tau) | 0 \rangle. \quad (4.21)$$

Here  $|0\rangle$  is the ground state of the impurity problem, which is why in a first step to obtain  $G(i\omega_n)$  we need to find  $|0\rangle$ .

This is achieved by applying DMRG (cf. Sec. 3.2), which however is a variational method. As mentioned in Sec. 3.5 in practice our impurity model will have multiple symmetries. Starting DMRG in a given symmetry sector yields the lowest energy eigenstate in that sector. Thus to make sure that we find the global ground state, we would have to search every single symmetry sector. Depending on the symmetry in question the number of sectors can however be very large, e.g. assume we have a system with a total number of  $L = 27$  sites as it is the case for a system with three impurities and  $L_b = 8$  per impurity. If we assume that we have the U(1) symmetries particle number ( $N$ ) and spin ( $S_z$ ) conservation then allowed sectors are

$$N \in \{0, \dots, 54\}, S_z \in \begin{cases} \{-\frac{N}{2}, \dots, \frac{N}{2}\} & \text{if } N \leq 27 \\ \{-\frac{54-N}{2}, \dots, \frac{54-N}{2}\} & \text{if } N > 27. \end{cases} \quad (4.22)$$

Already for this simple case the number of possibilities would be quite large (784 possibilities). So it is important to search many sectors in parallel as well as restrict their number by smart assumptions. For example, one can restrict the number of sectors significantly by solving the single particle part of the Hamiltonian. This makes it easy to obtain the number of occupied orbitals and therefore the particle number  $N_{\text{guess}}$  in the absence of interaction.

Afterwards one should still search a few particle number sectors around the guessed occupation number  $N_{\text{guess}}$ , however, so far we did not encounter a deviation larger than the maximal impurity occupation. An additional reasonable assumption can be made on the spin. Namely, when not treating a ferromagnetic system there should

usually be equally many up and down orbitals occupied. Thus it is a fair assumption to search only within sectors featuring small spin quantum numbers. When treating a new system it makes sense to include initially a large number of sectors and see for which typical spin quantum numbers the energy is rather low and then only search those. A reasonable guess is to restrict the spin quantum numbers to those of the impurity cluster. In the above example the maximal spin would be  $S_z = \frac{3}{2}$  due there being three impurity orbitals.

With these restrictions in place we would only need to search the sectors

$$N \in \{N_{\text{guess}} - 6, \dots, N_{\text{guess}} + 6\}, S_z \in \left\{ -\frac{3}{2}, -1, -\frac{1}{2}, 0, \frac{1}{2}, 1, \frac{3}{2} \right\}, \quad (4.23)$$

which amounts to a search in 54 sectors, assuming  $N_{\text{guess}}$  is even. If needed this can be further restricted as OTIS is designed such that the user can easily build in their own set of sectors they want to search in. However, 54 sectors are not really a problem when computing in parallel. OTIS allows for parallelisation both on the cores of a single machine and over multiple machines via the use of MPI (Message Passing Interface), which makes searches of rather large numbers of sectors feasible. Also after running a few iterations the sector does usually not change anymore, which could in principle be used to further restrict the above condition. In practice, we tend not to do this as we value the safety of searching a large number of sectors over the speed up. The symmetries implemented in OTIS so far are

Symmetry	quantum numbers
$U(1) \times (SU(2) \text{ or } U(1))$	$N, (S \text{ or } S_z)$
$U(1)^n \times (SU(2) \text{ or } U(1))$	$N_1, \dots, N_n, (S \text{ or } S_z)$
$\mathbb{Z}_2^n \times (SU(2) \text{ or } U(1))$	$P_1, \dots, P_n, (S \text{ or } S_z)$
$U(1)$	$N$

Here the  $U(1)^n$  symmetry is needed for particle number conservation in every band in case one treats multi-band problems with density-density interaction only. The  $\mathbb{Z}_2^n$  is necessary for multi-band problems where band parity is conserved, e.g. for Kanamori-type Hamiltonians [22]. Especially when treating symmetries that have an additional quantum number per band it becomes necessary to further reduce the sectors searched. One possibility is to restrict the search to identical band quantum numbers for degenerate bands. Once one has obtained a converged result it is good practice to check the sector by running another iteration on top allowing more sectors to make sure the correct one has been found.

After reading about the possible combinations of quantum numbers and all the sectors that have to be searched, the reader might be tempted to think that it might be

best to just run the computations with less symmetries. However, there are multiple reasons why including as many symmetries as possible is highly recommended. First of all DMRG is a variational method and not including some symmetry might lead to finding only a local minimum which in most cases renders the current DMFT iteration not only useless, but may destroy convergence. Second the block structure of all the dynamical quantities like the hybridisation  $\Delta(i\omega_n)$ , Green's function  $G(i\omega_n)$  and self-energy  $\Sigma(i\omega_n)$  are usually protected by the symmetries of the problem. Therefore not including a symmetry might wrongfully destroy the block structure. Last but not least there are problems that have degenerate ground states [94, 95]. Treating those appropriately is only possible if they are in different symmetry sectors, which might not be the case when one does not include all the symmetries of the problem. The treatment of degenerate ground states is also tied to the time-evolution that has to be performed upon excitations, which is why for now we close this section and postpone this discussion towards the end of the next section.

### 4.3 Time Evolution

Having obtained the ground state we can compute the time ordered Green's function of the impurity model as

$$G_{ij}(\tau) = -\Theta(\tau) \langle 0 | c_i(\tau) c_j^\dagger | 0 \rangle + \Theta(-\tau) \langle 0 | c_j^\dagger c_i(\tau) | 0 \rangle. \quad (4.24)$$

Here  $|0\rangle$  is the ground state and  $c_i$  ( $c_j^\dagger$ ) are the annihilation (creation) operators of electrons on the impurity site/orbital with index  $i$  ( $j$ ). The time dependence of  $c_i(\tau)$  is given by

$$c_i(\tau) = e^{\tau H} c_i e^{-\tau H}. \quad (4.25)$$

With this definition in place we obtain

$$G_{ij}(\tau) = -\Theta(\tau) \langle 0 | c_i e^{-\tau(H-E_0)} c_j^\dagger | 0 \rangle + \Theta(-\tau) \langle 0 | c_j^\dagger e^{\tau(H-E_0)} c_i | 0 \rangle. \quad (4.26)$$

Here we used, that the ground state is an eigenstate of the Hamiltonian and introduced the ground state energy  $E_0$ . For implementation purposes it is now useful to rephrase (4.26) in terms of time evolutions that have to be performed. Those are

$$|p_i\rangle(\tau) := e^{-\tau(H-E_0)} c_i^\dagger | 0 \rangle \quad (4.27)$$

$$|h_i\rangle(\tau) := e^{-\tau(H-E_0)} c_i | 0 \rangle. \quad (4.28)$$

We call  $|p_i\rangle$  ( $|h_i\rangle$ ) the imaginary time evolution of the particle (hole) excitation respectively. Inserting these excitations into (4.26) we obtain

$$G_{ij}(\tau) = -\Theta(\tau) \langle p_i | p_j(\tau) \rangle + \Theta(-\tau) \langle h_j | h_i(-\tau) \rangle \quad (4.29)$$

$$= -\Theta(\tau) \langle p_i | p_j(\tilde{\tau}) \rangle + \Theta(-\tau) \langle h_j | h_i(\tilde{\tau}) \rangle, \quad (4.30)$$

where we introduced  $\tilde{\tau} = |\tau|$  in the last line to further underline the direction in which the time evolution has to be taken. Namely, both particle and hole excitation have to be evolved forwards in imaginary time. This amounts to performing twice as many time evolutions as there are impurity sites. In order to keep this feasible it is very important to compute the time evolutions in parallel. To this aim OTIS distributes all time evolutions equally among machines that are used within MPI parallelisation and then further distributes all cores of said machines onto specific time evolutions. The overlaps are calculated on the fly during time evolution, however in some systems overlap computation may also be a bottle neck as during the time evolution only one core is used for the overlap calculations and there might be a large number of overlaps to compute depending on the matrix dimension of  $G(\tau)$ . Thus when all time evolution processes are finished the remaining overlaps get equally distributed over all cores and are then computed in parallel.

The careful reader may have realised that the time evolution operator  $e^{-\tau(H-E_0)}$  has only positive eigenvalues  $\lambda < 1$ , therefore leading to a decay in norm. As we are working at  $T = 0$  K we have to compute the time evolutions until the overlaps in (4.30) are well decayed. How fast this decay is, depends very heavily on the system at hand, as in essence we are applying the exponential of  $H - E_0$  onto the Hamiltonians single particle (hole) excitation subspace. This means that the rate of decay in essence corresponds to the size of the energy gap in between the ground state and the single particle (hole) excitation subspace. As we are simulating the problem on a finite size lattice the gaps are always finite. However, they are far larger in insulating systems than they are in metals.

In practice this means that we perform the time evolutions until the norm of the excitations is decayed under  $4 \times 10^{-8}$  or until some final time  $\tau_{\max}$  is reached. In typical insulating systems the first condition is usually met first, while in metallic systems the behaviour tends to be the other way around. If the final time condition is met and the norm is not sufficiently decayed we supplement the time evolution by a subsequent linear prediction [96].

How large one has to choose  $\tau_{\max}$  depends is problem dependent. However, in most applications  $\tau_{\max} = 200 \text{ eV}^{-1}$  was a sufficient abort condition. Whether or not  $\tau_{\max}$  is sufficient is best judged by comparing if the linear prediction does still change when  $\tau_{\max}$  is increased. An example can be seen in Fig. 4.3, which will be discussed in

more detail in Sec. 4.3.3. Finally having ensured proper decay, we perform a Fourier transformation to obtain  $G(i\omega_n)$ :

$$G(i\omega_n) = \int_{-\infty}^{\infty} e^{i\omega_n \tau} G(\tau) d\tau \quad (4.31)$$

### 4.3.1 Degenerate Blocks

In general the impurity problem has a Hamiltonian  $H$  of the form

$$H = \sum_{i,j,k,l \in I} V_{i,j,k,l} c_i^\dagger c_j^\dagger c_k c_l + \sum_{i,j \in I,B} T_{i,j} c_i^\dagger c_j, \quad (4.32)$$

where  $V$  and  $T$  are the two- and single-particle tensor, respectively, and  $I$  ( $B$ ) denotes the set of impurity (bath) sites. Every creation or annihilation operator changes the symmetry of the state in a well defined way.

As an example let us for simplicity consider a  $U(1) \times U(1)$  (particle number and spin) symmetric system with two impurities, then

$$I = \{(1, \uparrow), (1, \downarrow), (2, \uparrow), (2, \downarrow)\}. \quad (4.33)$$

Here, the first entry of each bracket is the orbital index while the second is the respective spin. We further assume  $T_{i,j}$  is such that there is hopping between impurities 1 and 2 but not between different spins as otherwise the spin  $U(1)$  symmetry would be broken. For the same reason  $V_{i,j,k,l}$  is also not allowed to modify a states spin. We can then label the ground state  $|0\rangle$  with its spin  $S_z$  and particle number  $N$  as those are conserved due to the symmetry

$$|0\rangle := |0, N, S_z\rangle. \quad (4.34)$$

With this definition in place we can write a slightly modified version of (4.26)

$$\begin{aligned} G_{ij}(\tau) &= -\Theta(\tau) \langle 0, N, S_z | c_i e^{-\tau(H-E_0)} c_j^\dagger | 0, N, S_z \rangle \\ &+ \Theta(-\tau) \langle 0, N, S_z | c_j^\dagger e^{\tau(H-E_0)} c_i | 0, N, S_z \rangle. \end{aligned} \quad (4.35)$$

We can again rephrase this in terms of the particle and hole excitations, however this time as we know that  $c_i$  annihilates a particle and changes the spin by  $\Delta S_z = \pm 0.5$  we can also label the excitations by their change of quantum numbers wrt. the ground state

$$\begin{aligned} G_{ij}(\tau) &= -\Theta(\tau) \langle p_i, 1, \Delta S_z^i | p_j(\tau), 1, \Delta S_z^j \rangle \\ &+ \Theta(-\tau) \langle h_j, -1, -\Delta S_z^j | h_i(-\tau), -1, -\Delta S_z^i \rangle. \end{aligned} \quad (4.36)$$

Note that also the time evolution does not change the quantum numbers as the time evolution operator can be written as a function of  $H$ . Therefore the above overlaps can only be finite if  $i, j$  are such that  $\Delta S_z^j = \Delta S_z^i$  leading to the following block structure of  $G(\tau)$

$$G(\tau) = \begin{pmatrix} G^\uparrow(\tau) & 0 \\ 0 & G^\downarrow(\tau) \end{pmatrix} \quad \text{with} \quad G^\sigma(\tau) = \begin{pmatrix} G_{1\sigma,1\sigma}(\tau) & G_{1\sigma,2\sigma}(\tau) \\ G_{2\sigma,1\sigma}(\tau) & G_{2\sigma,2\sigma}(\tau) \end{pmatrix}$$

This yields the two orbital subspaces  $\mathcal{S}_1 = \{(1, \uparrow), (2, \uparrow)\}$  and  $\mathcal{S}_2 = \{(1, \downarrow), (2, \downarrow)\}$ . If in addition the Hamiltonian is invariant under the exchange of  $\mathcal{S}_1$  and  $\mathcal{S}_2$  we know that

$$G^\uparrow(\tau) = G^\downarrow(\tau), \quad (4.37)$$

In which case we call the corresponding blocks in the Green's function degenerate. Such block degeneracies can be used to great efficiency as one can see in this example. Due to the equality of the two blocks, it is only necessary to compute one of them reducing the amount of time evolutions needed by a half. In practice, one should always make sure that the blocks are actually degenerate before reducing the number of time evolutions.

### 4.3.2 Treatment of degenerate ground states

In most systems strictly adhering to the above descriptions already results in the correct time-ordered Green's function  $G(\tau)$  at thermal equilibrium and  $T = 0$  K. However, in some systems there are multiple degenerate ground states [82, 94, 95] which makes it less straight forward to compute  $G(\tau)$ .

Even though the prescription that we are going to derive in this section has been applied in a specialised form in Refs. [82, 95], we are not aware of a published derivation. Thus we want to derive the procedure here.

To understand how the above algorithm has to be modified to account for degenerate ground states it is useful to go one step back and consider how one would in principle compute the Green's function at finite temperature

$$G_{i,j}^\beta(\tau) = -\Theta(\tau) \left\langle e^{\tau H} c_i e^{-\tau H} c_j^\dagger \right\rangle_\beta + \Theta(-\tau) \left\langle c_j^\dagger e^{\tau H} c_i e^{-\tau H} \right\rangle_\beta. \quad (4.38)$$

Here  $\beta$  is the inverse temperature and the expectation values have to be taken with respect to the Gibb's state at  $\beta$ :

$$\langle A \rangle_\beta := \frac{1}{Z_\beta} \text{Tr} (A e^{-\beta H}) \quad (4.39)$$

$$Z_\beta = \text{Tr} (e^{-\beta H}), \quad (4.40)$$

where  $A$  is an arbitrary operator. We are interested in the limit  $\beta \rightarrow \infty$ . In this limit the smallest energy contribution will dominate the partition sum  $Z_\beta$ . Thus it is useful to write

$$Z_\beta = \text{Tr} (e^{-\beta H}) = \text{Tr} (e^{-\beta(H-E_0)} e^{-\beta E_0}). \quad (4.41)$$

with  $E_0$  being the ground state energy. With this the expectation value  $\langle A \rangle_\beta$  becomes

$$\langle A \rangle_\beta = \frac{\text{Tr} (A e^{-\beta(H-E_0)})}{\text{Tr} (e^{-\beta(H-E_0)})} = \text{Tr} \left( A \frac{e^{-\beta(H-E_0)}}{\text{Tr} (e^{-\beta(H-E_0)})} \right). \quad (4.42)$$

Now using that  $e^{-\beta(H-E_0)}$  is diagonal in the eigenbasis of the Hamiltonian we can write

$$\langle A \rangle_\beta = \text{Tr} \left( A \frac{\sum_\lambda e^{-\beta(E_\lambda - E_0)} |\lambda\rangle \langle \lambda|}{\sum_\lambda e^{-\beta(E_\lambda - E_0)}} \right). \quad (4.43)$$

Taking the limit  $\beta \rightarrow \infty$  we obtain

$$\lim_{\beta \rightarrow \infty} \langle A \rangle_\beta = \frac{1}{N_{\text{deg}}} \sum_{\lambda: E_\lambda = E_0} \langle \lambda | A | \lambda \rangle \quad (4.44)$$

where  $N_{\text{deg}}$  is the number of degenerate ground states. As we can see from (4.44) the correct way to compute the expectation value is to evaluate it wrt. a equally weighted mixed superposition of the degenerate ground states.

Computing an expectation value like (4.44) is only possible if in every symmetry sector there is at maximum one state with energy  $E_0$ . This is what we call a scenario where we can *resolve* the ground state degeneracy within our symmetry. Otherwise it is impossible to build an exactly equally weighted superposition as in principle we would already obtain a random superposition of degenerate ground states out of a sector that contains more than one state with energy  $E_0$ .

From the above expression one might now expect that one has to compute  $G(\tau)$  for every single ground state therefore making the computation  $N_{\text{deg}}$  times more

expensive. However as before, the implemented symmetries come to our rescue: As mentioned in the last section the application of  $c_i$  ( $c_i^\dagger$ ) changes the quantum numbers in a well defined way and as all the states in (4.44) are in different symmetry sectors we can as well compute the expectation value by a single pure state, namely

$$|\Psi\rangle = \frac{1}{\sqrt{N_{\text{deg}}}} \sum_{\lambda: E_\lambda = E_0} |\lambda\rangle. \quad (4.45)$$

With this state we can now compute  $G(\tau)$  as

$$G_{ij}(\tau) = -\Theta(\tau) \langle \Psi | c_i e^{-\tau(H-E_0)} c_j^\dagger | \Psi \rangle + \Theta(-\tau) \langle \Psi | c_j^\dagger e^{\tau(H-E_0)} c_i | \Psi \rangle. \quad (4.46)$$

Writing this expression in terms of the states  $|\lambda\rangle$  and introducing an additional quantum number label  $Q$  we obtain:

$$\begin{aligned} G_{ij}(\tau) = & - \Theta(\tau) \frac{1}{N_{\text{deg}}} \sum_{\lambda, \lambda'} \langle \lambda', Q_{\lambda'} | c_i e^{-\tau(H-E_0)} c_j^\dagger | \lambda, Q_\lambda \rangle \\ & + \Theta(-\tau) \frac{1}{N_{\text{deg}}} \sum_{\lambda, \lambda'} \langle \lambda', Q_{\lambda'} | c_j^\dagger e^{\tau(H-E_0)} c_i | \lambda, Q_\lambda \rangle \end{aligned} \quad (4.47)$$

The expectation values in the above equation are only finite when one of the following cases holds

$$G_{ij}(\tau) \neq 0 \quad \text{if} \quad \begin{cases} Q_\lambda = Q_{\lambda'} \wedge \Delta Q_i = \Delta Q_j \\ Q_\lambda \neq Q_{\lambda'} \wedge \Delta Q_i \neq \Delta Q_j, \end{cases} \quad (4.48)$$

where we introduced the quantum number change induced by  $c_i$  as  $\Delta Q_i$ . This means that the only mixed terms, that can arise by using the pure superposition (4.45) instead of the mixed one (4.44) violate the block structure that is enforced by the symmetry. These violations can however easily be identified and discarded by simply ignoring contributions outside of the block structure.. All finite contributions within the block structure are then guaranteed to be equal to a computation wrt. a mixed superposition.

### 4.3.3 Linear Prediction

As mentioned before in metallic systems one usually stops the time evolution at some  $\tau_{\text{max}}$  at which the Green's function is not yet fully decayed. Performing a Fourier

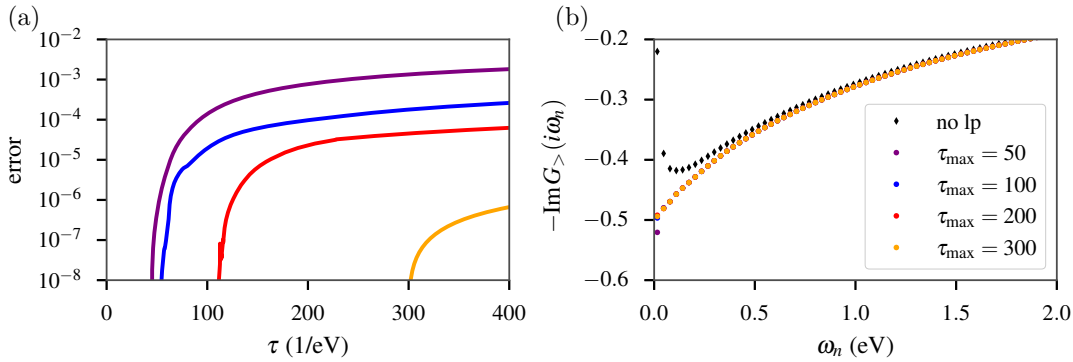


Figure 4.3: Linear prediction error and its influence on the corresponding Green's function  $G_{>}(i\omega_n)$  for different maximally reached times  $\tau_{\max}$  in time evolution. The calculation was done wrt. a single band Bethe lattice with 4 eV bandwidth.  $G_{>}(\tau) = \langle p_i | p_j(\tau) \rangle$  is the particle part of (4.30) and  $G_{>}(i\omega_n)$  (b) is its Fourier transform. The error (a) is given with respect to a time evolution with  $\tau_{\max} = 400 \text{ eV}^{-1}$ . The black diamonds in panel (b) correspond to a time evolution with  $\tau_{\max} = 400 \text{ eV}^{-1}$  without supplementary linear prediction.

transform upon a not fully decayed function yields deviations at low frequencies and might induce oscillations in  $G(i\omega_n)$  as the long time limit in essence gets cut off and thus  $G(i\omega_n)$  becomes a step function. For this reason we use linear prediction [96] to further predict the long time behaviour of  $G(\tau)$ .

For illustration we show in Fig. 4.3 a comparison between time evolutions until different maximal times  $\tau_{\max}$ . In panel (a) we can see how the prediction compares to an actual time evolution and find that in the case at hand it seems to be sufficient to perform a time evolution until  $\tau_{\max} = 100 \text{ eV}^{-1}$  as the error drops under  $10^{-3}$ . Of course longer times tend to yield an improvement. In panel (b) we compare the resulting Fourier transforms and find that indeed the only computation that gives a major deviation in the lowest frequency point is the one with  $\tau_{\max} = 50 \text{ eV}^{-1}$ . All the other calculations agree very well (up to  $\mathcal{O}(10^{-3})$ ). Most importantly, we can see that the calculation until  $\tau_{\max} = 400 \text{ eV}^{-1}$  does yield major deviations if no prediction is used. This leads us to the conclusion that we have to use linear prediction to ensure capturing low frequency behaviour correctly.

The following derivation can quite similarly be found in Ref. [96], but for completeness we also want to present it here.

Linear prediction takes a data set  $x_j = x(t_j)$  on a linearly spaced time grid  $t_j = j\Delta t$  and extends it further by fitting exponentials of the form  $\alpha e^{(i\omega+\eta)t}$  with  $\alpha \in \mathbb{C}$  and

$\omega, \eta \in \mathbb{R}$  to the data  $x_j$ . To achieve this we make the ansatz

$$\tilde{x}_n = - \sum_{i=0}^p a_i x_{n-i} \quad (4.49)$$

where  $\tilde{x}$  is the value for the time step that is to be determined given the last  $p$  time steps. Now one can determine the coefficients  $a_i$  by minimizing the cost function  $\chi$  over a fit interval

$$\chi(a) = \sum_{n \in I_{\text{fit}}} |\tilde{x}_n - x_n|^2 \quad (4.50)$$

Here we denoted by  $I_{\text{fit}}$  the fit interval. The coefficients  $a$  can now be obtained by simply taking the derivative of  $\chi(a)$  wrt.  $a_i^*$

$$\frac{\partial \chi}{\partial a_i^*} = \sum_{j=1}^p \sum_{n \in I_{\text{fit}}} x_{n-i}^* x_{n-j} a_j + \sum_{n \in I_{\text{fit}}} x_{n-i}^* x_n \stackrel{!}{=} 0 \quad (4.51)$$

This can be phrased as linear system of equations

$$Ra = -r \quad (4.52)$$

with  $R_{ij} = \sum_{n \in I_{\text{fit}}} x_{n-i}^* x_{n-j}$  and  $r_i = \sum_{n \in I_{\text{fit}}} x_{n-i}^* x_n$ . Solving this system of equations we obtain  $a_i$ , which we can, in principle, use to compute the predicted time series by the relation (4.49). However it might be useful to instead extract some more information about the form that time series will take. To this aim we define

$$A = \begin{pmatrix} -a_1 & -a_2 & -a_3 & \dots & -a_p \\ 1 & 0 & 0 & \dots & 0 \\ 0 & 1 & 0 & \dots & 0 \\ \vdots & \ddots & \ddots & \ddots & \vdots \\ 0 & \dots & 0 & 1 & 0 \end{pmatrix} \quad (4.53)$$

and using  $x_n := (x_{n-1}, \dots, x_{n-p})^T$  we can write

$$\tilde{x}_{n+1} = A\tilde{x}_n. \quad (4.54)$$

It is now useful to decompose  $A$  into its right eigenvectors. Let  $\alpha_i$  be the (possibly complex) eigenvalues of  $A$  and  $Y$  the matrix of right eigenvectors, then

$$\begin{aligned} \tilde{x}_{n+m} &= (A^m x_n)_1 = (A^m Y Y^{-1} x_n)_1 \\ &= (Y d_A^m Y^{-1} x_n)_1 = \sum_{i=1}^p \alpha_i^m c_i \end{aligned} \quad (4.55)$$

with  $c_i = Y_{1i}(Y^{-1}x_n)_i$ . As we expect the time series to decay we would expect to only obtain eigenvalues  $\alpha_i$  such that  $|\alpha_i| < 1$ , however, in practice this is not the case. Thus to ensure decay, we set  $c_i \rightarrow 0$  if  $|\alpha_i| \geq 1$ . Note however, that since the fit resulted in those finite weights  $c_i$ , setting them to 0 will induce a discontinuity. It is therefore advised to compute the fraction of weight that has been discarded as an error measure

$$w = \frac{\sum_{i:|\alpha_i|\geq 1} |c_i|}{\sum_{i=1}^p |c_i|}. \quad (4.56)$$

If the fraction of discarded weight  $w$  is too large it is reasonable to discard the prediction and try again with different parameters as a significant discontinuity will lead to an error in  $G(i\omega_n)$ . The main parameters that can be chosen for linear prediction are the number of points to be fitted  $N_{\text{fit}}$ , the index of the time where the predicted time series is supposed to start  $N_{\text{obs}}$  and the number of exponentials ( $\alpha_i^m$ ) that is used for the extrapolation  $p$ .

In case one chooses  $N_{\text{obs}}$  smaller than the last time step in the unpredicted time series, it is important to discard all time points later than  $x_{N_{\text{obs}}}$  as otherwise a discontinuity may be introduced, which again leads to oscillations in  $G(i\omega_n)$ .

As not every time series is the same, and usually over the course of multiple iterations the shape of the time series can change quite significantly, it might not be wise to fix the parameters  $N_{\text{fit}}$ ,  $N_{\text{obs}}$  and  $p$  for an entire DMFT calculation. A better approach is to optimize those parameters dependent on the to be predicted time series  $x_n$ . To this aim we compute an in sample error

$$\epsilon = \|x_{N_{\text{obs}}} - \tilde{x}_{N_{\text{obs}}}^{\text{err}}\|_{\infty}. \quad (4.57)$$

Here  $\tilde{x}^{\text{err}}$  is computed starting from the last point before the fit interval so that  $\epsilon$  corresponds to the difference of the actual values in the fit interval to the case where one would predict the data within from the  $p$  data points prior to the fit interval. The norm  $\|\cdot\|_{\infty}$  is defined as the maximum distance in a single element of the vector.

With this we have obtained two distinct measures for the quality of a prediction. Namely, the in sample error  $\epsilon$  and the discarded weight fraction  $w$ . Using those we define a cost function that is supposed to be optimized

$$\chi(N_{\text{fit}}, N_{\text{obs}}, p) = \max(\epsilon(N_{\text{fit}}, N_{\text{obs}}, p), w(N_{\text{fit}}, N_{\text{obs}}, p)). \quad (4.58)$$

The problem with the optimization of this cost function is that it takes integers as input, which makes most of the available standard optimization routines difficult to use. Due to this problem we designed our own optimizer.

The optimizer works by performing a random walk through parameter space, adjusting the maximally allowed step size once some maximal number of steps (in practice  $\mathcal{O}(100)$ ) has been reached. The steps are taken in random directions in parameter space with random step size smaller than the maximum step that is currently allowed. When adjusting the step size the new random walk starts from the optimum that has so far been found. The optimizer stops when the step size has become zero in every direction. This procedure is run in parallel on every core of the master node for the DMFT run, resulting usually in 32 independent random walks. In the end the best result is chosen for the actual prediction.

The entire linear prediction algorithm can be extended to matrix valued functions by replacing the values at every time step in (4.50) with matrices and the norm by the Frobenius norm. Assume that instead of a scalar time series we insert a matrix of dimensions  $L \times L$  then the system of equations for determining  $a$  stays formally the same however the definitions of  $R$  and  $r$  change

$$R_{ij}^{\text{mat}} = \sum_{k,l=1}^L \sum_{n \in I_{\text{fit}}} (x_{n-i}^{kl})^* x_{n-j}^{kl} \quad (4.59)$$

$$r_i^{\text{mat}} = \sum_{k,l=1}^L \sum_{n \in I_{\text{fit}}} (x_{n-i}^{kl})^* x_n^{kl}. \quad (4.60)$$

With these new definitions we can then define the matrix  $A$  as above, however, this time the weights of the eigenvectors are going to be matrix valued. They can be computed as  $(c_i^{\text{mat}})^{kl} = Y_{1i}(Y^{-1}(x_n)^{kl})$ . Here again  $x_n$  is a vector of matrices and the weights are computed element wise. We define the fraction of discarded weight  $w^{\text{mat}}$  and the prediction error  $\epsilon^{\text{mat}}$  as

$$w^{\text{mat}} = \frac{\sum_{i:\alpha_i \geq 1} \sum_{k,l=1}^L |c_i^{kl}|}{\sum_{i=1}^p \sum_{k,l=1}^L |c_i^{kl}|} \quad (4.61)$$

$$\epsilon^{\text{mat}} = \max_{kl} \left\| (x_{N_{\text{obs}}})^{kl} - (\tilde{x}_{N_{\text{obs}}}^{\text{err}})^{kl} \right\|_{\infty} \quad (4.62)$$

Note how the extension to matrices is written such that all the definitions reduce to the scalar version when  $L = 1$  as such it seems like a natural extension. In practice the idea would be to use the matrix valued algorithm in cases where the offdiagonals are slowly decaying or initially increasing as with the additional information from the diagonals we may have a better chance in predicting the correct behaviour. The algorithm is implemented in our toolkit, however, since we did not encounter any good use cases since its implementation it is largely untested.

## 4.4 Self-Energy

In the end, what the impurity solver needs to provide to the DMFT self-consistency loop is the self-energy of the impurity system  $\Sigma(i\omega_n)$  as it is needed to compute the local Green's function of the lattice system within the local self-energy approximation  $G_{\text{loc}}(i\omega_n) = \sum_{k \in \text{1.BZ}} (\mathbb{1}(i\omega_n + \mu) - H_k - \Sigma(i\omega_n))^{-1}$ . The most straight forward way to obtain the self-energy is to use Dyson's equation [64]

$$\Sigma(i\omega_n) = \mathcal{G}(i\omega_n)^{-1} - G(i\omega_n)^{-1}. \quad (4.63)$$

Here,  $\mathcal{G}(i\omega_n)$  is the non-interacting impurity Green's function and its inverse is given by

$$\mathcal{G}^{-1}(i\omega_n) = \mathbb{1}(i\omega_n + \mu) - \xi - \Delta(i\omega_n), \quad (4.64)$$

with  $\xi$  being the single particle Hamiltonian on the impurity and  $\Delta(i\omega_n)$  the hybridisation. In principle, one has a choice, namely one could either use the continuous hybridisation or the discrete version  $\Delta_{ij}^D(i\omega_n) = \sum_l \frac{\gamma_{il}\gamma_{jl}^*}{i\omega_n - \epsilon_l}$  as introduced in Sec. 4.1. We highly recommend the discretized version  $\Delta_{ij}^D(i\omega_n)$  as it is the hybridisation that actually corresponds to the model that was solved within DMRG. If one uses the continuous version one does not obtain the self-energy of the discretized problem nor does one get the the self-energy corresponding to the continuous problem that is to be approximated but something in between.

It should be mentioned, that even when one uses the discrete version the self-energy  $\Sigma(i\omega_n)$  might become unphysical at large frequencies  $\omega_n$ . This is due to the fact that both  $\mathcal{G}(i\omega_n)$  and  $G(i\omega_n)$  are numerical quantities which decay at large frequencies. Thus taking the difference of their inverses tends to blow up the error which can lead to unphysical positive imaginary parts on the diagonal of  $\Sigma(i\omega_n)$ .

Depending on the quantities of interest this may or may not be a problem. If one is for example only interested in  $G_{\text{loc}}(i\omega_n)$  this is not really a problem as in the limit of large  $\omega_n$  the diagonal is anyway dominated by  $i\omega_n$  so that small positive values of  $\Sigma(i\omega_n)$  do not make a difference. However, if the desired quantity is  $\Sigma(i\omega_n)$  itself, it may be desirable to avoid this problem by having a more numerically stable way of computing  $\Sigma(i\omega_n)$ . In order to achieve this Bulla *et al.*[97] introduced an additional correlator  $\Gamma(i\omega_n)$  with which the self-energy can be computed as matrix product of  $\Gamma(i\omega_n)$  and  $G^{-1}(i\omega_n)$ . As the original work [97] concerns itself specifically with the Hubbard model but we might also be interested in other interaction Hamiltonians, we will derive the form of  $\Gamma(i\omega_n)$  for a general impurity model with two-particle term  $V$  in the following.

### 4.4.1 The $V$ -Correlator

This derivation is relatively similar to the solution of the non-interacting AIM in Sec. 4.1 with the only difference that this time  $V \neq 0$ . From now on for simplicity when we denote no indices, then  $V$  will be defined as:

$$V = \sum_{i,j,n,m} V_{ijnm} c_i^\dagger c_j^\dagger c_n c_m \quad (4.65)$$

Repeating the steps in Sec. 4.1 the time derivative of  $G_{ij}(\tau)$  is given by

$$\frac{\partial G_{ij}}{\partial \tau}(\tau) = -\delta(\tau)\delta_{ij} - \sum_{k \in B} \gamma_{ik} G_{kj}(\tau) - \sum_{l \in I} \xi_{il} G_{lj}(\tau) + \Gamma_{ij}(\tau) \quad (4.66)$$

with

$$\Gamma_{ij}(\tau) := -\Theta(\tau) \langle 0 | [V, c_i](\tau) c_j^\dagger | 0 \rangle + \Theta(\tau) \langle 0 | c_j^\dagger [V, c_i](\tau) | 0 \rangle. \quad (4.67)$$

The equation of motion for the mixed bath-impurity Green's function  $G_{kj}(\tau)$  is the same as in the non-interacting case because  $V$  only acts on the impurity

$$\frac{\partial G_{kj}}{\partial \tau}(\tau) = - \sum_{i \in I} \gamma_{ik}^* G_{ij}(\tau) - \epsilon_k G_{kj}(\tau) \quad (4.68)$$

Now we can compute the Fourier transform of equations (4.67) and (4.68) to obtain

$$\begin{aligned} -i\omega_n G_{ij}(i\omega_n) = & - \delta_{ij} - \sum_{k \in B} \gamma_{ik} G_{kj}(i\omega_n) - \sum_{l \in I} \xi_{il} G_{lj}(i\omega_n) \\ & + \Gamma_{ij}(i\omega_n) \end{aligned} \quad (4.69)$$

$$-i\omega_n G_{kj}(i\omega_n) = - \sum_{l \in I} \gamma_{lk}^* G_{lj}(i\omega_n) - \epsilon_k G_{kj}(i\omega_n). \quad (4.70)$$

This can be decoupled in exactly the same way as in Sec. 4.1 and after some algebra we obtain the relation

$$-i\omega_n G_{ij}(i\omega_n) = -\delta_{ij} - \sum_{l \in I} (\Delta_{il}^D(i\omega_n) + \xi_{il}) G_{lj}(i\omega_n) + \Gamma_{ij}(i\omega_n). \quad (4.71)$$

Shifting the identity to the left and the term proportional to  $i\omega_n$  to the right side of the equation, we multiply by  $\mathcal{G}^{-1}$  to obtain

$$(G^{-1})_{ij} = i\omega_n \delta_{ij} - \Delta_{ij}^D(i\omega_n) - \xi_{ij} + \sum_{l \in I} \Gamma_{il}(i\omega_n) (G^{-1}(i\omega_n))_{lj}. \quad (4.72)$$

Identifying  $(G^0(i\omega_n)^{-1})_{ij} = i\omega_n\delta_{ij} - \Delta_{ij}^D(i\omega_n) - \xi_{ij}$  yields

$$(G^0(i\omega_n)^{-1})_{ij} - (G^{-1})_{ij} = - \sum_{l \in I} \Gamma_{il}(i\omega_n)(G^{-1}(i\omega_n))_{lj}. \quad (4.73)$$

But the left side of this equation is nothing else than Dyson's equation and therefore the self-energy is given by

$$\Sigma(i\omega_n) = -\Gamma(i\omega_n)G^{-1}(i\omega_n) \quad (4.74)$$

with

$$\begin{aligned} \Gamma_{ij}(i\omega_n) = & - \int d\tau e^{i\omega_n\tau} \Theta(\tau) \langle 0 | [V, c_i](\tau) c_j^\dagger | 0 \rangle \\ & + \int d\tau e^{i\omega_n\tau} \Theta(-\tau) \langle 0 | c_j^\dagger [V, c_i](\tau) | 0 \rangle. \end{aligned} \quad (4.75)$$

Please note that to compute this correlator one does not need to perform more time evolutions but merely additional overlaps. However, as  $\Gamma(i\omega_n)$  is a different correlator it may decay with a different rate than  $G(i\omega_n)$  possibly introducing a need for longer time evolutions. This behaviour can differ from system to system.

## 4.5 Calculations at fixed impurity occupation

The standard DMFT procedure works at fixed chemical potential  $\mu$  which then leads to some total occupation number on the impurity cluster. It might be desirable however to compute directly at a fixed particle number  $n$  and determine  $\mu$  such that this occupation is realised.

As we will explain in the next section, the local occupation number can be computed from the local Green's function  $G_{\text{loc}}(i\omega_n) = \sum_{k \in \text{1.BZ}} (\mathbb{1}(i\omega_n + \mu) - H_k - \Sigma(i\omega_n))^{-1}$ . The idea is therefore to start at some chemical potential  $\mu_0$ , compute the occupation number and adjust  $\mu$  depending on if it is higher or lower than the target density [98]. In essence this is a bisection of  $n(\mu)$  for a given hybridisation  $\Delta(i\omega_n)$  and self-energy  $\Sigma(i\omega_n)$ . The result of this bisection procedure is a guessed chemical potential  $\mu_{\text{guess}}$  such that the occupation number extracted from  $G_{\text{loc}}(i\omega_n)$  equals our target density  $n$ . Note that this is approximative because  $\Sigma(i\omega_n)$  was computed at a certain chemical potential and therefore changing  $\mu$  would also change  $\Sigma(i\omega_n)$ , which we ignore. Within a single iteration of DMFT this procedure simultaneously yields an update in  $\Delta(i\omega_n)$  and  $\mu$ . Therefore only when  $\mu$  converges,  $\Delta(i\omega_n)$  will. This can be problematic when trying to apply the procedure to an insulating calculation as there will be

multiple chemical potentials yielding the same or very similar occupation numbers, which may result in jumping chemical potentials. In order to get this under control one eventually has to fix the chemical potential to a value yielding the correct target density.

### 4.5.1 Tail fitting

In the last section we mentioned that it was possible to extract the occupation numbers of a system out of its Green's function. The easiest way to do this is by using the time ordered Green's function  $G(\tau)$

$$G(\tau) = -\Theta(\tau) \langle 0 | c(\tau) c^\dagger | 0 \rangle + \Theta(-\tau) \langle 0 | c^\dagger c(\tau) | 0 \rangle. \quad (4.76)$$

Here we suppressed all indices as we are right now only interested in diagonal components. Evaluating this expression at  $\tau = 0^-$  we find

$$G(\tau = 0^-) = \langle 0 | c^\dagger c | 0 \rangle \quad (4.77)$$

Unfortunately in many cases we do not have direct access to the time ordered Green's function but only to its Fourier transform  $G(i\omega_n)$ . Thus we need to perform a Matsubara frequency summation

$$G(\tau) = \frac{1}{\beta} \sum_n G(i\omega_n) e^{-i\omega_n \tau}. \quad (4.78)$$

Here the  $\beta$  usually corresponds to the temperature the Green's function is computed at, in our case this would be  $\beta = \infty$  as we are working at  $T = 0$  K. However as we are using an artificial  $\beta$  for the frequency discretization we will also use it here. In practice if  $\beta$  is chosen high enough ( $\beta \approx 100 - 200 \text{eV}^{-1}$ ) the summation does yield very good results even though performed as for finite temperatures.

Performing the sum in (4.78) is somewhat tricky as the Green's function  $G(i\omega_n)$  has a infinitely long high frequency tail, while we only have access to a finite number of data points. The idea is to fit the high frequency behaviour of  $G(i\omega_n)$  and separate  $G(i\omega_n) = \tilde{G}(i\omega_n) + G_{\text{tail}}(i\omega_n)$ , where  $\tilde{G}(i\omega_n)$  does now only have finite support and  $G_{\text{tail}}(i\omega_n)$  is known analytically [99, 100]

$$G_{\text{tail}}(i\omega_n) = \sum_k a_k \frac{1}{i\omega_n - b_k}, \quad (4.79)$$

where  $a_k$  and  $b_k$  are parameters. Interestingly,  $a_k$  and  $b_k$  can be related to the high frequency moments of the Green's function by defining  $u = \frac{1}{i\omega_n}$  and computing

$$\mu_n = \frac{1}{n!} \lim_{u \rightarrow 0} \frac{\partial^n}{\partial u^n} G(1/u) = \frac{1}{n!} \lim_{u \rightarrow 0} \frac{\partial^n}{\partial u^n} \sum_k a_k \frac{u}{1 - b_k u} \quad (4.80)$$

$$\mu_n = \begin{cases} \sum_k a_k b_k^{n-1} & \text{if } n > 0 \\ 0 & \text{else.} \end{cases} \quad (4.81)$$

Here (4.81) can be shown rather straight forward by induction. The connection between the moments  $\mu_n$  and the  $a_k$  and  $b_k$  is very useful as we may obtain the moments from a least square fitting problem

$$\chi = \sum_n \left| G(i\omega_n) - \sum_{k=1}^M \mu_k \frac{1}{(i\omega_n)^k} \right|^2 \quad (4.82)$$

where  $M$  denotes the maximal amount of moments taken into consideration and  $\chi$  is to be minimized. As the ansatz is linear in  $\mu_n$  we can again reduce the minimization to solving a linear system of equations

$$A\mu = c \quad (4.83)$$

$$c_k = \sum_n \frac{G(i\omega_n)}{(-i\omega_n)^k} \quad (4.84)$$

$$A_{kj} = \sum_n \frac{1}{(-1)^k (i\omega_n)^{k+j}}. \quad (4.85)$$

Having determined  $\mu_n$  we can obtain the tail Green's function by choosing arbitrary poles  $b_k$  on the positive and negative axis. In praxis we took integers  $b_k \in \{0, -1, 1, -2, 2, \dots\}$ . From (4.81) we can read off

$$\mu = Va \quad (4.86)$$

$$V_{kl} = b_l^{k-1} \quad (4.87)$$

Thus, we can obtain  $a_k = (V^{-1}\mu)_k$ , and determine  $G_{\text{tail}}(i\omega_n)$  which we now have to perform an analytic Matsubara summation on

$$G_{\text{tail}}(\tau = 0^-) = \lim_{\tau \uparrow 0^-} \frac{1}{\beta} \sum_n G_{\text{tail}}(i\omega_n) e^{-i\omega_n \tau} \quad (4.88)$$

$$= \lim_{\tau \uparrow 0^-} \oint_C dz G_{\text{tail}}(z) n_F(z) e^{-z\tau} \quad (4.89)$$

$$= \sum_k a_k \frac{1}{1 + e^{\beta b_k}}. \quad (4.90)$$

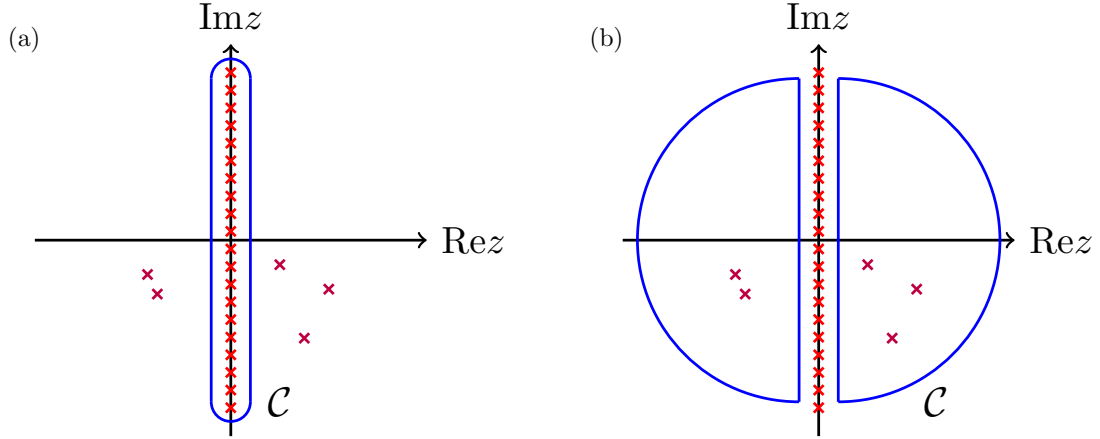


Figure 4.4: Contour  $\mathcal{C}$  in the complex plane enclosing the poles of the weighting function  $n_F(z) = \frac{1}{1+e^{\beta z}}$  (a) and deformed to enclose the poles of  $G_{\text{tail}}(z)$  (b). All lines are meant to extend to infinity and the circles are supposed to have infinite radius. The lines that are at infinite distance can be added or removed at will as those have no weight in the integral (4.89) due to the choice of  $n_F(z)$ . This makes the deformation from (a) to (b) possible without changing the value of the integral. The poles of  $n_F(z)$  and  $G_{\text{tail}}(z)$  are depicted as red and purple crosses respectively.

Here  $n_F(z) = \frac{1}{1+e^{\beta z}}$  is the Fermi-Dirac distribution that is used as a weighting function both to introduce poles at the Matsubara frequencies and to make the integrand vanish as  $|z| \rightarrow \infty$ . The steps in between equations (4.88, 4.89, 4.90) involve complicated manipulations. In the first step we are introducing  $n_F(z)$  that has its poles exactly at the Matsubara frequencies and therefore the integral over the contour enclosing those poles (cf. 4.4 (a)) is equal to the Matsubara summation. We then deform the contour to enclose the poles of  $G_{\text{tail}}(z)$ . This is possible as the Fermi-Dirac distribution and the term  $e^{-z\tau}$  ensure that the integrand vanishes in the limit  $|z| \rightarrow \infty$  when  $\tau$  is negative. Therefore we can add and remove contours at infinite radius for free. With this deformation we can conclude that the integral is also equal to the sum over the residues of the poles of  $G_{\text{tail}}(z)$  and therefore end up with (4.90), i.e. the contribution coming from the tail. In order to obtain the occupation number we now need to add the contribution of the Green's function  $\tilde{G}(i\omega_n)$

$$\langle 0 | c^\dagger c | 0 \rangle = \frac{1}{\beta} \sum_n \tilde{G}(i\omega_n) + \sum_k a_k \frac{1}{1 + e^{\beta b_k}} \quad (4.91)$$

Here the remaining Matsubara summation should only have finite support (as we subtracted the tail) and thus it can be carried out numerically. This entire procedure depends very much on the fact that  $G(i\omega_n)$  can be fitted well, if this is not the case, then the occupation number obtained may be wrong. In practice, we fit  $M = 10$  moments  $\mu_n$  to the last 20% of  $G(i\omega_n)$  data which tended to yield good results at auxiliary  $\beta = 200 \text{ eV}^{-1}$  and 1025 frequency points. Within the projects treated in the context of this thesis we used both our own implementation of the above mentioned method and the TRIQS implementation [99, 100]. However, when working with the latter (in the BaOsO<sub>3</sub> project) we simply used the default parameters which amounts to  $M = 3$  moments.

## 4.6 Analytic Continuation

The single particle Green's function is analytic on the upper half of the complex plane [101], which means in principle the real axis and imaginary axis data contains the same information. Even though many interesting quantities like polarizations, mass enhancement and in principle all single particle static quantities can be computed on the imaginary axis, sometimes the quantity of interest lies on the real axis. An example would be the (momentum resolved) spectral function that can be used, e.g. to compare to ARPES, where it is the quantity that is measured.

The transformation from the real axis to the imaginary axis is given by [102]

$$G(i\omega_n) = \int_{\mathbb{R}} d\omega \frac{A(\omega)}{i\omega_n - \omega} \quad (4.92)$$

where  $A(\omega) = -\frac{1}{\pi} \text{Im}G(\omega)$  is the spectral function belonging to  $G(z)$ . In principle the above can be interpreted as a matrix equation

$$G(i\omega_n) = \frac{\omega_{\max} - \omega_{\min}}{N_\omega} \sum_k \frac{A(\omega_k)}{i\omega_n - \omega_k} \quad (4.93)$$

$$= \sum_k K_{nk}^\omega A(\omega_k) \quad (4.94)$$

where we introduced a discretization  $\omega_k$  of the real frequency axis with  $\omega_{\max}$  and  $\omega_{\min}$  defining the boundary of the support of  $A(\omega)$ . Now the only remaining task would be to invert the kernel  $K^\omega$ , however this problem is numerically ill-conditioned and therefore a direct inversion is bound to lead to unreasonable results. The reason for this ill-conditioning can intuitively be understood from (4.92) which is in essence

nothing other than a sum over  $(i\omega_n - \varepsilon_k)^{-1}$  where  $\varepsilon_k$  are all the eigen energies in the single particle excitation subspace of the Hamiltonian. While on the real axis those summands are extremely peaked functions, on the Matsubara axis they are very smooth. Thus the information about the pole structure is smoothed out and in essence partially lost due to numerical accuracy.

It is for this reason that there exist many different analytic continuation algorithms, e.g. Pade approximants [103], Nevanlinna [104] and the maximum entropy method [105, 106]. All these methods come with parameters that one can fine tune to obtain more reasonable analytic continuations. The problem is that all of them might look different on the real axis due to the suppression of information when encoded on the Matsubara axis. When performing analytic continuations one should therefore make sure to vary the parameters used until the result seems rather stable against parameter change. Furthermore, it is helpful to compare to alternative analytic continuation techniques.

We do want to stress at this point that concerning checking the validity of our analytic continuations we are in a very favourable spot. Namely, using our impurity solver one is also able to run DMFT directly on the real axis. The discussion of the real axis algorithm is left to Martin Grundner's PhD Thesis [83] as its testing and implementation was mainly his work. However, using said implementation allows us to compare our analytic continuations to data computed directly on the real frequency axis, allowing for direct assessment of the quality of the continued data.

We want to use this section to share some experience we gained when using said algorithms in particular the TRIQS [99] implementation of the maximum entropy method (maxent) [107].

### 4.6.1 Continuation of Green's functions

The continuation of an imaginary frequency Green's function  $G(i\omega_n)$  using maxent amounts to minimizing the functional

$$Q_\alpha[A] = \frac{1}{2}\chi^2[A] - \alpha S[A] \quad (4.95)$$

with

$$\chi^2[A] = \sum_i \frac{1}{\sigma_i^2} \left[ G(\tau_i) - \int d\omega \frac{e^{-\tau_i\omega}}{1 + e^{-\omega\beta}} A(\omega) \right]^2 \quad (4.96)$$

$$S[A] = \int d\omega \left[ A(\omega) - D(\omega) - A(\omega) \log \frac{A(\omega)}{D(\omega)} \right] \quad (4.97)$$

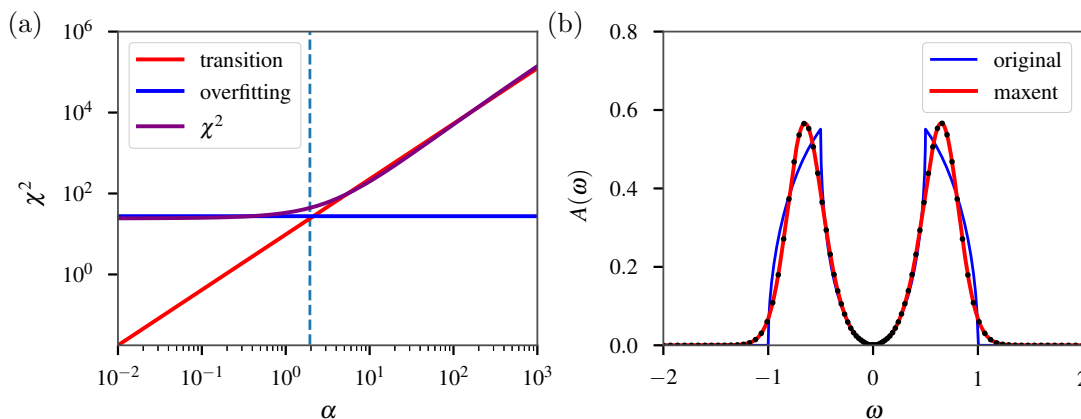


Figure 4.5: (a)  $\chi^2$  for multiple values of  $\alpha$  together with the line fits onto the overfitting and transition regions of  $\alpha$ . The dashed line shows the value for  $\alpha$  that is picked as optimal by the line fit analyser. (b) The exact spectral function (blue) together with the analytic continuation obtained by maxent (red). The black dots are the points on which  $A(\omega)$  is optimized, while the red lines are a spline interpolation by third order polynomials. This example is up to a few changed parameters the same as in the TRIQS/maxent documentation [107].

where  $D(\omega)$  is the so called *default model* that encodes prior knowledge about the form of the spectral function,  $G(\tau_i)$  is the Fourier transform of  $G(i\omega_n)$  at discrete times  $\tau_i$ ,  $\sigma_i$  is the error of  $G(\tau_i)$ ,  $\beta$  is the inverse temperature and  $\alpha$  is a parameter that has to be determined. In practice, all those integrals are discretized, for  $\beta$  we use our auxiliary inverse temperature  $\beta_{\text{aux}}$  with which we discretized our frequency grid  $i\omega_n$  (cf. Sec. 4.1) and we use a flat default model  $D(\omega)$  representing no previous knowledge.

The functional  $Q_\alpha$  is minimized over a range of values for  $\alpha$  and successively the behaviour of  $\chi^2$  with  $\alpha$  is used to determine which  $\alpha$  yields the most faithful result. For large values of  $\alpha$  entropy maximization is largely favoured, leading to results similar to  $D(\omega)$ , while at small values of  $\alpha$  one only tries to optimize  $\chi^2$ , which leads to overfitting as the features in  $G(\tau)$  are strongly suppressed. Therefore, the optimal  $\alpha$  lies somewhere in the middle.

TRIQS comes with a variety of different analysers, that attempt to find the optimal  $\alpha$ . When performing analytic continuations we used the *line fit analyser*. In Fig. 4.5(a) we show the typical behaviour of  $\chi^2$  with  $\alpha$ , together with two lines fit onto  $\chi^2$  in certain regions of  $\alpha$  on a double logarithmic scale. The blue line is fit onto the low  $\alpha$

regime, where  $\chi^2$  becomes essentially constant (i.e. where the overfitting happens), while the red line is fit into the transition between noise fitting and overfitting. The  $\alpha$  at the crossing of the red and blue line is picked as the optimal  $\alpha$ , for which the result of the optimization is then the output of maxent. The choice of alpha range is essential for this to work. We need to choose values of  $\alpha$ , such that the overfitting regime is reached, but the noise fitting is not within the range, as otherwise the line fit will not only fit the transition but also parts of the noise fitting regime. As the fit is in logarithmic scale we tend to use a logarithmic spacing in  $\alpha$ . In panel (b) we show the exact spectral function that we obtained analytically together with the result for the optimal value of  $\alpha$ . As the evaluation of the cost function in the end depends on the number of frequency points one does usually not want to discretize in a too fine way, which is why the rest of the frequency range has to be obtained by interpolation. We typically use around 500 frequency points for our maxent runs. In practice it makes sense to test out if the result improves with more points, though in the cases we tested above 500 there usually was not a significant improvement to be observed. TRIQS also allows for different frequency spacings. We used the hyperbolic grid, when working on BaOsO<sub>3</sub> and the linear grid in the context of t-CuO, as the latter is an insulator and therefore there are no features close to the Fermi level.

In case the quantity of interest is not only the spectral function, but the entire Green's function one can make use of Kramer's Kronig relations [102]

$$G(\omega + i\eta) = \int_{\mathbb{R}} d\omega' \frac{A(\omega')}{\omega' - \omega - i\eta}. \quad (4.98)$$

This way we can simply discretize  $A(\omega)$  very finely and choose some small but finite  $\eta$  to obtain back the full Green's function  $G(\omega)$ .

### 4.6.2 Continuation of self-energies

In many situations it is actually more useful to compute the analytic continuation of self-energies rather than Green's functions. Not only can the local Green's function within the typical approximations of DMFT be computed from the impurity self-energy (cf. Sec. 2.2), but also the momentum resolved Green's function can be obtained directly from the self-energy

$$G(k, \omega + i\eta)_{\alpha\nu} = [(\mathbb{1}(\omega + i\eta) - H(k) - \Sigma(\omega + i\eta))^{-1}]_{\alpha\nu}. \quad (4.99)$$

where  $\alpha, \nu$  are orbital indices,  $H(k)$  is the single particle Hamiltonian in momentum space,  $\eta$  is some broadening and  $\Sigma$  is the self-energy.

This means that when computing momentum resolved spectral functions one would either have to do an analytic continuation for every  $k$ -point of interest, a task that is not really feasible as analytic continuation depends strongly on the parameters, or one can simply perform a single analytic continuation on the self-energy. The benefit of the latter is immediately clear.

The imaginary part of the self-energy  $-\frac{1}{\pi}\text{Im}\Sigma(\omega)$  does not have to decay like  $1/\omega^2$ , which is why it is not a valid spectral function and therefore needs special care before we can apply the maxent procedure introduced above. We can resolve this issue in one of two possible ways. The direct route would be to fit the high frequency tail of  $\Sigma(i\omega_n)$  and subtract the constant and the first order moment, that then have to be treated analytically, similar to Sec. 4.5.1. The remaining part of  $\Sigma$  behaves like a spectral function and can therefore be continued. On the other hand we can use the inversion method [106, 108], that is we define an auxiliary Green's function  $G_{\text{aux}}$  as

$$G_{\text{aux}}(i\omega_n) = [i\omega_n\mathbb{1} - C - \Sigma(i\omega_n)]^{-1}, \quad (4.100)$$

where  $C$  is a constant Hermitian matrix. This approach is very useful in that it does not involve tail fits and one obtains a further parameter  $C$  that can be varied to make the maxent result stable. The auxiliary Green's function  $G_{\text{aux}}(i\omega_n)$  can be continued as described in the last section. Using the resulting  $G_{\text{aux}}(\omega)$  we obtain the self-energy  $\Sigma(\omega)$  by the inverting the above relation (4.100)

$$\Sigma(\omega) = \omega\mathbb{1} - C - G_{\text{aux}}^{-1}(\omega). \quad (4.101)$$

In practice, we usually chose  $C = \lim_{\omega_n \rightarrow \infty} \Sigma(i\omega_n) + \lambda\mathbb{1}$  where  $\lambda$  is a constant we varied until the self-energy seemed stable against minor changes of  $\lambda$ .

### 4.6.3 Continuation of matrix-valued functions

In principle, the maximum entropy method can also be applied on matrix valued functions [106]. However to the current date, the algorithm is not available to public use. The only way to perform maxent on matrix-valued functions that is supported so far is element-wise analytic continuation, which can however not guarantee the positive definiteness of the spectral function. Typical consequences can be seen in Fig. 4.6. The auxiliary Green's function  $G_{\text{aux}}(\omega)$  that is continued loses its positive definiteness and the successive inversion that is needed to obtain the self-energy back leads to unphysical behaviour. Interestingly, using the self-energy from Fig. 4.6 to compute the momentum resolved spectral function (not shown) actually gives qualitative agreement with the one obtained directly on the real axis in the lower

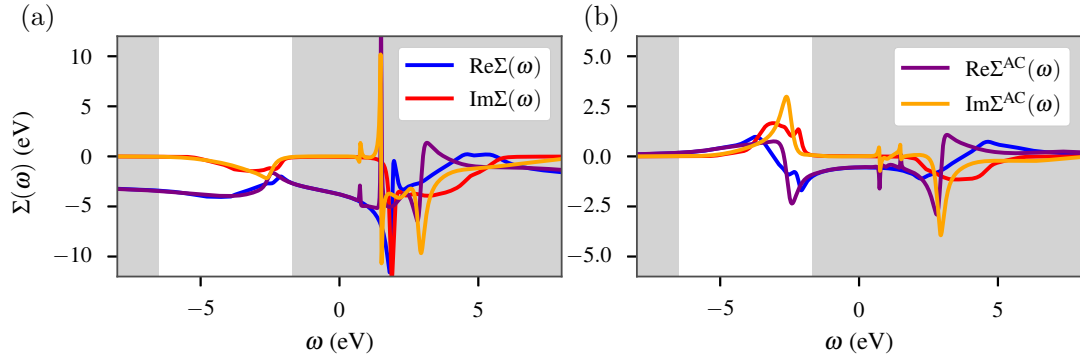


Figure 4.6: Chosen diagonal (a) and offdiagonal (b) element of the self-energy  $\Sigma(\omega)$  for a matrix-valued CDMFT calculation in the context of the t-CuO project (cf. Chap. 6). The blue and red curves show the real and imaginary part of  $\Sigma(\omega)$  as computed with at a broadening  $\eta = 0.05$  eV on the real axis, while the purple and orange curves show the same computed by an analytic continuation from imaginary data using the inversion method. The parameter  $C$  for the inversion method was adjusted such that in the white area the self-energy does not become significantly unphysical, while in the greyed out area it clearly does.

band, while the artefacts only show up in the upper band. This was achieved by choosing  $C = \lim_{\omega_n \rightarrow \infty} \Sigma(i\omega_n) + \lambda \mathbb{1}$  with  $\lambda = -3.5$  eV to shift towards the lower end of the spectrum. The same can also be done for the upper band by shifting  $\lambda$  in the other direction. The exact value does not matter, as the continuation stays rather stable also when changing  $\lambda$  slightly. For the t-CuO project (cf. Chap. 6) from which this data was taken the region of interest is actually the lower band, which makes this approach quite interesting.

In the actual project we did in the end refrain from using analytic continuation as we also had access to the data computed directly on the real axis. In general, we would recommend that, whenever the quantity of interest is only obtainable on the real axis it is best to also compute it there if possible.

## 4.7 A word about interfacing new models

It is likely that future users of the impurity solver will want to solve models that have not yet been treated within the context of this thesis. This is why as a wrap up of this chapter we want to explain the steps necessary to introduce new models.

The impurity solver has to be supplied with an initial hybridisation  $\Delta(i\omega_n)$ . This is usually obtained by setting the self-energy  $\Sigma(i\omega_n)$  to be 0 and demanding the non-interacting impurity Green's function to be equal to its counterpart on the lattice system  $G_0^{\text{loc}}(i\omega_n)$ . We then obtain:

$$\Delta_0(i\omega_n) = \mathbb{1}(i\omega_n + \mu) - \xi - G_0^{\text{loc}}(i\omega_n)^{-1} \quad (4.102)$$

where  $\xi$  denotes the local terms of the non-interacting Hamiltonian and  $\mu$  is the chemical potential. Thus the user needs to provide a way to compute  $G_0^{\text{loc}}(i\omega_n)$ . Furthermore a way to close the self-consistency loop is needed, but this can usually be done in a very similar fashion as

$$G_0^{\text{loc}}(i\omega_n) = \frac{1}{(2\pi)^d} \int_{\text{BZ}} dk [\mathbb{1}(i\omega_n + \mu) - H(k)]^{-1} \quad (4.103)$$

$$G^{\text{loc}}(i\omega_n) = \frac{1}{(2\pi)^d} \int_{\text{BZ}} dk [\mathbb{1}(i\omega_n + \mu) - H(k) - \Sigma(i\omega_n)]^{-1}. \quad (4.104)$$

where  $\Sigma(i\omega_n)$  is the impurity self-energy, which is equal to the lattice self-energy within the DMFT approximations (cf. Sec. 2.2). Thus once one has provided a way to compute  $G_0^{\text{loc}}(i\omega_n)$ ,  $G^{\text{loc}}(i\omega_n)$  can simply be computed by putting  $i\omega_n \mathbb{1} \rightarrow i\omega_n \mathbb{1} - \Sigma(i\omega_n)$ . The same is true for the update of  $\Delta(i\omega_n)$ :

$$\Delta(i\omega_n) = \mathbb{1}(i\omega_n + \mu) - \xi - G^{\text{loc}}(i\omega_n)^{-1} - \Sigma(i\omega_n). \quad (4.105)$$

The models implemented so far are one band 2D lattice models with arbitrary hopping parameters for both DMFT, CDMFT and DCA<sup>1</sup>, a bethe lattice model for DMFT and a TRIQS interface for real materials calculations. The latter is rather general and does only need an input file that can be generated from Wannier90 [109]. For more details on the TRIQS DFT + DMFT interface please consult the documentation on their webpage [98, 110].

In case the interaction Hamiltonian and the symmetries of the problem are already implemented there is nothing left to do. However, let's assume that we want to compute a model that uses an interaction that was not used before. In that case we need to add an option to the parameter specifying the interaction. So far we support Hubbard, Hubbard-Kanamori and density-density-only Hubbard-Kanamori interactions. Further we need to add the interaction tensor  $V_{ijkl}$  to the setup of the MPS

---

<sup>1</sup>DCA was not introduced in depth in this work, as we did not use it in any project. For an introduction we refer the reader to Nils-Oliver Linden's PhD thesis [82]

lattice in the OTIS module `lat.init_TV`. The interaction tensor has to be provided in a way that the contraction is supposed to be normal ordered

$$H_{\text{int}} = \sum_{ijkl} V_{ijkl} c_i^\dagger c_j^\dagger c_k c_l, \quad (4.106)$$

where the indices  $i, j, k, l$  are running over orbitals and spins on the impurity. Assume our model does also have a symmetry that was not used within the impurity solver before. This would mean we have to implement a new symmetry within SYTEN. The way to achieve this is well documented on the SYTEN webpage [80] as well as Claudius Hubig's PhD thesis [81]. After the symmetry has been implemented on the tensor network level we need to tell the impurity solver to create a lattice with said symmetry in the module `lat.lat.gen` as well as in which order the sectors with different quantum numbers have to be searched. The latter can be done in the module `dmrg.sector.managment`. Also in case we do not specify that the model is diagonal in all dynamic quantities we will have to define a new block structure corresponding to this symmetry within the bookkeeping framework of OTIS. If we further know that some blocks are degenerate for the model in question we should also provide this information to the bookkeeping framework as this can greatly speed up the calculation. The OTIS bookkeeping framework is very self explanatory and examples for existing symmetries can be found in the module `util.init_bookkeeping`. All this might sound complicated at first but it is not only straight forward but please note that what was described in this section is not only the steps necessary to interface a new band structure, but a completely new Hamiltonian with new symmetries.

### 4.7.1 Additional steps for SU(2) symmetries

Also non-abelian symmetries like e.g. the SU(2) spin symmetry can be used within tensor network applications [81, 111]. If one wishes to do so the implementation of the interaction term is however a bit more involved as it needs to be written in an explicitly SU(2) invariant way. In SYTEN the approach is to write the Hamiltonian in terms of dot products of spinors containing single particle operators. While the general concept is introduced in Claudius Hubig's PhD thesis [81], in OTIS we have a framework that attempts to translate the U(1) symmetric formulation of the interaction tensor directly into coefficients for those dot products. Thus the only task left for the user is to supply the U(1) formulation of  $V_{ijkl}$  in a way that it can be parsed into an SU(2) symmetric version. The possible dot products  $p_{ijkl}$  consisting

of two creators and two annihilators are given by:

$$p_{ijkl} = \begin{cases} c_{i\uparrow}^\dagger c_{j\downarrow}^\dagger c_{k\uparrow} c_{l\downarrow} + c_{i\downarrow}^\dagger c_{j\downarrow}^\dagger c_{k\downarrow} c_{l\downarrow} + c_{i\uparrow}^\dagger c_{j\uparrow}^\dagger c_{k\uparrow} c_{l\uparrow} + c_{i\downarrow}^\dagger c_{j\uparrow}^\dagger c_{k\downarrow} c_{l\uparrow} & \Delta S = 0 \\ c_{i\uparrow}^\dagger c_{j\uparrow}^\dagger c_{k\uparrow} c_{l\downarrow} + c_{i\uparrow}^\dagger c_{j\downarrow}^\dagger c_{k\uparrow} c_{l\uparrow} + c_{i\uparrow}^\dagger c_{j\uparrow}^\dagger c_{k\downarrow} c_{l\uparrow} + c_{i\downarrow}^\dagger c_{j\uparrow}^\dagger c_{k\uparrow} c_{l\uparrow} & \Delta S = 1 \\ c_{i\downarrow}^\dagger c_{j\downarrow}^\dagger c_{k\downarrow} c_{l\uparrow} + c_{i\downarrow}^\dagger c_{j\downarrow}^\dagger c_{k\uparrow} c_{l\downarrow} + c_{i\downarrow}^\dagger c_{j\uparrow}^\dagger c_{k\downarrow} c_{l\downarrow} + c_{i\uparrow}^\dagger c_{j\downarrow}^\dagger c_{k\downarrow} c_{l\downarrow} & \Delta S = 1 \\ c_{i\uparrow}^\dagger c_{j\downarrow}^\dagger c_{k\downarrow} c_{l\uparrow} + c_{i\downarrow}^\dagger c_{j\uparrow}^\dagger c_{k\uparrow} c_{l\downarrow} + c_{i\uparrow}^\dagger c_{j\uparrow}^\dagger c_{k\downarrow} c_{l\downarrow} + c_{i\downarrow}^\dagger c_{j\downarrow}^\dagger c_{k\uparrow} c_{l\uparrow} & \Delta S \in \{0, 1, 2\} \end{cases} \quad (4.107)$$

Here the second and the third term explicitly break the  $U(1)$  symmetry and therefore they can not contribute to the Hamiltonian. Thus the rules for  $V_{ijkl}$  are:

$$i \neq j \wedge k \neq l \quad \begin{cases} V_{i\uparrow j\downarrow k\uparrow l\downarrow} = V_{i\downarrow j\downarrow k\downarrow l\downarrow} = V_{i\uparrow j\uparrow k\uparrow l\uparrow} = V_{i\downarrow j\uparrow k\downarrow l\uparrow} \\ V_{i\uparrow j\uparrow k\uparrow l\downarrow} = V_{i\uparrow j\uparrow k\downarrow l\uparrow} = V_{i\uparrow j\downarrow k\uparrow l\uparrow} = V_{i\downarrow j\uparrow k\uparrow l\uparrow} = 0 \\ V_{i\downarrow j\downarrow k\downarrow l\uparrow} = V_{i\downarrow j\downarrow k\uparrow l\downarrow} = V_{i\downarrow j\uparrow k\downarrow l\downarrow} = V_{i\uparrow j\downarrow k\downarrow l\downarrow} = 0 \\ V_{i\uparrow j\downarrow k\downarrow l\uparrow} = V_{i\downarrow j\uparrow k\uparrow l\downarrow} = V_{i\uparrow j\uparrow k\downarrow l\downarrow} = V_{i\downarrow j\downarrow k\uparrow l\uparrow} (= 0) \end{cases} \quad (4.108)$$

$$i \neq j \wedge k = l \quad \begin{cases} V_{i\uparrow j\downarrow k\uparrow l\downarrow} = V_{i\downarrow j\uparrow k\downarrow l\uparrow} \\ V_{i\uparrow j\uparrow k\uparrow l\downarrow} = V_{i\uparrow j\uparrow k\downarrow l\uparrow} = 0 \\ V_{i\downarrow j\downarrow k\downarrow l\uparrow} = V_{i\downarrow j\downarrow k\uparrow l\downarrow} = 0 \\ V_{i\downarrow j\uparrow k\uparrow l\downarrow} = V_{i\uparrow j\downarrow k\downarrow l\uparrow} (= 0) \end{cases} \quad (4.109)$$

$$i = j \wedge k \neq l \quad \begin{cases} V_{i\uparrow j\downarrow k\uparrow l\downarrow} = V_{i\downarrow j\uparrow k\downarrow l\uparrow} \\ V_{i\downarrow j\uparrow k\uparrow l\uparrow} = V_{i\uparrow j\downarrow k\uparrow l\uparrow} = 0 \\ V_{i\uparrow j\downarrow k\downarrow l\downarrow} = V_{i\downarrow j\uparrow k\downarrow l\downarrow} = 0 \\ V_{i\downarrow j\uparrow k\uparrow l\downarrow} = V_{i\uparrow j\downarrow k\downarrow l\uparrow} (= 0) \end{cases} \quad (4.110)$$

$$i = j \wedge k = l \quad \begin{cases} V_{i\uparrow j\downarrow k\uparrow l\downarrow} = V_{i\downarrow j\uparrow k\downarrow l\uparrow} \\ V_{i\downarrow j\uparrow k\uparrow l\downarrow} = V_{i\uparrow j\downarrow k\downarrow l\uparrow} (= 0) \end{cases} \quad (4.111)$$

where we separated the spin indices  $\uparrow, \downarrow$  from the orbital indices  $i, j, k, l$ . When all these rules are followed OTIS can construct the coefficients for the dot products in (4.107) automatically. Even though the last line of (4.107) does also contain the  $\Delta S = 0$  sector we recommend only using dot products in the shape of the first line, which is why in (4.108)-(4.111) we put  $(= 0)$  in brackets. In case it is necessary to also include products of the last lines kind, make sure to check that the  $SU(2)$  Hamiltonian gives the same results as its  $U(1)$  counterpart. The last step necessary is to tell the dot products computed within the module `lat.lat_gen` onto which sectors of the new symmetry they are supposed to project. There are plenty of symmetries already implemented that act as examples. The rule is that when performing a dot

product the result has to be projected into the sector that corresponds to the change the resulting operator should have on quantum numbers. For further details see the documentation of SYTEN [\[80\]](#).

# Chapter 5

## BaOsO<sub>3</sub>: A Hund's metal in the presence of strong spin-orbit coupling

The following results are based on the author's publication [2].

In correlated materials many of the emerging properties originate in the complex interplay of many factors like e.g. Hubbard interaction  $U$ , Hund's coupling  $J_H$ , and band structure details like crystal field splitting [38, 39] and the presence of van-Hove singularities [41] (vHs) close to the Fermi level [17, 18]. Additionally, when atomic numbers become large spin-orbit coupling (SOC) becomes relevant [112–114] yielding a broken U(1) symmetry in the spin sector and introducing a finite polarization between orbitals with different total angular momentum that supports the formation of Mott insulating states [112, 115–118].

A class of materials that has raised a significant amount of interest in recent years are Hund's metals in which the Hund's coupling  $J_H$  leads to stronger mass enhancement, and favours the metallic over the insulating state [18, 119–125]. For the case of the  $t_{2g}$  orbitals being the active shell it can be argued that Hund's coupling reduces the Mott gap when the shell is occupied by either two or four electrons [18]. An important Hund's metal that has extensively been studied both from experiment and theory is Sr<sub>2</sub>RuO<sub>4</sub> [4, 35, 126–146]. Apart from the before mentioned effects of Hund's coupling, it was found that the presence of a vHs close to the Fermi level plays an important role in regard of the surprisingly strong electronic correlation effects, like e.g. the very high mass enhancement in Sr<sub>2</sub>RuO<sub>4</sub> [4, 138, 143, 145]. Including the comparably small SOC ( $\lambda = 0.1$  eV) in the study of Sr<sub>2</sub>RuO<sub>4</sub> [35, 126, 133, 135, 139, 140, 146]

did however not yield any effect on the quasiparticle mass enhancement. Still it had important consequences on the shape of the Fermi surface [126, 132, 135] by splitting otherwise degenerate bands. Further, in accordance with experiment, SOC was found to be enhanced by roughly a factor two as compared to the bare value due to the presence of electronic correlations [35, 133, 139, 140, 146].

This being said, SOC is not very sizeable in 3d and 4d materials, e.g. only roughly 0.1 eV in the case of Sr<sub>2</sub>RuO<sub>4</sub> i.e. about three to four times smaller than  $J_H$ . The question arises if Hund's metal physics can survive SOC of comparable size to  $J_H$  as its polarizing tendency favours an insulating state.

An ideal candidate to investigate this question is BaOsO<sub>3</sub>, a transition metal oxide with 4 electrons in the  $t_{2g}$  shell. BaOsO<sub>3</sub> crystallizes in a cubic perovskite structure and shows metallic behaviour in optical and transport measurements on polycrystalline samples [37, 147]. Specific heat measurements show an enhancement of a factor 2.2 over the bare band value [37], which is an indication of sizeable electronic correlations as it can likely be traced back to a mass enhancement of similar size. This, together with the characteristic Hund's metal filling, points towards BaOsO<sub>3</sub> being a Hund's metal. However, the sizeable SOC of 0.3 eV favours a band insulating state, standing in contrast both with strong *dynamic* correlations and with the metallic behaviour. Furthermore in DFT calculations without the inclusion of SOC it was shown, that BaOsO<sub>3</sub> features a vHs directly at the Fermi level [148], which we can expect to have a strong impact on the effect of electronic correlations.

In this chapter we will first give an introduction to the model Hamiltonian that we studied in the basis of cubic harmonics. We will then discuss the transformation into the total angular momentum ( $J$ ) basis, and why this is the appropriate basis to think in in order to understand the physics of BaOsO<sub>3</sub>. After those introductory sections we will discuss the correlated spectral functions and compare them to DFT results, investigate the influence of the vHs, by varying the strength of SOC and present results at the other possible Hund's metal filling of two electrons. Further, we will analyse how the quasi particle mass enhancement depends on SOC and Hund's coupling, identifying a competition between the two. In the end of this chapter we present a phase diagram we mapped out in the  $U$ - $\lambda$  plane, which puts our findings in context with experiment [37].

## 5.1 Model Hamiltonian

The active orbitals of BaOsO<sub>3</sub> are the 5d orbitals, which are depicted in Fig. 5.1. In the cubic harmonic basis the d orbitals are labelled by  $\{d_{xy}, d_{yz}, d_{xz}, d_{z^2}, d_{x^2-y^2}\}$  and can be further divided into the  $e_g = \{d_{z^2}, d_{x^2-y^2}\}$  and the  $t_{2g} = \{d_{xy}, d_{yz}, d_{xz}\}$

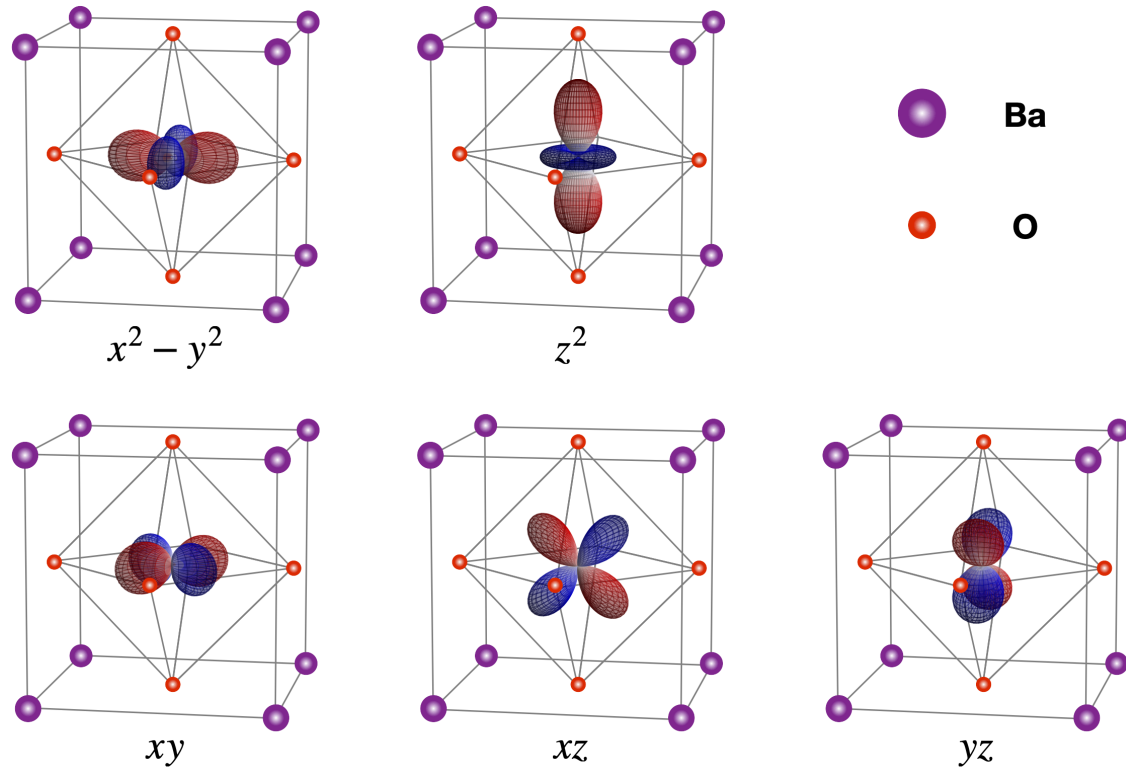


Figure 5.1: Illustration of the d orbitals in the cubic harmonic basis together with a unit cell of  $\text{BaOsO}_3$ . The orbitals are the osmium orbitals, while the other atoms in the unit cell are simply depicted as red (oxygen) and purple (barium) spheres. The upper and lower row show the  $e_g$  and  $t_{2g}$  orbitals respectively.

submanifolds. Due to the presence of the electrons in the p-orbitals of the surrounding oxygen atoms the  $e_g$  orbitals are energetically less favourable than the  $t_{2g}$  ones. The reason for this behaviour can be seen in Fig. 5.1. Namely, when comparing the orientation of the orbitals in the upper row ( $e_g$ ) to those in the lower row ( $t_{2g}$ ) we observe that the  $e_g$  orbitals are pointing directly into the direction of the oxygens, while the  $t_{2g}$  orbitals are pointing between them. It is for this reason that the electrons in the  $e_g$  orbitals feel a stronger repulsion from the electrons within the oxygen orbitals. This lifting of the degeneracy between the d-orbitals is known as crystal field splitting [38, 39]. In fact in  $\text{BaOsO}_3$  the  $t_{2g}$  bands are the only ones crossing the Fermi level, which is why we treat those as correlated orbitals in our DMFT calculations.

We obtained the hopping elements for our tight binding model by fitting maximally

localized Wannier functions [149, 150] to the DFT bands around the Fermi level using the wien2wannier [151] and Wannier90 [109] packages. These fits and the corresponding DFT calculations were performed by our colleague Manuel Zingl.

We include electron-electron interaction on our three active orbitals via a Hubbard-Kanamori-type Hamiltonian [22],

$$\begin{aligned}
H_K = & U \sum_m n_{m\uparrow} n_{m\downarrow} + U' \sum_{m \neq m'} n_{m\uparrow} n_{m'\downarrow} + (U' - J_H) \sum_{m < m'} n_{m\sigma} n_{m'\sigma} + \\
& - J_H \sum_{m \neq m'} d_{m\uparrow}^\dagger d_{m\downarrow} d_{m'\downarrow}^\dagger d_{m'\uparrow} + J_H \sum_{m \neq m'} d_{m\uparrow}^\dagger d_{m\downarrow}^\dagger d_{m'\downarrow} d_{m'\uparrow}.
\end{aligned} \tag{5.1}$$

Here the  $d_{m\sigma}$  ( $d^\dagger$ ) are the annihilation (creation) operators of an electron with spin  $\sigma$  in the orbital  $m \in \{xy, xz, yz\}$  while  $n_{m\sigma}$  measures the occupancy of the latter. The parameters  $U$ ,  $U'$  and  $J_H$  are the intra- and inter-orbital Hubbard interaction and Hund's coupling, respectively. In the  $t_{2g}$  manifold the inter orbital Hubbard interaction is given by  $U' = U - 2J_H$  [18]. For the calculations performed on BaOsO<sub>3</sub> we believe that  $U \sim 2.55$  eV and  $J \sim 0.27$  eV are reasonable parameters as these values were reported in Ref. [152] for NaOsO<sub>3</sub> and LiOsO<sub>3</sub> and similar ones were also found in Ref. [153] for BaOsO<sub>3</sub>. In addition to this parameter set that we consider physical we probe a large range of interaction parameters for  $U$  and the SOC strength  $\lambda$ .

This Hamiltonian can be rephrased by defining the total spin, orbital momentum and particle number operators  $\vec{S}$ ,  $\vec{L}$  and  $N$

$$\vec{S} = \frac{1}{2} \sum_m \sum_{\sigma\sigma'} d_{m\sigma}^\dagger \vec{\tau}_{\sigma\sigma'} d_{m\sigma'} \tag{5.2}$$

$$L_m = i \sum_{m'm''} \sum_{\sigma} \varepsilon_{mm'm''} d_{m'\sigma}^\dagger d_{m''\sigma} \tag{5.3}$$

$$N = \sum_{m\sigma} n_{m\sigma}. \tag{5.4}$$

Here  $\vec{\tau}$  is the vector of Pauli matrices and  $\varepsilon$  is the Levi-Civita tensor. With these definitions in place and using  $U' = U - 2J_H$  the Hamiltonian (5.1) can be written as [18]

$$H_K = (U - 3J_H) \frac{N(N-1)}{2} - 2J_H \vec{S}^2 - \frac{J_H}{2} \vec{L}^2 + \frac{5}{2} JN, \tag{5.5}$$

a form which will prove useful when we discuss the competition of SOC and Hund's coupling. Also from (5.5) we get a direct physical interpretation of what Hund's

coupling  $J_H$  does, namely, it attempts to maximize first the total spin  $\vec{S}^2$  and then the total orbital momentum  $\vec{L}^2$ . The fact that it prioritizes spin can be seen from the prefactor of the two operators  $\vec{S}^2$  and  $\vec{L}^2$ .

The local SOC term which we consider is by definition a single particle term as it couples the orbital momentum of a single electron to its spin. Thus to get its representation in second quantisation we have to evaluate its matrix elements in first quantisation. Denote by  $|d_\alpha, \sigma\rangle$  the  $t_{2g}$  orbitals, then

$$H_{\text{SOC}} = -\lambda \sum_{\alpha\beta\sigma\sigma'} \left\langle d_\alpha, \sigma \left| \sum_i l_i s_i \right| d_\beta, \sigma' \right\rangle d_{\alpha\sigma}^\dagger d_{\beta\sigma'}. \quad (5.6)$$

Here we denoted the SOC strength by  $\lambda$  and the single particle orbital momentum (spin) operator by  $\vec{l}$  ( $\vec{s}$ ). Inserting an identity yields

$$\begin{aligned} H_{\text{SOC}} &= -\lambda \sum_{\alpha\beta\gamma i} \sum_{\sigma\sigma'\sigma''} \langle d_\alpha, \sigma | l_i | d_\gamma, \sigma'' \rangle \langle d_\gamma, \sigma'' | s_i | d_\beta, \sigma' \rangle d_{\alpha\sigma}^\dagger d_{\beta\sigma'} \\ &= -\frac{i\lambda}{2} \sum_{\alpha\beta\gamma i} \sum_{\sigma\sigma'\sigma''} \langle d_\alpha, \sigma | \varepsilon_{i\alpha\gamma} | d_\gamma, \sigma'' \rangle \langle d_\gamma, \sigma'' | \tau_{\sigma'',\sigma'}^i | d_\beta, \sigma' \rangle d_{\alpha\sigma}^\dagger d_{\beta\sigma'} \\ &= -\frac{i\lambda}{2} \sum_{i\alpha\sigma'\sigma\beta} \tau_{\sigma\sigma'}^i \varepsilon_{i\alpha\beta} d_{\alpha\sigma}^\dagger d_{\beta\sigma'}. \end{aligned} \quad (5.7)$$

As we can see in the last expression  $H_{\text{SOC}}$  breaks the U(1) spin symmetry. This would have severe consequences on the computational effort as symmetries speed up MPS calculations significantly. However, there is another U(1) symmetry that can be exploited, when we change the basis of our single particle orbitals.

### 5.1.1 Basis of total angular momentum

Intuitively one might already realise, that we could simply express the SOC term in the basis of total angular momentum  $\vec{j} = \vec{l} + \vec{s}$ , as then

$$\vec{l} \cdot \vec{s} = \frac{1}{2} \left( \vec{j}^2 - \vec{l}^2 - \vec{s}^2 \right), \quad (5.8)$$

which is diagonal in said basis. The problem that arises with this transformation is that we do not have access to the full basis set of the d-orbitals and thus the transformation into the spherical harmonics  $Y_m^l$  with  $l = 2$  can not be done. However, it can be shown, that the  $t_{2g}$  submanifold behaves like an effective  $l = 1$  subspace [40, 82] and we can therefore transform into the spherical harmonics  $Y_m^1$ . From there another

basis transformation can be employed to arrive at the total angular momentum basis set of  $\vec{j} = \vec{l} + \vec{s}$ . In the following we only give the form of  $H_{\text{SOC}}$  in the total angular momentum basis ( $J$ -basis) together with the transformation matrices. For more details the interested reader may resort to Refs. [40, 82].

As the effective orbital momentum has  $l = 1$  and every electron carries spin  $s = \frac{1}{2}$ , the total angular momentum quantum number is going to take the values  $j \in \{\frac{1}{2}, \frac{3}{2}\}$ . Assuming the same convention as in [82] we denote the orbitals with  $j = \frac{3}{2}$  by  $q_m$  and the ones with  $j = \frac{1}{2}$  by  $d_m$  where  $m$  is the projection onto the  $z$ -direction. Ordering the basis as  $\{q_{\frac{3}{2}}, q_{\frac{1}{2}}, q_{-\frac{1}{2}}, q_{-\frac{3}{2}}, d_{\frac{1}{2}}, d_{-\frac{1}{2}}\}$  the Hamiltonian  $H_{\text{SOC}}$  takes the form

$$H_{\text{SOC}}^J = -\lambda \begin{pmatrix} \frac{1}{2} & 0 & 0 & 0 & 0 & 0 \\ 0 & \frac{1}{2} & 0 & 0 & 0 & 0 \\ 0 & 0 & \frac{1}{2} & 0 & 0 & 0 \\ 0 & 0 & 0 & \frac{1}{2} & 0 & 0 \\ 0 & 0 & 0 & 0 & -1 & 0 \\ 0 & 0 & 0 & 0 & 0 & -1 \end{pmatrix}. \quad (5.9)$$

The transformation matrix  $U_J$  that has to be applied to the  $t_{2g}$  orbitals in the basis order  $\{d_{xy\uparrow}, d_{xy\downarrow}, d_{yz\uparrow}, d_{yz\downarrow}, d_{xz\uparrow}, d_{xz\downarrow}\}$  is given by

$$\begin{pmatrix} q_{\frac{3}{2}} \\ q_{\frac{1}{2}} \\ q_{-\frac{1}{2}} \\ q_{-\frac{3}{2}} \\ d_{\frac{1}{2}} \\ d_{-\frac{1}{2}} \end{pmatrix} = \underbrace{\begin{pmatrix} 0 & 0 & \frac{-1}{\sqrt{2}} & 0 & \frac{-i}{\sqrt{2}} & 0 \\ \sqrt{\frac{2}{3}} & 0 & 0 & \frac{-1}{\sqrt{6}} & 0 & \frac{-i}{\sqrt{6}} \\ 0 & \sqrt{\frac{2}{3}} & \frac{1}{\sqrt{6}} & 0 & \frac{-i}{\sqrt{6}} & 0 \\ 0 & 0 & 0 & \frac{1}{\sqrt{2}} & 0 & \frac{-i}{\sqrt{2}} \\ \frac{-1}{\sqrt{3}} & 0 & 0 & \frac{-1}{\sqrt{3}} & 0 & \frac{-i}{\sqrt{3}} \\ 0 & \frac{1}{\sqrt{3}} & \frac{-1}{\sqrt{3}} & 0 & \frac{i}{\sqrt{3}} & 0 \end{pmatrix}}_{U_J} \begin{pmatrix} d_{xy\uparrow} \\ d_{xy\downarrow} \\ d_{yz\uparrow} \\ d_{yz\downarrow} \\ d_{xz\uparrow} \\ d_{xz\downarrow} \end{pmatrix}. \quad (5.10)$$

We observe that in this basis  $H_{\text{SOC}}$  is diagonal. Also  $H_K$  (5.5) does not change total angular momentum, thus so far it seems like all dynamical quantities would be diagonal in this basis. However note that as all the orbitals have to be rotated, the hybridisation  $\Delta(i\omega_n)$  will be rotated as well. In the cubic harmonic basis  $\Delta(i\omega_n)$  is

diagonal so let us write

$$\Delta(i\omega_n) = \begin{pmatrix} a & 0 & 0 & 0 & 0 & 0 \\ 0 & a & 0 & 0 & 0 & 0 \\ 0 & 0 & b & 0 & 0 & 0 \\ 0 & 0 & 0 & b & 0 & 0 \\ 0 & 0 & 0 & 0 & c & 0 \\ 0 & 0 & 0 & 0 & 0 & c \end{pmatrix}, \quad (5.11)$$

with  $a = a(i\omega_n)$ ,  $b = b(i\omega_n)$  and  $c = c(i\omega_n)$ . Rotating this into the  $J$ -basis we obtain

$$\Delta_J(i\omega_n) = \begin{pmatrix} \alpha & 0 & \beta & 0 & 0 & \gamma \\ 0 & \delta & 0 & \beta & \eta & 0 \\ \beta & 0 & \delta & 0 & 0 & -\eta \\ 0 & \beta & 0 & \alpha & -\gamma & 0 \\ 0 & \eta & 0 & -\gamma & \xi & 0 \\ \gamma & 0 & -\eta & 0 & 0 & \xi \end{pmatrix} \quad (5.12)$$

where we defined the following functions

$$\alpha = \frac{b+c}{2}, \quad \beta = \frac{c-b}{2\sqrt{3}}, \quad \gamma = \frac{b-c}{\sqrt{6}}, \quad \delta = \frac{2}{3}a + \frac{b+c}{6}$$

$$\eta = \frac{\frac{1}{\sqrt{2}}(b+c) - \sqrt{2}a}{3}, \quad \xi = \frac{a+b+c}{3}.$$

At first glance this might seem problematic, as the terms  $\beta$  and  $\gamma$  are now again breaking the newly found  $U(1)$  symmetry. Taking a close look at the expressions for those terms though we find, that if the hybridisation is the same for the  $d_{yz}$  and the  $d_{xz}$  orbital, then this largely simplifies

$$\Delta_J(i\omega_n) = \begin{pmatrix} \alpha & 0 & 0 & 0 & 0 & 0 \\ 0 & \delta & 0 & 0 & \eta & 0 \\ 0 & 0 & \delta & 0 & 0 & -\eta \\ 0 & 0 & 0 & \alpha & 0 & 0 \\ 0 & \eta & 0 & 0 & \xi & 0 \\ 0 & 0 & -\eta & 0 & 0 & \xi \end{pmatrix}. \quad (5.13)$$

Typically this is the case for tetragonal unit cells as there the  $d_{xz}$  and  $d_{yz}$  orbitals are degenerate. This degeneracy can be understood by imagining the orbitals in Fig. 5.1 in a unit cell that is elongated along the  $z$ -direction. From the above we

can now extract a block structure  $S_1 = \{q_{\frac{3}{2}}\}$ ,  $S_2 = \{q_{-\frac{3}{2}}\}$ ,  $S_3 = \{q_{\frac{1}{2}}, d_{\frac{1}{2}}\}$ ,  $S_4 = \{q_{-\frac{1}{2}}, d_{-\frac{1}{2}}\}$ , which corresponds to the conservation of the  $z$ -projection of the total angular momentum  $\vec{j}$ . Defining  $\tilde{\Delta}(i\omega_n) = \Delta_J(i\omega_n) + H_{\text{SOC}}^J$  and reading off the blocks yields:

$$\tilde{\Delta}^{1,2}(i\omega_n) = \alpha - \frac{\lambda}{2}, \quad \tilde{\Delta}^{3,4}(i\omega_n) = \begin{pmatrix} \delta - \frac{\lambda}{2} & \pm\eta \\ \pm\eta & \xi + \lambda \end{pmatrix}, \quad (5.14)$$

which means that the 1x1 blocks are degenerate and the 2x2 blocks are degenerate up to a rotation with  $\sigma_z$ . One can numerically check, that neither  $H_K$  nor any other part of the impurity Hamiltonian changes when rotating the orbitals in  $S_4$  by  $\sigma_z$ . Further one can check that switching the orbital in  $S_1$  with the one in  $S_2$ , or switching the orbitals in  $S_3$  and  $\sigma_z \cdot S_4$  leaves  $H_K$  and all other terms invariant. Therefore the blocks  $\{S_1, S_2\}$  and  $\{S_3, \sigma_z \cdot S_4\}$  are degenerate and can be treated as described in Sec. 4.3.1 yielding a speed up of factor 2 as only half the blocks of the Green's function have to be computed.

In the case of BaOsO<sub>3</sub> the unit cell is even cubic, making the hybridisations equal for  $d_{xy}$ ,  $d_{yz}$  and  $d_{xz}$ , due to symmetry (see Fig. 5.1). This yields an hybridisation proportional to the identity with which we obtain six 1x1 blocks where every orbital with equal  $j$  is degenerate

$$\tilde{\Delta}^{1,2,3,4}(i\omega_n) = a - \frac{\lambda}{2}, \quad \tilde{\Delta}^{5,6}(i\omega_n) = a + \lambda. \quad (5.15)$$

Exploiting this further reduces the computation time by one third. Note that currently the symmetry responsible for this additional factorization is not implemented. The latter is only present in this case, as the hybridisation does no longer feature terms, that can change  $j$ . Not having this additional symmetry implemented had no negative influence on the convergence of the DMFT loop.

The fact that all the dynamical quantities are diagonal in the  $J$ -basis is why it is most natural to discuss the physics of BaOsO<sub>3</sub> in this basis. Before moving on to discuss the physics of BaOsO<sub>3</sub> we briefly want to give an overview of the impurity solver parameters that were used for the calculations.

### 5.1.2 Computational details

We perform DMFT calculations for this model with and without Hund's coupling as well as with and without SOC. Without the inclusion of SOC the Hamiltonian is SU(2) symmetric and we are able to use five quantum numbers for the calculation: the occupation number parity of each orbital, the total particle number and the

spin. As was detailed in this section, upon inclusion of SOC we perform calculations in the total angular momentum basis and use only the total particle number and the total angular momentum as quantum numbers. In the case of  $J_H = 0$  we gain further symmetries namely the conservation of the particle number in each orbital (in the  $J$ -basis). For the DMFT calculations presented in this chapter we use at least  $L_b = 6$  bath sites per spin and orbital yielding a total of  $L_{\text{tot}} = 21$  for calculations with  $SU(2)$  symmetry and  $L_{\text{tot}} = 42$  without. We perform time evolutions until a final time of  $\tau = 100 \text{ eV}^{-1}$  in steps of  $\Delta\tau = 0.05 \text{ eV}^{-1}$ .

Now that we have these technical details out of the way we can turn towards the result obtained for  $\text{BaOsO}_3$  starting with the discussion of its spectral function in the next section.

## 5.2 Spectral functions

The starting point of our investigation is the band structure obtained by DFT using the Wien2k [154] toolkit. All DFT calculations were performed by Manuel Zingl.

In Fig. 5.2 we present the band structure of  $\text{BaOsO}_3$  and its density of states (DOS) as obtained by DFT. Note that in both panels (a,b) the active orbitals are the only ones crossing the Fermi surface and are clearly separated from the surrounding orbitals, which we therefore approximate as either full or empty. The DOS has multiple contributing orbitals. As shown in panels (c,d) the main contribution arises from the Os- $t_{2g}$  orbitals, while there is also a large contribution from oxygen. The Os- $t_{2g}$  orbitals hybridize with the oxygen p-orbitals to the effective ones that we describe via the localized Wannier orbitals. A very prominent feature which is present in the absence of SOC is the vHs directly at the Fermi level (c), that can be traced back to the flat bands present in panel (a). However, upon inclusion of SOC the vHs gets split into two parts above and below the Fermi level (d). In  $\text{Sr}_2\text{RuO}_4$  the large mass enhancement, a trademark of strong electron-electron correlations, was partially traced back to the presence of a vHs close to the Fermi level [4, 138, 143, 145]. We therefore expect that in  $\text{BaOsO}_3$  SOC will yield a reduction in mass enhancement, as it leads to a splitting of the vHs, reducing the weight of the DOS around the Fermi level. The careful reader might have recognized that in panels (c,d) there is a slight discrepancy between the Wannier fit and the bands obtained from DFT. This discrepancy is due to the fact, that in the DFT calculation potential momentum dependent SOC terms were taken into account, while on the Wannier model we just added a local SOC term. The reason for this decision is that we wanted to vary the SOC strength over a large range of parameters without having to perform new DFT calculations for each parameter set. Apart from these slight discrepancies however

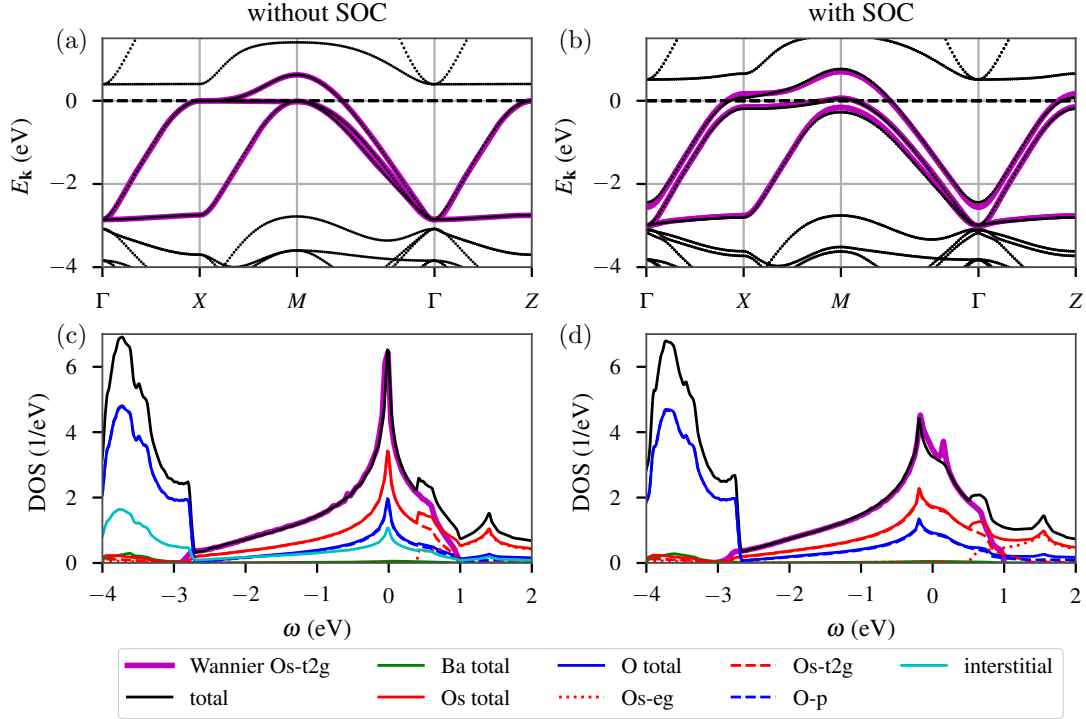


Figure 5.2: Band structure (top row) and density of states (bottom row) as obtained by DFT together with a Wannier fit (purple) of the active orbitals. Panels (a) and (b) show the band structure with and without the inclusion of SOC along a high symmetry path through the Brillouin zone. The lower row shows the density of states (DOS) with (c) and without (d) the inclusion of SOC.

we believe that our Wannier fit describes the low energetic bands of BaOsO<sub>3</sub> to very high accuracy.

In Fig. 5.3 we present the spectral function of BaOsO<sub>3</sub> obtained by DMFT upon inclusion of electron-electron interactions. The calculations were performed using the parameter set we consider physical ( $U = 2.55$  eV,  $J_H = 0.27$  eV,  $\lambda = 0.3$  eV) without (a,b) and with (c,d) the inclusion of SOC respectively. We observe that BaOsO<sub>3</sub> is a moderately correlated metal with strongly renormalized quasiparticle bands at low energies, and substantially incoherent states at higher energies. Without the inclusion of SOC we still find the vHs at the Fermi level (b) and its splitting with SOC (d) is relatively unaffected by electronic correlations.

The inverse quasi particle renormalization  $Z^{-1}$  can be computed from the self-energy

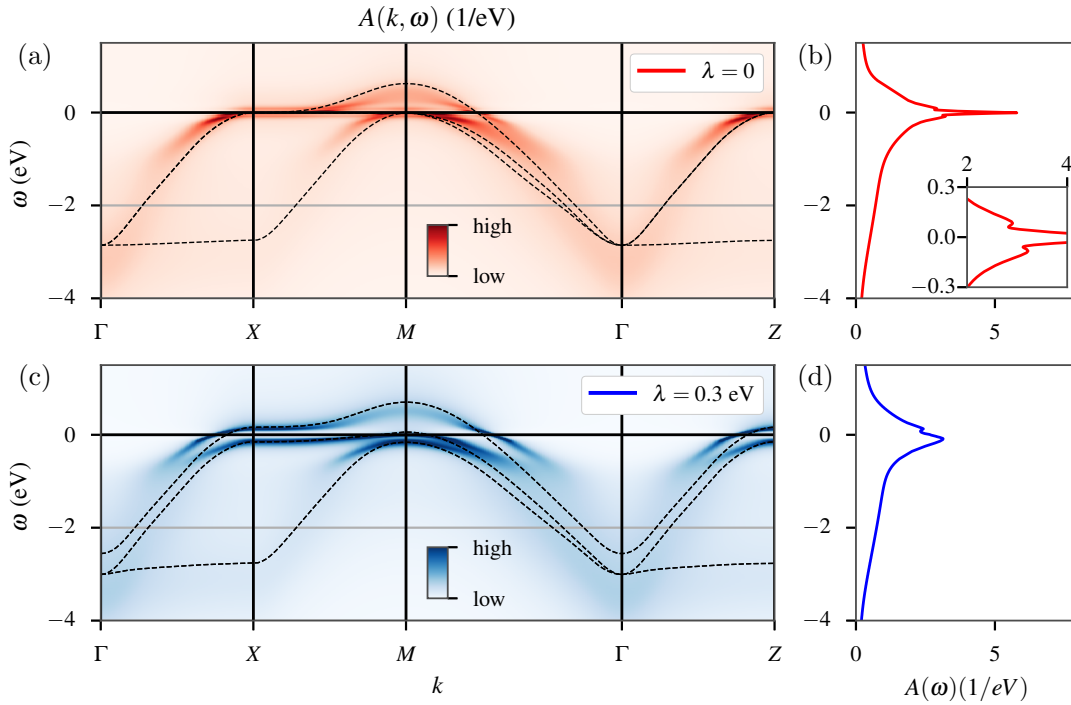


Figure 5.3: Momentum resolved (a,c) and local (b,d) correlated spectral functions for the physical parameter set  $U = 2.55$  eV,  $J_H = 0.27$  eV without (top row) and with SOC  $\lambda = 0.3$  eV (bottom row). The momentum resolved spectral function (a,c) is depicted along a high symmetry path in the Brillouin zone. The inset in (b) shows a zoom onto the two side peaks found in the local spectral function when not including SOC.

as

$$Z^{-1} = 1 - \lim_{\omega_n \rightarrow 0} \frac{\partial \text{Im}\Sigma(i\omega_n)}{\partial \omega_n} \quad (5.16)$$

and is within the local self-energy approximation (c.f. Sec. 2.1.2) equivalent to the quasi particle mass enhancement  $m^*/m$ . The calculated mass enhancement of 2.3 upon the inclusion of SOC is in excellent agreement with the specific heat enhancement of 2.2 measured in experiment [37]. This good agreement with experiments indicates that our choice of interaction parameters for BaOsO<sub>3</sub> is meaningful. We find that the overall band width of the correlated spectral function is roughly comparable to the one of the non-interacting model.

Interestingly in Fig. 5.3 (b) we find two side peaks located roughly at  $\pm 0.1$  eV. These peaks are not present in the non-interacting DOS (c.f. Fig. 5.2 (c)). Similar side peaks were previously observed in both model [124, 125, 155, 156] and real materials calculations [4, 131, 145, 157] and their emergence has been identified as a characteristic feature of Hund's metals. However contrary to the case of BaOsO<sub>3</sub> the side peak was usually only observed on either the occupied side of the spectrum for systems with more than half-filled shells or the unoccupied side in case of less than half-filled shells, but never on both sides as in Fig. 5.3 (b). We could not recover those peaks when ignoring Hund's coupling ( $J_H = 0$ ) nor when including Hund's coupling but considering a semi-circular DOS (spectral functions not shown), which is why we attribute the emergence of those side peaks to both the presence of the vHs in close vicinity to the Fermi level and the inclusion of Hund's coupling. This interpretation is also inline with the fact that no such side peaks are present in the spectral function for the system with SOC (c.f. Fig. 5.3) as SOC splits the vHs away from the Fermi level. Note that the two peaks found in the calculation with SOC are already present without the inclusion of electronic correlations (Fig. 5.2 (d)). We believe that the reason for the emergence of the side peaks on both sides of the spectrum is due to the highly symmetric DOS of BaOsO<sub>3</sub> in the range from  $-0.5$  eV to  $0.5$  eV. However, at the current point this is just speculation and we recommend that these peaks should be investigated in more detail in future studies.

We want to stress at this point that even though SOC is not sufficiently strong to drive the system into a band insulating state the mass enhancement gets reduced from  $Z^{-1} = 3.3$  without SOC to  $Z^{-1} = 2.3$  when including SOC. One characteristic of Hund's metals is that the finite  $J_H$  leads to large mass enhancement. However as discussed before, the presence of the vHs at the Fermi level is also a factor favouring strong correlations. Thus the question arises if the reduction of mass enhancement can be traced back to SOC splitting the vHs, thereby removing it from the Fermi level. This will be investigated in the following section.

### 5.3 Influence of the van-Hove singularity

We start by investigating the influence the splitting of the vHs has on electronic correlations. To this aim we perform a numerical experiment which we present in Fig. 5.4. Namely we shift the non-interacting DOS, such that the shell is occupied by only 2 electrons. This removes the vHs from the Fermi level as can be seen in Fig. 5.4 (b). Note that due to the particle-hole symmetry of the Hubbard-Kanamori Hamiltonian [22] this means that the influence of electronic correlations should not change. SOC on the other hand is not particle-hole symmetric, thus in order to obtain

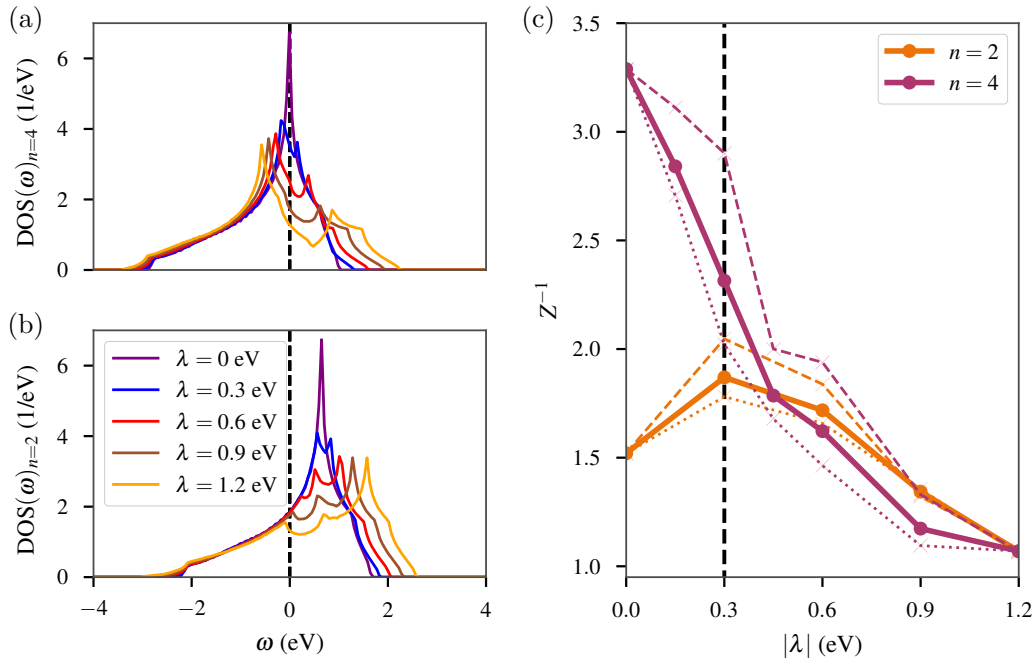


Figure 5.4: Non-interacting DOS for  $n = 4$  (a) and  $n = 2$  (b) electrons in the active orbitals at different values of SOC strength  $\lambda$ . Note that the sign of SOC was inverted for the  $n = 2$  case to also favour the band insulating state at large  $\lambda$ . The dashed black line indicates the Fermi level. Panel (c) depicts the inverse quasi particle renormalization at varying SOC strength  $\lambda$ . The dotted and dashed line correspond to the mass enhancement of the  $j = 3/2$  and  $j = 1/2$  bands respectively, while the solid line depicts the diagonal elements of the mass enhancement in the cubic harmonic basis set. The black dashed line in panel (c) indicates the physical value of the SOC strength  $\lambda$ .

the same large SOC strength limit we reverse its sign for this experiment favouring the two  $j = 1/2$  orbitals over the four  $j = 3/2$  orbitals that would otherwise be preferred. In Fig. 5.4 we show how the non-interacting DOS in the original model (a) and the numerical experiment (b) depend on the SOC strength  $\lambda$ . As expected in the original model the DOS at the Fermi level is strongly decreasing as SOC increases. In the two electron case (b) we still observe a splitting of the vHs but contrary to the four electron case (a) the dependency of the DOS around the Fermi level on

SOC is much weaker. Computing the quasi particle renormalization for both cases reveals an intriguing behaviour (c), namely starting from  $\lambda = 0$  we observe that the renormalization is much stronger for the original four electron system than for the two electron case, which is likely due to the removal of the vHs from the Fermi level. Furthermore, when increasing  $\lambda$  the mass enhancement  $Z^{-1}$  in the four electron case shows a very steep decrease, while in the  $n = 2$  case the dependency seems to be much weaker. This is again completely in line with the behaviour of the DOS around the Fermi level in Fig. 5.4 (a,b). At large SOC strength  $\lambda$  both models approach  $Z^{-1} = 1$  which is reasonable as we setup our numerical experiment such that it also favours the band insulator in this limit, and a band insulator is at its core a single particle phenomenon. We also see that the  $j = 1/2$  bands are always stronger correlated than the  $j = 3/2$  bands. We think that this is due to the  $j = 3/2$  orbitals being four fold degenerate while the  $j = 1/2$  orbitals are only two fold degenerate, yielding a larger active space for the latter. The careful reader may have recognized that in Fig. 5.4 (c) actually the mass enhancement of the  $n = 2$  case is initially increasing (from  $\lambda = 0$  to  $\lambda = 0.3\text{eV}$ ), even though the DOS around the Fermi level is not changing significantly (b). We believe that this is due to both the  $j = 1/2$  and the  $j = 3/2$  subspaces crossing the point of integer occupancy around this value of SOC strength. The results presented in this section give clear evidence of how dramatic the impact of band structure effects can be for electronic correlations.

## 5.4 SOC, Hubbard and Hund's physics

In this section we want to get an understanding about the importance of Hund's physics in BaOsO<sub>3</sub>. In order to achieve this we computed the mass enhancements and polarizations  $\Delta n = n_{j=\frac{3}{2}} - n_{j=\frac{1}{2}}$  in between the  $j = 3/2$  and  $j = 1/2$  orbitals for a broad range of Hubbard interaction parameters  $U$ , two values of  $J_H$  as well as a large variety of SOC strengths  $\lambda$ . We present these results in Fig. 5.5. Let's start by discussing our findings without the inclusion of Hund's coupling. In Fig. 5.5 (a) we observe that the mass enhancement seems to depend overall rather weakly on SOC. Furthermore, we find that at higher values of  $U$  it stays essentially constant up to some critical value of SOC strength  $\lambda$ , where it drastically drops to 1. This is best seen in the curve corresponding to  $U = 3.825\text{eV}$ . Similar behaviour was already observed in model calculations on a semi circular DOS [114], however, even upon inclusion of Hund's coupling. This could hint towards Hund's coupling being necessary to make the mass enhancement sensitive to the vHs close to the Fermi level, as here the dependence is rather weak. Turning our attention towards the polarization (Fig. 5.5 (c)) we can see that without the inclusion of Hund's coupling the polariza-

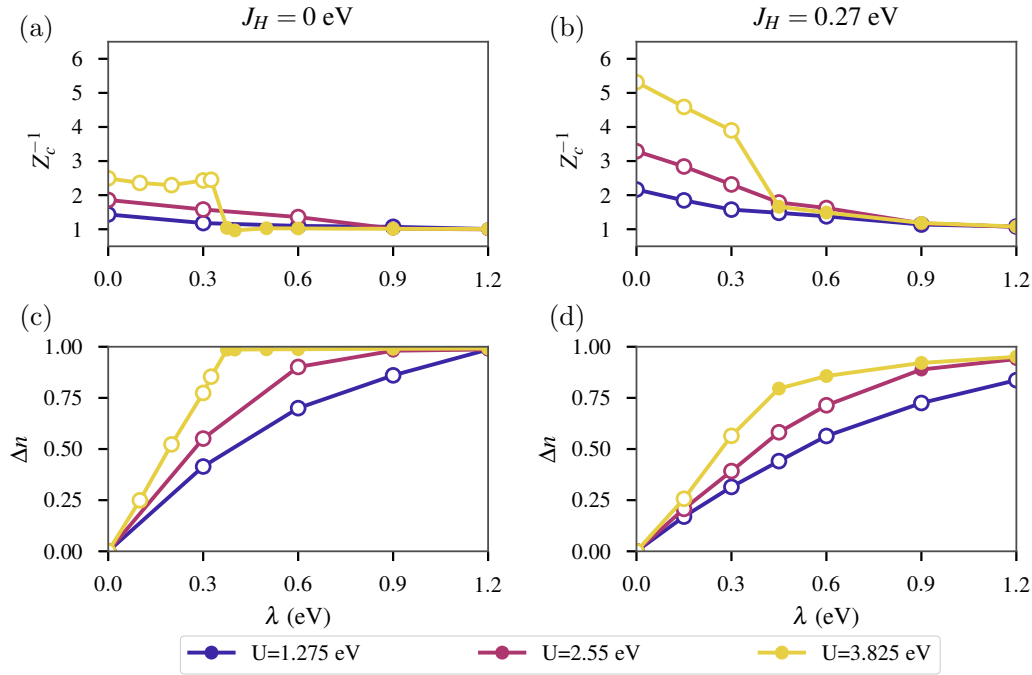


Figure 5.5: (Top row) Diagonal elements of the mass enhancement in the basis of cubic harmonics  $Z_c^{-1}$  for  $J_H = 0$  eV (a) and  $J_H = 0.27$  eV (b) for multiple values of Hubbard interaction  $U$  and SOC strength  $\lambda$ . (Bottom row) Polarizations  $\Delta n = n_{j=3/2} - n_{j=1/2}$  in between the  $j = 3/2$  and  $j = 1/2$  orbitals for  $J_H = 0$  eV (c) and  $J_H = 0.27$  eV for multiple values of  $U$  and  $\lambda$ . In all panels open circles correspond to metallic states, while full circles represent insulators.

tion increases steeply and for all the  $U$  values full occupation of the  $j = 3/2$  orbitals is actually achieved. It is only then when the material becomes insulating. Thus for all the interaction parameters probed without Hund's coupling the only insulating states we found were band insulators. This does however not mean that there can not be any Mott insulators at finite SOC, it just means that to find those one would likely have to go to far larger Hubbard interaction  $U$ .

Upon inclusion of Hund's coupling  $J_H = 0.27$  eV multiple things change. On the one hand the mass enhancement (Fig. 5.5 (b)) drastically increases at low values of SOC strength  $\lambda$ . On the other hand the mass enhancement does now continuously decrease when varying  $\lambda$  and does not just stay constant until a critical value of  $\lambda$ . This again underlines the aforementioned claim that Hund's coupling is the part of

the interaction that is sensitive to the vHs close to the Fermi level. Furthermore, we find that the polarizations (Fig. 5.5 (d)) seem to increase significantly slower than in the case without Hund's coupling. Actually none of the parameter sets probed upon inclusion of Hund's coupling reaches full polarization. Indeed the smoothness of this transition at finite  $J_H$  seems to be a generic feature independent of band structure [114]. This generality hints towards a competition between SOC and Hund's coupling as the latter stops the former from fully filling up the  $j = 3/2$  orbitals.

This competition can actually be explained by an argument in the atomic limit. In the original publication [2] we did not give a derivation. However, here we want to be more elaborate and present the argument in more detail within the next section. Wrapping up this section we conclude that even though the increase of mass enhancement by inclusion of Hund's coupling is less than in 3d/4d Hund's metals [4, 119, 143, 144, 157] it is still a significant increase of about 50% even in the presence of SOC. Furthermore, Hund's coupling has the additional important role of counteracting the polarizing effect of SOC. We can therefore claim that Hund's physics survives even at SOC as strong as  $\lambda = 0.3$  eV and call BaOsO<sub>3</sub> a moderately correlated Hund's metal.

### 5.4.1 The atomic limit

In the last section we observed that there seems to be a competition between Hund's coupling and SOC. Here we present evidence that this competition can be explained by a consideration in the atomic limit.

When the system only consists of a singular atom the Hamiltonian becomes

$$H = H_K + H_{\text{SOC}} \quad (5.17)$$

$$H_K = (U - 3J_H) \frac{N(N-1)}{2} - 2J_H \vec{S}^2 - \frac{J_H}{2} \vec{L}^2 + \frac{5}{2} JN \quad (5.18)$$

$$H_{\text{SOC}} = -\frac{i\lambda}{2} \sum_{i\alpha\sigma'\sigma\beta} \tau_{\sigma\sigma'}^i \varepsilon_{i\alpha\beta} d_{\alpha\sigma}^\dagger d_{\beta\sigma'} \quad (5.19)$$

where the  $d$  ( $d^\dagger$ ) are creation (annihilation) operators in the cubic harmonic basis,  $\vec{S}$ ,  $\vec{L}$  and  $N$  are defined as in Eqs. (5.2) - (5.4). Note that we only have a singular atom and we do already know its overall filling  $N$  to be equal to 4, thus all the terms going with  $N$  are essentially constants in this section. The only other terms  $H_K$  depends on are proportional to  $\vec{S}^2$  and  $\vec{L}^2$ . It would therefore be beneficial to represent our Hilbert space in a basis where those two operators are diagonal, so that we can identify the states that are favoured by  $H_K$ . Currently we represent our

Hilbert space as

$$\mathcal{H} = \mathcal{P}_- \left[ \mathcal{H}_{s=\frac{1}{2}}^{\otimes 4} \otimes \mathcal{H}_c^{\otimes 4} \right], \quad (5.20)$$

where the  $\mathcal{H}_{s=\frac{1}{2}}$  denotes the Hilbert space of the spin (i.e.  $\mathbb{C}^2$ ),  $\mathcal{H}_c$  denotes the Hilbert space spanned by the cubic harmonic basis set and the projector  $\mathcal{P}_-$  projects onto the completely antisymmetric part of the wave function. As we discussed already in Sec. 5.1 the  $t_{2g}$  states can be represented by spherical harmonics corresponding to an effective orbital momentum with  $l = 1$ . Thus the Hilbert space can be written as

$$\mathcal{H} = \mathcal{P}_- \left[ \mathcal{H}_{s=\frac{1}{2}}^{\otimes 4} \otimes \mathcal{H}_{l=1}^{\otimes 4} \right] = \mathcal{P}_- \left[ \left( \bigoplus_{S=0}^2 \mathcal{H}_S \right) \otimes \left( \bigoplus_{L=0}^4 \mathcal{H}_L \right) \right]. \quad (5.21)$$

Here in the second step we performed angular momentum summation in the first and second term respectively to be able to label the Hilbert space by total spin ( $\mathcal{H}_S$ ) and orbital momentum ( $\mathcal{H}_L$ ). Doing so would allow us to identify which of the multiplets is favoured by  $H_K$ . The ultimate goal would be to compute the overlap the state favoured by  $H_{\text{SOC}}$ , namely, the one fully occupying the  $j = 3/2$  states, has with the multiplet. However, performing four angular momentum additions in both the first and the second term would result in a massive calculation as we would have to compute Clebsch-Gordan coefficients (CGC) for every summation successively.

A lot of this effort can be alleviated by performing a particle hole transform, that is we shift from describing the particles occupying the  $t_{2g}$  shell to describing the orbitals who are left empty. We consider the transform

$$d_{\alpha\sigma}^\dagger \rightarrow \eta_\alpha d_{\alpha\sigma} \quad (5.22)$$

with

$$\eta_\alpha = \begin{cases} 1 & \text{if } \alpha \in \{xy, xz\} \\ -1 & \text{if } \alpha \in \{yz\}. \end{cases} \quad (5.23)$$

One can check that under this transformation the terms in the Hamiltonian transform as

$$\vec{S}^2 \rightarrow \vec{S}^2 \quad (5.24)$$

$$\vec{L}^2 \rightarrow \vec{L}^2 \quad (5.25)$$

$$N \rightarrow 6 - N \quad (5.26)$$

$$H_{\text{SOC}} \rightarrow -H_{\text{SOC}}. \quad (5.27)$$

Thus as the particle number on our atom is fixed  $H_K$  stays invariant up to the addition of constants.  $H_{\text{SOC}}$  changes sign and therefore does now favour the full occupation of the  $j = 1/2$  orbitals with holes, which makes perfect sense as this is physically the same as favouring the occupation of the  $j = 3/2$  orbitals with electrons. Our particle hole transformed Hilbert space can now be represented as

$$\mathcal{H}_{\text{ph}} = \mathcal{P}_- \left[ \mathcal{H}_{s=\frac{1}{2}}^{\otimes 2} \otimes \mathcal{H}_{l=1}^{\otimes 2} \right] = \mathcal{P}_- \left[ \left( \bigoplus_{S=0}^1 \mathcal{H}_S \right) \otimes \left( \bigoplus_{L=0}^2 \mathcal{H}_L \right) \right], \quad (5.28)$$

where in the second step we performed an angular momentum addition to again label the subspaces by their total spin  $S$  and orbital momentum  $L$ . It is now interesting to investigate the basis of the subspaces for given  $S$  and  $L$ .

$\mathcal{H}_S$  is spanned by

$$\mathcal{H}_{S=1} = \begin{cases} |1_{S=1}\rangle & = |\uparrow\uparrow\rangle \\ |0_{S=1}\rangle & = \frac{1}{\sqrt{2}} (|\uparrow\downarrow\rangle + |\downarrow\uparrow\rangle) \\ |-1_{S=1}\rangle & = |\downarrow\downarrow\rangle \end{cases} \quad (5.29)$$

$$\mathcal{H}_{S=0} = \left\{ |0_{S=0}\rangle = \frac{1}{\sqrt{2}} (|\uparrow\downarrow\rangle - |\downarrow\uparrow\rangle) \right\} \quad (5.30)$$

where  $|m_S\rangle$  represents the state with total spin  $S$  and projection on the  $z$ -direction  $m$ , while the arrows on the right represent holes with the corresponding spin. The brackets on the right side denote the span over the enclosed states.

$\mathcal{H}_L$  is spanned by

$$\mathcal{H}_{L=2} = \begin{cases} |2_{L=2}\rangle & = |1, 1\rangle \\ |1_{L=2}\rangle & = \frac{1}{\sqrt{2}} (|1, 0\rangle + |0, 1\rangle) \\ |0_{L=2}\rangle & = \frac{1}{\sqrt{6}} (|-1, 1\rangle + |1, -1\rangle + 2|0, 0\rangle) \\ |-1_{L=2}\rangle & = \frac{1}{\sqrt{2}} (|-1, 0\rangle + |0, -1\rangle) \\ |-2_{L=2}\rangle & = |-1, -1\rangle \end{cases} \quad (5.31)$$

$$\mathcal{H}_{L=1} = \begin{cases} |1_{L=1}\rangle & = \frac{1}{\sqrt{2}} (|1, 0\rangle - |0, 1\rangle) \\ |0_{L=1}\rangle & = \frac{1}{\sqrt{2}} (|1, -1\rangle - |-1, 1\rangle) \\ |-1_{L=1}\rangle & = \frac{1}{\sqrt{2}} (|0, -1\rangle - |-1, 0\rangle) \end{cases} \quad (5.32)$$

$$\mathcal{H}_{L=0} = \left\{ |0_{L=0}\rangle = \frac{1}{\sqrt{3}} (|1, -1\rangle + |-1, 1\rangle - |0, 0\rangle) \right\} \quad (5.33)$$

where  $|m_L\rangle$  is the state with total orbital momentum  $L$  and projection of the same onto the  $z$ -axis  $m$ . The states  $|m_1, m_2\rangle$  on the right are the spherical harmonics for

the effective  $l = 1$  in the  $t_{2g}$  manifold where the first (second) hole is in the state with orbital momentum in  $z$ -direction  $m_1$  ( $m_2$ ).

Note that the states in  $\mathcal{H}_{L=2}$ ,  $\mathcal{H}_{L=0}$  and  $\mathcal{H}_{S=1}$  are symmetric under exchanging the holes, while those in  $\mathcal{H}_{L=1}$  and  $\mathcal{H}_{S=0}$  are antisymmetric. This allows us to immediately apply the projection  $\mathcal{P}_-$  and obtain for the particle hole transformed Hilbert space

$$\mathcal{H}_{\text{ph}} = \mathcal{P}_- \left[ \left( \bigoplus_{S=0}^1 \mathcal{H}_S \right) \otimes \left( \bigoplus_{L=0}^2 \mathcal{H}_L \right) \right] \quad (5.34)$$

$$= (\mathcal{H}_{S=1} \otimes \mathcal{H}_{L=1}) \oplus (\mathcal{H}_{S=0} \otimes \mathcal{H}_{L=2}) \oplus (\mathcal{H}_{S=0} \otimes \mathcal{H}_{L=0}) \quad (5.35)$$

In each of these three subspaces  $H_K$  takes a constant value. Their energies are up to the constants stemming from the occupation number  $E_{S=1,L=1} = -\frac{5}{2}J_H$ ,  $E_{S=0,L=2} = -J_H$  and  $E_{S=0,L=0} = 0$  respectively. Therefore,  $H_K$  clearly favours the  $S = 1$ ,  $L = 1$  subspace. For the following argument it is also useful to think about the overall total angular momentum supported by these subspaces respectively. Performing another angular momentum addition in each of the subspaces we obtain

$$\mathcal{H}_{\text{ph}} = \left( \mathcal{H}_{J=2}^{L=1,S=1} \oplus \mathcal{H}_{J=1}^{L=1,S=1} \oplus \mathcal{H}_{J=0}^{L=1,S=1} \right) \oplus \mathcal{H}_{J=2}^{S=0,L=2} \oplus \mathcal{H}_{J=0}^{S=0,L=0}. \quad (5.36)$$

Please note how total angular momentum  $J = 0$  is only supported, when  $S = 1$ ,  $L = 1$  or  $S = 0$ ,  $L = 0$ . As we will show the state with full occupation of the  $j = 1/2$  orbitals has total angular momentum  $J = 0$ , thus it is only possible to not have a competition between  $H_K$  and  $H_{\text{SOC}}$ , when said state is contained in  $\mathcal{H}_{J=0}^{L=1,S=1}$  as this is the subspace that both has  $J = 0$  and is favoured by  $H_K$ . In order to check this we have to identify the state  $H_{\text{SOC}}$  favours in the same basis as we have for  $H_K$ . Therefore, we yet again write the particle-hole transformed Hilbert space in a different manner

$$\mathcal{H}_{\text{ph}} = \mathcal{P}_- \left[ \mathcal{H}_{s=\frac{1}{2}}^{\otimes 2} \otimes \mathcal{H}_{l=1}^{\otimes 2} \right] \quad (5.37)$$

$$= \mathcal{P}_- \left[ \left( \mathcal{H}_{s=\frac{1}{2}} \otimes \mathcal{H}_{l=1} \right) \otimes \left( \mathcal{H}_{s=\frac{1}{2}} \otimes \mathcal{H}_{l=1} \right) \right] \quad (5.38)$$

$$= \mathcal{P}_- \left[ \left( \mathcal{H}_{j=\frac{3}{2}}^{l=1,s=\frac{1}{2}} \oplus \mathcal{H}_{j=\frac{1}{2}}^{l=1,s=\frac{1}{2}} \right) \otimes \left( \mathcal{H}_{j=\frac{3}{2}}^{l=1,s=\frac{1}{2}} \oplus \mathcal{H}_{j=\frac{1}{2}}^{l=1,s=\frac{1}{2}} \right) \right] \quad (5.39)$$

$$= \mathcal{P}_- \left[ \left( \mathcal{H}_{j=\frac{3}{2}} \otimes \mathcal{H}_{j=\frac{3}{2}} \right) \oplus \left( \mathcal{H}_{j=\frac{1}{2}} \otimes \mathcal{H}_{j=\frac{3}{2}} \right) \oplus \left( \mathcal{H}_{j=\frac{3}{2}} \otimes \mathcal{H}_{j=\frac{1}{2}} \right) \right] \\ \oplus \mathcal{P}_- \left[ \mathcal{H}_{j=\frac{1}{2}} \otimes \mathcal{H}_{j=\frac{1}{2}} \right]. \quad (5.40)$$

In (5.39) we performed the angular momentum summation first between each holes orbital momentum and spin. Note that this is equivalent to rotating the single

particle orbitals into the basis of the total angular momentum per particle as we did in Sec. 5.1.1. Then in the last step we suppressed the  $l, s$  labels to not further bloat up the equation. We want to have a first quantized description of the state that describes the full occupation of  $j = 1/2$  orbitals with holes. Therefore, the only subspace we are interested in is

$$\mathcal{H}_{\text{SOC}} = \mathcal{P}_- \left[ \mathcal{H}_{j=\frac{1}{2}} \otimes \mathcal{H}_{j=\frac{1}{2}} \right] = \mathcal{P}_- \left[ \mathcal{H}_{J=1}^{j_1=\frac{1}{2}, j_2=\frac{1}{2}} \oplus \mathcal{H}_{J=0}^{j_1=\frac{1}{2}, j_2=\frac{1}{2}} \right] \quad (5.41)$$

whose subspaces are given by

$$\mathcal{H}_{J=1}^{j_1=\frac{1}{2}, j_2=\frac{1}{2}} = \begin{cases} |1_{J=1}\rangle & = |\frac{1}{2}, \frac{1}{2}\rangle \\ |0_{J=1}\rangle & = \frac{1}{\sqrt{2}} (|\frac{1}{2}, -\frac{1}{2}\rangle + |-\frac{1}{2}, \frac{1}{2}\rangle) \\ |-1_{J=1}\rangle & = |-\frac{1}{2}, -\frac{1}{2}\rangle \end{cases} \quad (5.42)$$

$$\mathcal{H}_{J=0}^{j_1=\frac{1}{2}, j_2=\frac{1}{2}} = \begin{cases} |0_{J=0}\rangle & = \frac{1}{\sqrt{2}} (|\frac{1}{2}, -\frac{1}{2}\rangle - |-\frac{1}{2}, \frac{1}{2}\rangle). \end{cases} \quad (5.43)$$

Here the  $|m_{j_1}, m_{j_2}\rangle$  represent the state with one hole having total angular momentum in  $z$ -direction  $m_{j_1}$  while the other one has  $m_{j_2}$ . As we can immediately see all the states in the  $J = 1$  subspace are symmetric under particle exchange, thus they are projected out by  $\mathcal{P}_-$ . Now we have to write both the state favoured by SOC and the one favoured by  $H_K$  in the basis of spin and the spherical harmonics to be able to compute an overlap. For this we need the basis representation of  $\mathcal{H}_{j=\frac{1}{2}}^{s=\frac{1}{2}, l=1}$  in terms of spherical harmonics

$$\mathcal{H}_{j=\frac{1}{2}}^{s=\frac{1}{2}, l=1} = \begin{cases} |\frac{1}{2}_{j=\frac{1}{2}}\rangle & = \frac{1}{\sqrt{3}} (|\uparrow, 0\rangle - \sqrt{2}|\downarrow, 1\rangle) \\ |-\frac{1}{2}_{j=\frac{1}{2}}\rangle & = \frac{1}{\sqrt{3}} (|\downarrow, 0\rangle - \sqrt{2}|\uparrow, -1\rangle) \end{cases} \quad (5.44)$$

Thus in the original basis the state  $|\text{SOC}\rangle$  favoured by  $H_{\text{SOC}}$  is given by

$$\begin{aligned} |\text{SOC}\rangle = & \frac{1}{3\sqrt{2}} |\uparrow, 0, \downarrow, 0\rangle - \frac{1}{3} |\downarrow, 1, \downarrow, 0\rangle - \frac{1}{3} |\uparrow, 0, \uparrow, -1\rangle \\ & + \frac{\sqrt{2}}{3} |\downarrow, 1, \uparrow, -1\rangle - (1 \leftrightarrow 2), \end{aligned} \quad (5.45)$$

where we denoted by  $|m_{s_1}, m_{l_1}, m_{s_2}, m_{l_2}\rangle$  for a state with two holes, where the  $i$ -th hole has spin  $m_{s_i}$  and orbital momentum  $m_{l_i}$  in  $z$ -direction. For the state favoured by Hund's coupling  $|S = 1, L = 1, J = 0\rangle$  we obtain

$$\begin{aligned} |S = 1, L = 1, J = 0\rangle = & \frac{1}{\sqrt{6}} |\uparrow, 0, \uparrow, -1\rangle + \frac{1}{\sqrt{6}} |\downarrow, 1, \downarrow, 0\rangle - \frac{1}{2\sqrt{3}} |\uparrow, 1, \downarrow, -1\rangle \\ & - \frac{1}{2\sqrt{3}} |\downarrow, 1, \uparrow, -1\rangle - (1 \leftrightarrow 2). \end{aligned} \quad (5.46)$$

With this we can compute their overlap

$$\langle S = 1, L = 1, J = 0 | \text{SOC} \rangle = -\sqrt{\frac{2}{3}} \quad (5.47)$$

which proves, that  $|\text{SOC}\rangle$  is not fully contained in the  $S = 1, L = 1$  multiplet. Since we are already at it, we might as well also compute the overlap with the only other state, that has  $J = 0$ , namely

$$\begin{aligned} |S = 0, L = 0, J = 0\rangle = & \frac{1}{\sqrt{6}} (|\uparrow, 1, \downarrow, -1\rangle - |\uparrow, 0, \downarrow, 0\rangle - |\downarrow, 1, \uparrow, -1\rangle) \\ & - (1 \leftrightarrow 2). \end{aligned} \quad (5.48)$$

Thus we obtain for the overlap

$$\langle S = 0, L = 0, J = 0 | \text{SOC} \rangle = -\sqrt{\frac{1}{3}} \quad (5.49)$$

and with this we can write the  $|\text{SOC}\rangle$  in the basis labelled by  $S, L, J$  as

$$|\text{SOC}\rangle = -\sqrt{\frac{2}{3}} |S = 1, L = 1, J = 0\rangle - \frac{1}{\sqrt{3}} |S = 0, L = 0, J = 0\rangle. \quad (5.50)$$

Note that the state with  $S = 0, L = 0$  and  $J = 0$ , is the state that is the least favourable for Hund's coupling  $J_H$ . Therefore its competition with SOC that was observed in the last section can be understood already at this level even without the inclusion of any band structure effects. Putting it in a very pictorial way, Hund's coupling wants to align the angular momentum and spin of all the electrons, while SOC just wants to align every particles spin with its own orbital momentum. These two orientations are however not simultaneously fulfillable, yielding a competition as long as both  $J_H$  and the SOC strength  $\lambda$  are finite. Please note that the above consideration is only valid for materials in which the  $t_{2g}$  shell hosts four electrons as throughout the section we assumed  $N = 4$ .

## 5.5 Classification of Phases in the $U$ - $\lambda$ -plane

After this very extensive investigation of the competition between Hund's coupling, SOC and also the role of the vHs we now want to place  $\text{BaOsO}_3$  in a paramagnetic phase diagram in the  $U$ - $\lambda$  plane, presented in Fig. 5.6 (a). We find an insulating (squares) and a metallic (circles) phase, which we identified by studying the local

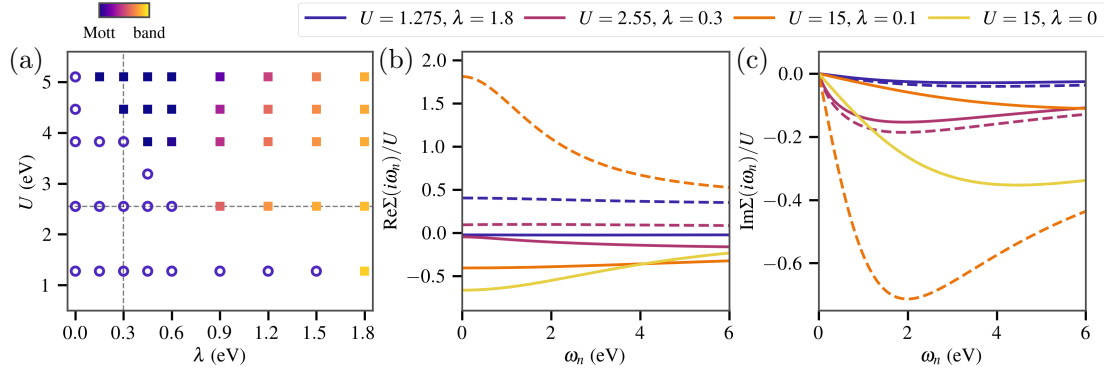


Figure 5.6: Phase diagram in the  $U - \lambda$  plane at constant  $J_H = 0.27$  eV (a). We depict metallic states by open circles and insulating states by squares. As there is no sharp transition but rather a crossover between the Mott and the band insulating state we encode the states character (Mott-like or band-like) in the symbol colours (see main text for details). Real (b) and imaginary (c) part of the self-energy for  $J_H = 0.27$  eV and selected values of  $U$  and  $\lambda$  (in eV). The solid and dashed lines correspond to the  $j = 3/2$  and  $j = 1/2$  bands, respectively. In order to show all self-energies on a comparable scale we shifted the real parts by the chemical potential and rescaled both imaginary and real part by  $1/U$ .

Green's function  $G_{\text{loc}}(i\omega_n)$  in the limit  $\omega_n \rightarrow 0$ . In this limit due to the analyticity of  $G_{\text{loc}}$ , the Green's functions on the real axis and on the imaginary axis coincide. Thus when the spectrum has a gap the imaginary part of  $G_{\text{loc}}$  tends to zero as  $\omega_n \rightarrow 0$ . The first interesting observation that can be made from Fig. 5.6 (a) is that the metallic regime is located on the lower left triangle of the phase diagram, i.e. at small  $U$  and  $\lambda$ . This tells us that Hubbard interaction and SOC work together to stabilize the insulating regime. Indeed this observation can be understood by the polarizing nature of the Hubbard interaction together with the SOC favouring the  $j = 3/2$  orbitals. The latter leads to a polarization that can then be enhanced upon by the electron-electron interaction. As discussed in Sec. 5.2 at physical parameters (dashed lines in Fig. 5.6) BaOsO<sub>3</sub> is metallic, however, it is rather close to the insulating regime. We want to note that our phase diagram is consistent with an unpublished calculation by Dai [158].

Investigating the insulating regime further we find states of two different characters namely Mott and band insulator like states. At high  $U$  and  $\lambda = 0$  we expect a Mott insulating regime, where the insulating nature stems from strong electronic correlation effects, while in the high  $\lambda$  region we find the band insulating phase. The latter,

contrary to the Mott state, is at its core a single particle effect as it stems from the gap induced by separating the  $j = 1/2$  from the  $j = 3/2$  orbitals. When  $U$ ,  $J_H$  and  $\lambda$  are finite the transition between the Mott and the van-Vleck state is continuous as we did already observe in Sec. 5.4 and more specifically Fig. 5.5. Therefore, we decided to introduce a colour coding in the phase diagram (Fig. 5.6 (a)). Namely, we define a measure for electronic calculations  $\chi(U, \lambda) = |\min_{j, \omega_n} \text{Im}\Sigma_j(i\omega_n)|$  where  $\Sigma_j(\omega_n)$  is the self-energy of an orbital with total angular momentum  $j$ .  $\chi$  is a good measure, as in the band insulating case the self-energy should be completely frequency independent, and as it is decaying to 0 as  $\omega_n \rightarrow \infty$  its imaginary part has to be equal to 0 for all  $\omega_n$ . Furthermore  $\text{Im}\Sigma_j(i\omega_n)$  is always smaller than 0, thus taking the minimum actually gives us the largest value it has in magnitude. In the figure the colour scaling is such that for  $\chi > 0.5$  eV the darkest colour is given otherwise its linearly interpolated between 0 and 0.5 eV. In panels (b,c) of Fig. 5.6 we show the real and imaginary parts of self-energies for a few typical values of  $U$  and  $\lambda$  with the goal of illustrating the differences between the insulating states. The case  $U = 1.275$  eV,  $\lambda = 1.8$  eV shows a typical band insulating state with almost constant self-energy, but nevertheless not unimportant correlations, as they lead to a further separation of the  $j = 1/2$  and  $j = 3/2$  state. This is what we call a *static* correlation effect, as it does not depend on frequency. On the other hand we show with  $U = 15$  eV,  $\lambda = 0$  a typical Mott insulating case. Note the strong frequency dependence in both the real and imaginary parts. This is what we like to refer to as *dynamic* correlation effects. With  $U = 15$  eV,  $\lambda = 0.1$  eV we also show a Mott insulator in the presence of small SOC. Even though there is a large static level splitting in the real part, the dynamic effect is even stronger, which can also be seen in the imaginary part. Due to the presence of such strong dynamic correlation effects we still identify this state as a Mott insulator. This is far from trivial as one could have thought that as soon as SOC introduces a slight polarization between the  $j = 1/2$  and  $j = 3/2$  states the Hubbard interaction would enhance this effect so strongly that one immediately arrives in the band insulating limit. However, we find that this is not the case. Note also that the dynamic correlations, best seen in the imaginary part, are always stronger in the  $j = 1/2$  bands. As already explained in Sec. 5.4 this is likely due to the larger active space in those orbitals.

Finally we present also the self-energies which we find for the realistic parameter set ( $U = 2.55$  eV,  $\lambda = 0.3$  eV). We find sizeable dynamic correlation effects, best seen in the imaginary part. Further we observe that in contrast to the Mott insulating case at small SOC ( $U = 15$  eV,  $\lambda = 0.1$  eV) at low frequencies the splitting in the real part is smaller than at high frequencies, which we interpret as the dynamic correlations helping to reduce the gap between the  $j = 1/2$  and  $j = 3/2$  states therefore favouring

the metallic state. This is likely an effect of Hund's coupling as Hubbard interaction at integer fillings does not favour a metallic state [18]. The reason why this effect can not be seen in the other parameter regimes is because in those either  $U$  or  $\lambda$  is dominating the effects of  $J_H$ .

The splitting found in the real part of the self-energy can be interpreted as a correlation-driven enhancement of the SOC as splitting the  $j = 3/2$  from the  $j = 1/2$  bands is in essence exactly what SOC does. However, contrary to the case of Sr<sub>2</sub>RuO<sub>4</sub> [4, 35, 114, 133, 140], where the real parts are almost constant, in BaOsO<sub>3</sub> they are strongly frequency dependent. This makes it difficult to talk about an effective SOC, as SOC is a term in the Hamiltonian and therefore static. As we are describing a low energy model of the problem we define  $\lambda_{\text{eff}} := \lambda + \frac{2}{3}\Delta\text{Re}\Sigma_j(i\omega_n \rightarrow 0)$  as the splitting in the low frequency limit as proposed in Ref. [114]. The splitting between the components of the real part of the self-energy in this limit is about 0.34 eV, which yields  $\lambda_{\text{eff}} \approx 0.53$  eV. This means that, at low frequencies, SOC is effectively enhanced by roughly a factor of 1.8, which is slightly less than the factor of 2 found for Sr<sub>2</sub>RuO<sub>4</sub> and Sr<sub>2</sub>MoO<sub>4</sub> [4, 35, 133, 140]. Upon inspecting Fig. 5.3 (c) one however finds, that the splitting of the bands introduced by SOC does not seem to have significantly increased by including electronic correlations. This can be explained by the fact that the mass of the quasi particles to which those bands correspond does also get renormalized. Including the mass renormalization we obtain an effective splitting of  $\sim Z\lambda_{\text{eff}}$  which in our case is about 0.23 eV. Investigating again Fig. 5.3(c) we find that the splitting at the  $X$  point is of magnitude 0.25 eV, which coincides very well to the splitting we would expect for the quasi-particle bands.

## 5.6 Summary

Within this chapter we investigated the electronic structure and correlation effects in BaOsO<sub>3</sub>. We started by discussing the bandstructure and DOS obtained from DFT and found that in the absence of SOC, there is a vHs located directly at the Fermi surface. This vHs is split upon the inclusion of SOC, which reduces the weight of the DOS around the Fermi level, raising the question whether inclusion of electron-electron interactions via a Hubbard-Kanamori interaction term may already be sufficient to drive the system into a insulating state.

To address this question, we studied the spectral functions upon inclusion of electron-electron interaction computed using DMFT. Our findings are that the SOC of about 0.3 eV is not sufficient to drive the system into a band insulating regime, in contrast to e.g. the 5d iridate NaIrO<sub>3</sub> [159, 160].

In order to understand the influence the vHs has on electronic correlations, we per-

formed calculations at an artificial filling of two electrons in the  $t_{2g}$  shell. Adjusting the filling to two electrons yields a shift in the chemical potential, which removes the vHs from the Fermi level, while remaining at a characteristic Hund's metal filling [18]. By comparing the quasi particle mass enhancement obtained at a filling of two and four electrons, we find that indeed electronic correlations are strongly enhanced by the presence of the vHs. This is similar to the ruthenates  $\text{Sr}_2\text{RuO}_4$  [4, 127–129, 131–145] and  $\text{BaRuO}_3$  [161, 162], where the van-Hove singularity is known to strongly impact electronic correlations.

With the goal of studying the influence of SOC on electronic correlations we performed calculations at varying SOC strength and find that indeed at low SOC quasi particle mass enhancements are strongly enlarged by Hund's coupling. At increasing SOC, however, we find a non-trivial decrease in electronic correlations that we can trace back to two effects. First, due to the splitting of the vHs with SOC the density of states around the Fermi level gets reduced, yielding a decrease in electronic correlations. Second, we identify a competition between the atomic states favoured by SOC and Hund's coupling (c.f. Sec. 5.4.1), which diminishes the influence of the latter.

Finally, we place  $\text{BaOsO}_3$  in a phase diagram in the  $U$ - $\lambda$  plane, where we identify a metallic, a Mott and a band insulating regime. Further, we find that, consistent with experiment [37],  $\text{BaOsO}_3$  is on the boundary of the metal-insulator transition. Concluding this chapter, we want to emphasize that electronic correlations in  $\text{BaOsO}_3$  are governed by a complex interplay of Hund's physics, SOC and details of the band structure (vHs). It is this interplay that makes  $\text{BaOsO}_3$  an highly interesting material to study and we believe that our work therefore contributes to a more complete understanding of strongly correlated materials and their fascinating properties.



# Chapter 6

## Formation of weakly coupled sublattices in thin films of tetragonal CuO

The following results are based on the author's publication [1].

In the last 35 years a great research effort has been made to investigate high-temperature superconductivity in cuprates [16, 47, 163–166]. Early on their quasi 2D planes were identified as key elements for the understanding of the cuprates low-energy physics and therefore two-dimensional (2D) models were proposed [48, 167–171].

Most cuprates do however feature distortion or disorder effects not captured by typical models and therefore a highly symmetric *ideal* cuprate would be an important step to connect materials and low-energy models. A class of candidate materials are polymorphs of pure CuO planes [172]. Unfortunately, contrary to other binary transition metal oxides (MnO, FeO, CoO, NiO), CuO crystallizes in a lower symmetric monoclinic structure [42] and not in a cubic or tetragonal phase that is made up of CuO planes.

However, a few years ago it was shown that when thin films of CuO are grown on a SrTiO<sub>3</sub> substrate [43–45] a structure consisting of tetragonal 2D planes stacked in a staggered configuration along the *c*-direction is realized.

Multiple first principles studies including DFT with hybrid functionals [173–176] and DFT+U [177, 178] followed and gave insights about the electronic structure of tetragonal CuO (t-CuO).

In addition, they proposed an antiferromagnetic stripe order [173, 174, 176], which

is in agreement with experimental findings from resonant inelastic x-ray scattering (RIXS) [49]. Extrapolation from other binary transition metal oxides [43, 179] and estimates from first principles calculations [173, 174, 176] place the Néel temperature around  $\sim 800$  K, which is much higher than the critical temperature of its monoclinic bulk phase ( $T_N \sim 220$  K [180]) and therefore indicates much stronger antiferromagnetic correlations. It is due to these observations that we also studied magnetic properties within CDMFT and variational cluster approximation (VCA) [57] choosing clusters that allow for this ordering. Note that VCA was not introduced in this thesis as the author is not the expert on the method, however, in the section presenting the VCA results (Sec. 6.6) we will give a short overview.

t-CuO was measured to be an insulator with quite sizeable gap  $\Delta > 2.35$  eV via angle-resolved photoemission spectroscopy (ARPES) [45] and its electronic structure was used to construct effective three- and one-band  $t - J$  models [45, 181, 182]. The effective one-band model derived from RIXS in Ref. [49] is in qualitative agreement with the one derived from a Zhang-Rice singlet [48] (ZRS) description [182] and is thus the one we were considering during this thesis.

In Sec. 6.1 we will introduce the model we used for our CDMFT and VCA calculations. Further, we are going to investigate the dynamical influence of the inter-sublattice hopping  $t_d$  in Sec. 6.2 by analysing the corresponding elements of the Matsubara self-energy computed by CDMFT with the impurity solver introduced in Chap. 4. Our key finding is that the inter-sublattice correlations are heavily suppressed as compared to local and short-range intra-sublattice correlations, which formally justifies to regard t-CuO as weakly-coupled interlaced CuO<sub>2</sub> lattices. Motivated by this observation, we introduce in Sec. 6.3 a block-construction scheme for self-energies which allows us to treat twice the amount of correlated electronic orbitals for the same computational cost. In Sec. 6.4 we use this efficient scheme together with our impurity solver working directly on the real axis [36, 83, 84, 183–185] to reproduce equal energy maps and momentum resolved spectral functions in remarkable agreement with ARPES measurements without the need for analytic continuation. In Sec. 6.5 we analyse the magnetic ordering in t-CuO as a function of temperature using CTQMC and identify two driving mechanisms for the insulating phase. Finally, in Sec. 6.6 we give brief introduction to VCA and use it to predict the presence of superconductivity (SC). As a direct consequence of the sublattice decoupling, we find coexistence of magnetic stripe order and superconductivity of  $d_{xy}$ -symmetry, whereas the usual cuprate  $d_{x^2-y^2}$  order is strongly suppressed. This can be interpreted as pairing only happening within sublattices and is therefore an exciting result.

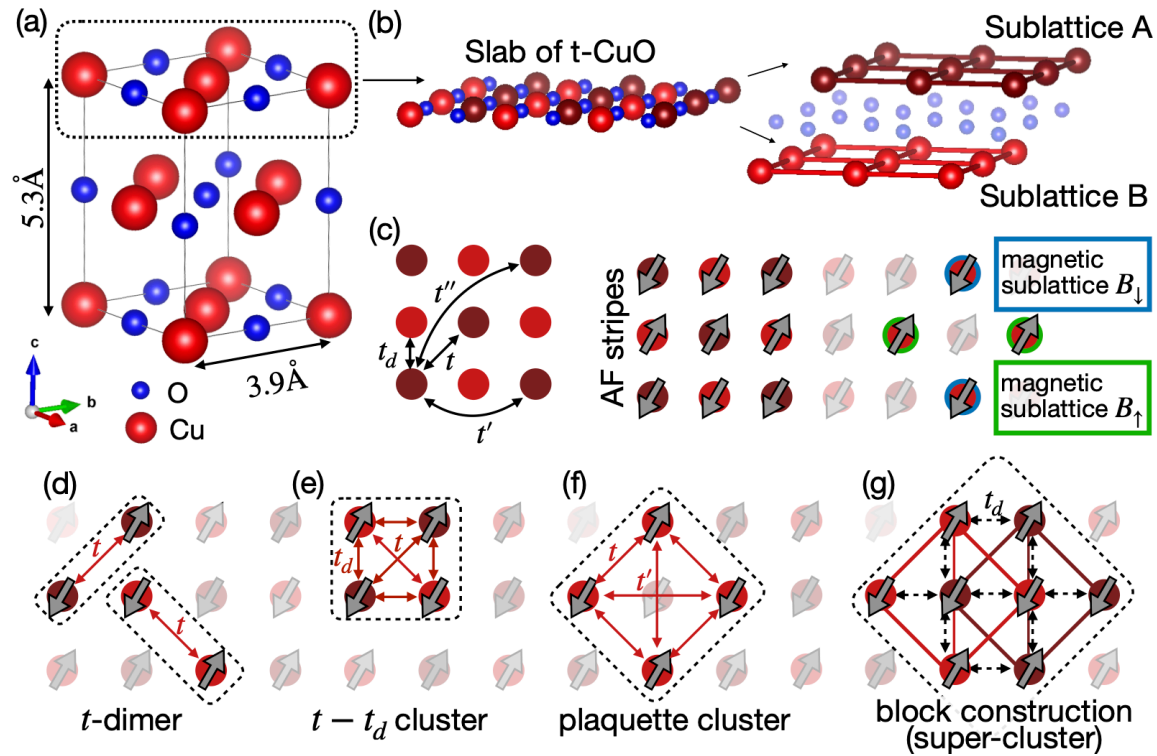


Figure 6.1: (a) Rock salt crystal structure of tetragonal CuO. (b) slab of CuO within the a-b plane. Bright (dark) red atoms indicate the sublattice A and B of our model. (c) Two identical Cu-sublattices and indication of the hoppings  $t_d$ ,  $t$ ,  $t'$  and  $t''$  included in the model. The arrows sketch the stripe order considered throughout the paper. Highlighted in blue and green are the magnetic sublattices that correspond to the stripe order. (d-g) Clusters including different hopping terms as discussed in the text.

## 6.1 Model Hamiltonian

In Fig. 6.1 we show the crystal structure of thin films of t-CuO. As mentioned in the last section, t-CuO consists of 2D planes that are stacked in a staggered configuration (see Fig. 6.1(a)). Due to the large separation between layers the material can be treated as quasi 2D, which is why we consider a single plane of CuO, that can be interpreted as two interpenetrating  $\text{CuO}_2$  sublattices (see Fig. 6.1(b)). The model

we consider is a single band Hubbard model [15, 22, 23]

$$\begin{aligned}
 H = U \sum_i n_{i\uparrow} n_{i\downarrow} + \sum_{\substack{i,j,\sigma \\ |\mathbf{i}-\mathbf{j}|=a}} t_d c_{i\sigma}^\dagger c_{j\sigma} + \sum_{\substack{i,j,\sigma \\ |\mathbf{i}-\mathbf{j}|=\sqrt{2}a}} t c_{i\sigma}^\dagger c_{j\sigma} \\
 + \sum_{\substack{i,j,\sigma \\ |\mathbf{i}-\mathbf{j}|=2a}} t' c_{i\sigma}^\dagger c_{j\sigma} + \sum_{\substack{i,j,\sigma \\ |\mathbf{i}-\mathbf{j}|=2\sqrt{2}a}} t'' c_{i\sigma}^\dagger c_{j\sigma}
 \end{aligned} \tag{6.1}$$

with  $i, j$  being site indices and  $\sigma \in \{\uparrow, \downarrow\}$ .

Contrary to the approach of wannierising orbitals obtained from DFT in Chap. 5, here we use single particle terms ( $t_d = -0.1$  eV,  $t = 0.44$  eV,  $t' = -0.2$  eV,  $t'' = 0.075$  eV) that were obtained as a result of fitting the magnon dispersion, measured by RIXS, with a  $t$ - $J$  model in Ref. [49]. In Fig. 6.1(c) we depict these hopping matrix elements graphically. Please note that the nearest neighbour hopping  $t_d$  is roughly four times smaller than the next nearest neighbour hopping. The reason can be found in Fig. 6.1(a,b) where it becomes apparent, that the oxygen atoms lie between next nearest neighbours instead of nearest neighbours. Thus thinking in terms of a Zhang-Rice singlet [48](ZRS) construction it becomes apparent that the dominating hopping has to be next-nearest-neighbour, as the mechanism behind it is the coupling to a virtual ZRS state that is formed between a hole on the oxygen p-orbitals and the copper  $d_{xy}$  orbital. Note that this is different from usual cuprates, where the oxygens are between nearest-neighbours and thus the copper  $d_{x^2-y^2}$  orbital would contribute to the ZRS. Additionally  $t_d$  is the only hopping term that connects the two  $\text{CuO}_2$  sublattices. We use a Hubbard interaction of interaction strength  $U = 7$  eV, that is significantly stronger than the one in Ref. [49]. However, such strong interactions are necessary to obtain a gap larger than the experimental lower bound of 2.35 eV [45]. Similar values of  $U$  have been used in LDA+U calculations [177, 178], which gives us confidence in our choice for the interaction strength. Note that Fig. 6.1(c) also shows the magnetic stripe order in a single layer of t-CuO. This order was not enforced by any kind of static field in our calculations. The only input we gave was a self-energy corresponding to an initially polarized system afterwards we let the system relax over the iterations and still obtained stripe order. We mentioned in Chap. 2 that in CDMFT an entire cluster of sites is treated as impurity system. Such clusters are depicted in Fig. 6.1(d-g). Namely, Fig. 6.1(d,e) show the clusters used to investigate the sublattice decoupling, while the ones depicted in Fig. 6.1(f,g) are the ones needed for the block-construction. The careful reader may have realised that the super lattice construction consisting of the cluster Fig. 6.1(f) would not span the entire lattice, but only one  $\text{CuO}_2$  sublattice. This is indeed true, but as we will

explain in Sec. 6.3 this is exactly what is needed for the efficient calculation of the diamond cluster in Fig. 6.1(g).

Concluding this section we want to give a few details about typical parameters for our solver used in this project. The calculations on the imaginary axis were carried out using a Matsubara frequency grid corresponding to a fictitious temperature of  $\beta_{\text{fict}} = 200 \text{ eV}^{-1}$ , a number of bath sites  $L_b = 8$  ( $L_b = 6$ ) per correlated site for clusters containing two (four) sites and allowing for a maximal bond dimension of 2048 during ground state searches. The time evolution was performed until the norm of the excitations decayed under  $10^{-8}$ . Calculations on the real axis were carried out with a broadening of 0.05, a number of bath sites  $L_b = 274$  ( $L_b = 200$ ) per correlated site in the case of clusters with two (four) sites and allowing a maximal bond dimension of 1536 during ground state searches. The time evolution was performed until  $T_{\text{max}} = 60 \text{ eV}^{-1}$ . For details about the VCA calculations and CDMFT + CTQMC we refer the reader to the original work [1].

With those computational details out of the way we can now concentrate on the intriguing physics in t-CuO.

## 6.2 Sublattice decoupling

A major point of this project was figuring out the microscopic origin of the  $\text{CuO}_2$  sublattice decoupling in t-CuO, which is hard to argue for on the single particle level as the inter sublattice hopping  $t_d$  is roughly of the same order of magnitude ( $|t_d| \sim t/4$ ) as the leading order hopping  $t$ . It is therefore important to take into account the self-energy which captures the modification the non-interacting Hamiltonian experiences due to the interaction with the other electrons. CDMFT seems like the perfect framework to investigate the effect of treating non-local correlation effects mediated by different hopping terms as by the choice of our impurity cluster we can decide which hopping term is treated perturbatively and which in an exact manner. Namely, all those contained within the cluster are treated exactly, while the others are encoded in the bath degrees of freedom. Thus to investigate the dynamical influence of  $t_d$  it makes sense to treat two kinds of clusters. One where the cluster is located on a single  $\text{CuO}_2$  sublattice and the coupling to the second sublattice is fully encoded in the bath degrees of freedom, and another bigger one, that contains one such cluster on every sublattice. We can then compare the results we obtain, when pretending that the sublattices are disconnected, to the calculation on the larger cluster. The former consists essentially only of two copies of the self-energy obtained from the smaller cluster. We apply this idea by computing the self-energy for the

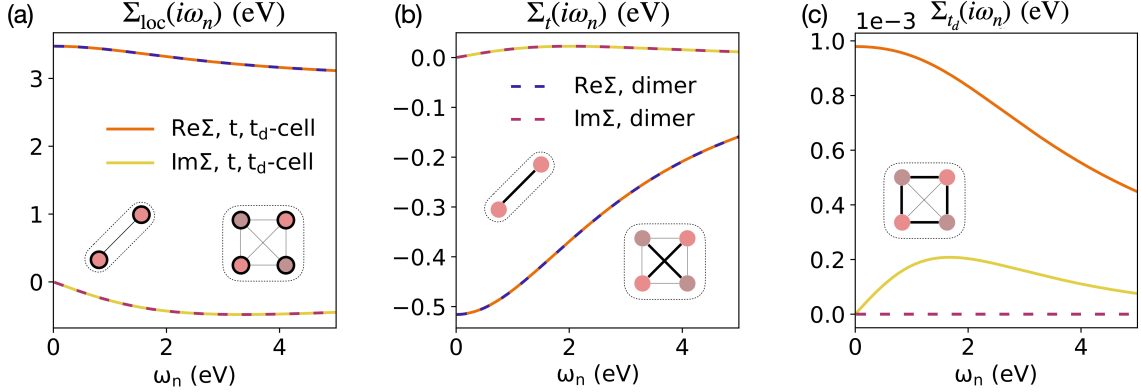


Figure 6.2: Comparison between selected elements of the self-energy computed on two different clusters using the solver introduced in Chap. 4. Note the difference in scales between panels (a,b) and (c). The components shown belong to the block of the up-spin self-energy. The small graphics in each panel depict whether the self-energy element corresponds to local or hopping terms and in the latter case to which. Different coloured sites correspond to different  $\text{CuO}_2$  sublattices.

$t - t_d$  cluster and the  $t$  dimer respectively (cf. Fig. 6.1(d,e)).

In Fig. 6.2 we show chosen elements of the self-energy computed in the above described manner at zero temperature ( $T = 0\text{K}$ ). We denote the local component by  $\Sigma_{\text{loc}}(i\omega_n)$  and the components corresponding to the nearest neighbour hopping  $\Sigma_{t_d}(i\omega_n)$  and  $\Sigma_t(i\omega_n)$ , respectively. In Fig. 6.2(a,b) we show the self-energy elements already included on the dimer and find that the inclusion of the second sublattice and the inter sublattice hopping  $t_d$  does actually not change the self-energy significantly. Furthermore, as shown in Fig. 6.2(c) the self-energy component corresponding to the inter sublattice hopping is about three orders of magnitude smaller than the self-energy elements contained on a single sublattice. Actually we computed the relative difference of the self-energies via the Frobenius norm and found it to be on order  $10^{-4}$  over the entire frequency range. This indicates that electronic correlation effects are not affected by the presence of the second sublattice. This is far from trivial given the relative size of the inter sublattice hopping wrt. the leading order hopping ( $|t_d| \sim t/4$ ) and means that electronic correlations strongly favour the hopping of electrons on a single sublattice. We believe that the driving mechanism behind the formation of sublattices is that the hoppings  $t_d, t, t'$  and  $t''$  are not monotonically decaying with distance. The leading order hopping is favoured by correlations no matter if its nearest or next nearest neighbour. In typical cuprates the nearest neighbour hopping is of leading order and the entire lat-

tice is connected through leading order hopping processes. However, in t-CuO this is not the case, here the fact that the next-nearest neighbour hopping is of leading order means that only one CuO<sub>2</sub> sublattice can be reached via leading order hopping processes. We believe that it is for this reason that the inter-lattice self-energy is strongly suppressed.

Not only does this result explain the physical origin of the sublattice decoupling and justifies thinking of t-CuO as two disconnected sublattices, it also enables us to devise a block construction scheme for the efficient calculation of self-energies. We will introduce this scheme in Sec. 6.3, but before we do we want to mention a few interesting results connected to the sublattice decoupling that were not shown in the original work.

### 6.2.1 Exact Diagonalization study

With the goal of a better classification of the sublattice decoupling we investigated the  $t - t_d$  cell depicted in Fig. 6.1(e) by the means of exact diagonalization. The reason why we chose the  $t - t_d$  cluster is that it is the smallest cluster that we can properly investigate the sublattice decoupling with. Note that within this investigation we do not consider any form of self-consistency loop or addition of bath sites, but simply investigate the four sites composing the  $t - t_d$  cell, which means all other hopping terms are ignored.

Numbering the sites such that odd numbered sites belong to sublattice A and even numbered ones to sublattice B, we define two states which we want to use to characterize the eigenstates of the system. Those states are given by

$$|t\rangle = \hat{s}_{13}\hat{s}_{24}|0\rangle \quad (6.2)$$

$$|t_d\rangle = \frac{1}{\sqrt{2}}(\hat{s}_{12}\hat{s}_{34} - \hat{s}_{23}\hat{s}_{41})|0\rangle \quad (6.3)$$

with  $\hat{s}_{ij} = \frac{1}{\sqrt{2}}(c_{i\uparrow}^\dagger c_{j\downarrow}^\dagger - c_{i\downarrow}^\dagger c_{j\uparrow}^\dagger)$  and  $|0\rangle$  being the vacuum. The operator  $\hat{s}_{ij}$  was chosen such that applied to a dimer consisting out of the sites  $i$  and  $j$  it creates the double occupancy of the zero momentum state but projects out the real space double occupancies. The guess of those states was motivated by the minimization of the kinetic energy along the bonds connected by the hoppings  $t$  and  $t_d$ , respectively. However, as Hubbard repulsion strongly penalizes double occupancies we projected those out. One can check that the overlap  $\langle t|t_d\rangle$  vanishes, which means that those states might be good candidates to distinguish the ground states character.

In Fig. 6.3(a) we show the lowest energy eigenstates of the  $t - t_d$  cluster together

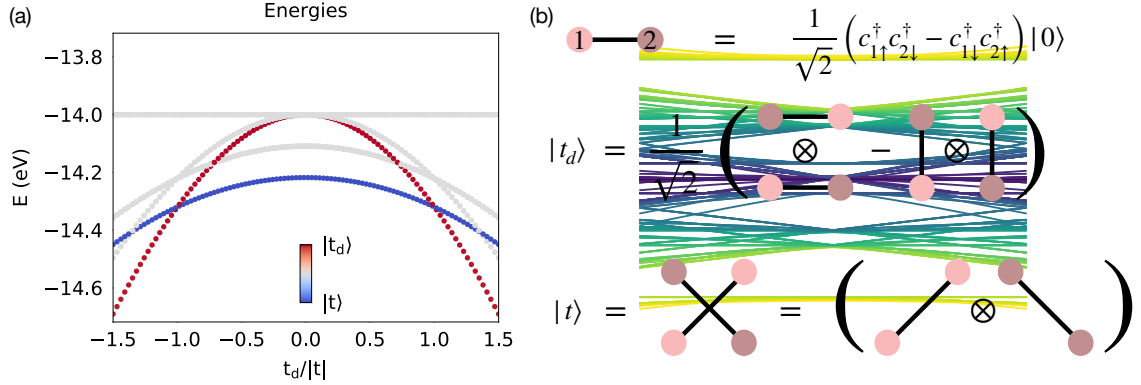


Figure 6.3: (a) Lowest energy eigenstates of the  $t-t_d$  cluster and their corresponding energy in dependency of  $t_d$ . The colour coding is done wrt. the function  $\chi(t_d) = |\langle t_d | E(t_d) \rangle| - |\langle t | E(t_d) \rangle|$ , where  $|E(t_d)\rangle$  is a eigenstate at given  $t_d$ . The upper and lower end of the colour bar correspond to  $\chi = \pm 1$  respectively. (b) Graphical depiction of the states  $|t_d\rangle$  and  $|t\rangle$  the overlaps in (a) are computed with, where  $|0\rangle$  is the vacuum. Note that the state  $|t\rangle$  corresponds to essentially independent subsystems.

with a graphical depiction (Fig. 6.3) of the states we just introduced to characterize the ground state. Investigating panel (a) we observe that around  $|t_d/t| = 1$  the ground state changes its character. Namely, starting from  $t_d = 0$  the ground state has  $|t\rangle$  character, corresponding to two essentially decoupled dimers. However, when  $|t_d/t| > 1$  two energy eigenstates, one with  $|t_d\rangle$  and one with  $|t\rangle$  character, cross and thus the new ground state is of  $|t_d\rangle$  character, which abruptly changes the behaviour of the system from two disconnected dimers to a state that entangles all the sites. This observation may give an indication why the self-energy presented in Fig 6.2 corresponds to two essentially decoupled sublattices. At the ratio of  $|t_d/t| \sim 1/4$  corresponding to t-CuO we are still deep within the regime where the ground state has  $|t\rangle$  character and the change happens very abruptly due to the level crossing, which might explain why  $|t_d/t| \sim 1/4$  is not so much different from  $t_d = 0$ , at least for the effect of electronic correlations. However, we have to be careful not to interpret too much into this result, as not only are we ignoring all the higher order hopping terms in this investigation but we are also very far from the thermodynamic limit as we ignore the rest of the lattice. Thus the results in this subsection should rather be a thought of as a possible indication for the weak dependence on the value of  $t_d$  than a definite proof.

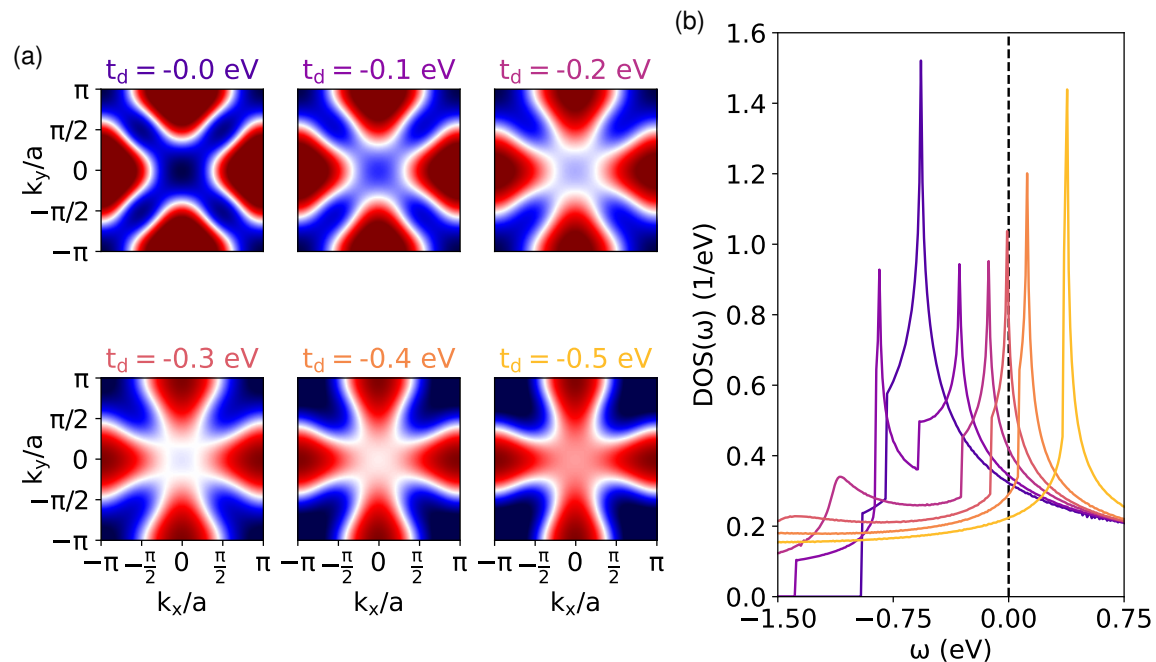


Figure 6.4: (a) Dispersion relation in the non-interacting limit for different values of  $t_d$ . Blue (red) momenta correspond to negative (positive) energies. The white line depicts the Fermi surface. (b) Density of states in the non-interacting limit for varying  $t_d$ . The curves correspond to the equally coloured  $t_d$  in (a). The black dashed line depicts the Fermi level. The heat maps are normalized such that they are centered at zero energy. The maximum and the minimum of the heat maps are set to the most extremal energies in the band, that still allow for said centering.

### 6.2.2 Non-interacting limit

Motivated by our findings in the exact diagonalization study, but struck with the realisation that those may be obtained under too strongly simplified conditions we decided to investigate t-CuO ignoring the strong Hubbard repulsion. This might sound a bit far from our original model as  $U = 7$  eV is everything but not negligible. However, we do not want to actually obtain data for the full problem from this investigation, but rather find hallmarks of why the self-energy in Fig. 6.2 depends so weakly on  $t_d$ . Given that there are only two inputs to CDMFT, namely, the dispersion relation of the lattice in the thermodynamic limit and the impurity cluster, it makes sense to investigate both also individually. Having treated the cluster problem in the last subsection, here we want to investigate the non-interacting limit.

In Fig. 6.4(a) we show the Brillouin zone coloured with respect to the energy of the respective momentum states. The blue regions are occupied by electrons, while the red regions are empty. Investigating the Fermi surface for the case  $t_d = 0$  we find, respecting the periodicity of the BZ, two disconnected circles enclosing the unoccupied states. The states with negative energies are found in the middle of the BZ and on the diagonals. Tuning  $t_d$  this changes slowly, as for  $t_d \in [-0.2\text{eV}, 0]$  the Fermi surface gets slightly twisted, emptying out more and more states close to the middle of the BZ. This change is rather slight in comparison to what happens at stronger  $t_d$ , where an entire region of the BZ is pushed through the Fermi surface. Namely, the states in the middle of the Fermi surface that used to be occupied empty all the sudden leading to a completely different shape of the Fermi surface. Please note that this changes the topology of the Fermi surface. Before the reformation at  $t_d \sim -0.35\text{eV}$  it consists of two disconnected circles, while afterwards, taking into account the periodicity of the BZ, the Fermi surface only consists of a single circle. An abrupt change in the Fermi surface topology like this is in the literature referred to as a Lifshitz transition following Lifshitz's original paper [186]. In Fig. 6.4(b) we show the non-interacting density of state as for the same values for which we also present the maps of the Brillouin zone in Fig. 6.4(a). We note that in the  $t_d = 0$  case there is a single van-Hove singularity (vHs), that gets split as we tune  $t_d$  towards negative values. The part of the vHs that moves towards the occupied side, gets smeared out, while the one moving towards the Fermi surface becomes sharper. The latter eventually crosses the Fermi surface for  $|t_d| > 0.3\text{eV}$ , which is also where the Lifshitz transition happens. We remind the reader that the relevant value of  $t_d$  for t-CuO is  $-0.1\text{eV}$  for which the Fermi surface appears far more similar to the case of  $t_d = 0$ , than to the case after the vHs crosses the Fermi surface. Note that even when hole-doping t-CuO we should still be on this side of the transition even though a density lower than half-filling would yield a shift of the DOS towards higher frequencies. Making this shift large enough to move the vHs through the Fermi surface would require a filling lower than 0.7 electrons per band which is significantly stronger doping than studied in this work. Please also note that since  $t_d$  is the next-neighbour hopping the Fermi surface after the transition should in its shape/topology correspond to the dispersion of typical cuprates with monotonically decreasing hoppings. Again similar to last subsection our observations can not be directly transferred to the full interacting problem as the strong Hubbard repulsion may have all kinds of unforeseen effects. However, we believe that the observations from exact diagonalisation and the non-interacting limit contribute towards a more complete discussion of the sublattice decoupling.

## 6.3 Block construction and cluster orientation

Here we want to give a quick overview of two refinements we used with respect to the pure CDMFT framework, namely, the block construction scheme for self-energies, that allows us to obtain a better momentum resolution and the averaging over cluster orientations that eliminates artificially favouring certain directions in momentum resolved spectra.

### 6.3.1 Block construction

In the last section we showed on the example of the dimer and  $t - t_d$  cluster that the dynamical influence of the  $t_d$  hopping is negligible. As  $t_d$  is the only term connecting the two  $\text{CuO}_2$  sublattices this can be used to treat clusters consisting of twice as many sites.

The idea is to assume that the self-energy becomes block diagonal with one block per sublattice. This is true if the components corresponding to  $t_d$  vanish and all the other components of the self-energy are not influenced by  $t_d$ . As shown in Fig. 6.2 this seems to be a fair assumption.

Furthermore, since the two  $\text{CuO}_2$  sublattices are identical, it is enough to just compute the block of one sublattice and determine the other one from symmetry. Thus we only need to solve the impurity problem within one sublattice to obtain the self-energy. Once it is obtained we construct the full self-energy by the scheme just described and close the self-consistency loop with the full dispersion including  $t_d$ . This way effects of  $t_d$  are still included on a perturbative level. After closing the self-consistency loop we project down onto one of those blocks and obtain an impurity problem on the unit cell of a single sublattice (Fig. 6.1(f)). In the following we will perform block construction calculations treating a plaquette cluster on a single sublattice (Fig. 6.1(f)) which we then use to build a diamond cluster on the full lattice (Fig. 6.1(g)). The benefit of having more sites in the unit cell is that the momentum resolution is increased as longer ranged correlation effects are taken into account. By this construction we are able to obtain a momentum resolution corresponding to an eight site cluster with the computational effort of treating a impurity model with four correlated sites. In the following we will refer to the described diamond cluster as block construction.

### 6.3.2 Cluster Orientation

Most of the results in this project were obtained by using the diamond cluster or the dimer as unit cells. However, those clusters break the rotational symmetry of

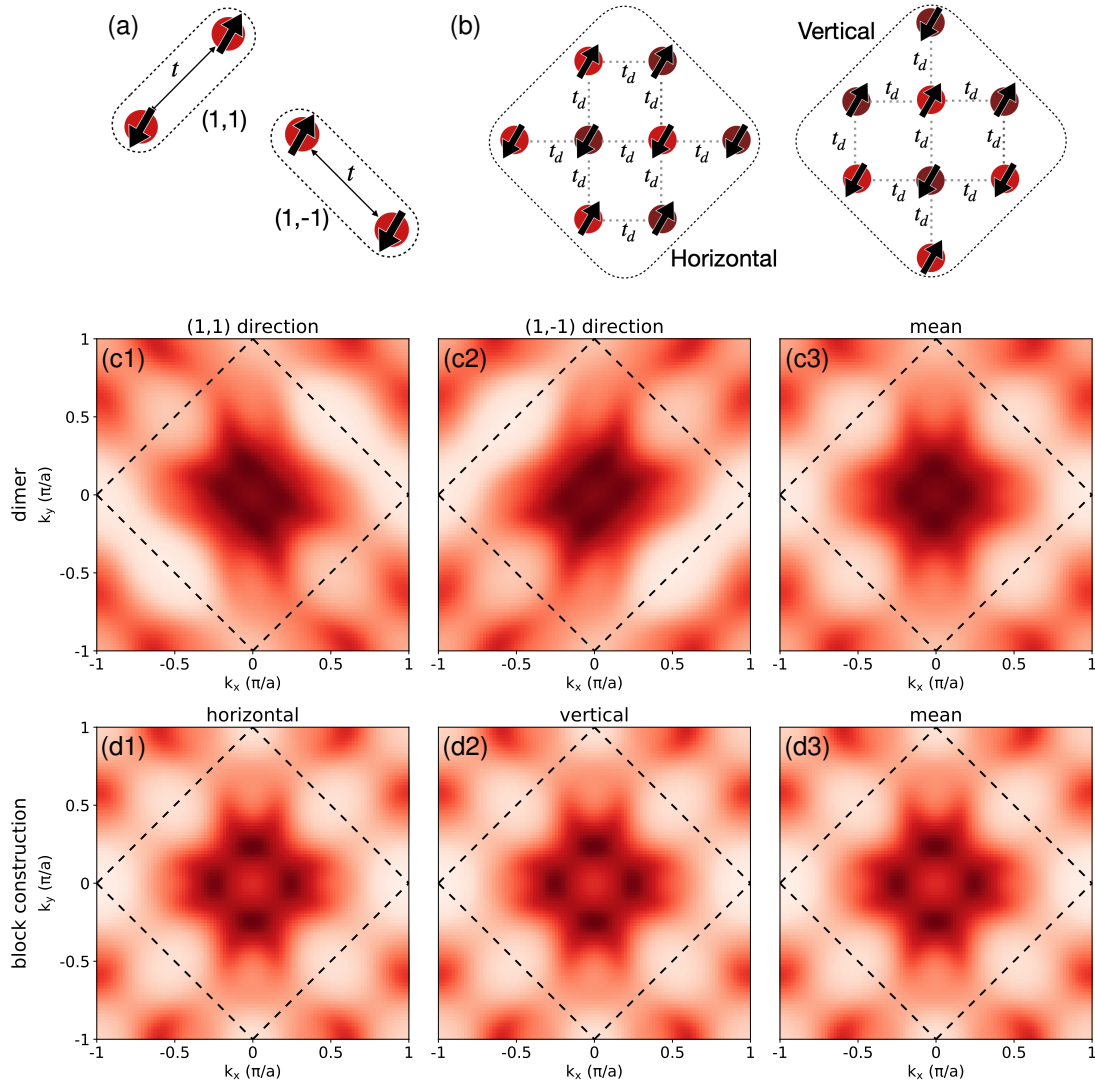


Figure 6.5: Sketch of the two possible orientations within a given magnetic stripe order for (a) the dimer and (b) the diamond cluster. Panels (c) and (d) show the corresponding equal energy maps obtained at  $E = -2.2$  eV using these cluster orientations as well as their mean. The dashed black line indicates the BZ of a single sublattice.

the lattice as rotating them by  $90^\circ$  results in a different cluster setup as depicted in Fig. 6.5(a,b). It is for this reason that for the remainder of this chapter we will average over those two equivalent orientations whenever displaying momentum resolved spectra. This averaging approach goes by the name oriented cluster DMFT and was already introduced in Refs. [187, 188] and applied to  $\text{Sr}_2\text{IrO}_4$  [187–189]. The result of this procedure can be seen in Fig. 6.5(c,d), where we display equal energy maps computed with the dimer and diamond cluster respectively. The sub panels (c1,c2,d1,d2) show the spectra obtained by only choosing one direction, while the ones in sub panels (c3,d3) display the averaged result. We observe that the dimer results are far more sensitive to the orientation, however apart from the minimum in the middle of the BZ their average is already very similar to the energy maps computed with the block construction. This implies that the dimer results already capture very well the physics in t-CuO, which indicates that the most important physical content of the extended unit cells is actually the delocalisation along the dominating bonds, as we argued in Sec. 6.2. Furthermore, the block construction does only seem to depend very weakly on its orientation, which we interpret as a hint towards convergence in cluster size.

## 6.4 Spectral functions

In this section we compare the momentum resolved spectral functions that were computed using the block construction scheme to experimental data from ARPES measurements [45]. The results presented in this section were computed using our solver but working directly on the real axis [36, 83, 84, 183–185], allowing to directly access the real frequency data without the need for analytic continuation. The computations to obtain the results presented in this section were performed in equal parts by the author and Martin Grundner [83, 84].

In Fig. 6.6(a) we show an equal energy map computed at  $-2.2\text{ eV}$ , which in our model is at the top of the valence band. This equal energy cut reproduces well the experimentally measured data (cf. [45] Fig. 1(a)). Namely we are able to reproduce the four strong maxima, that are close to the center of the BZ and are offset by  $90^\circ$ . Furthermore we are also able to reproduce the replica features outside the BZ that corresponds to a single  $\text{CuO}_2$  sublattice (dashed black line). In contrast to ARPES our method is not subject to matrix element effects [190] which is why our replicas do not undergo any additional intensity modulations. The reason why the replicas are not perfect is because the sublattices are not entirely disconnected. If this was the case ( $t_d = 0$ ), then the true BZ would be the one of a single sublattice and everything outside would just be periodically repeated. Thus the presence of

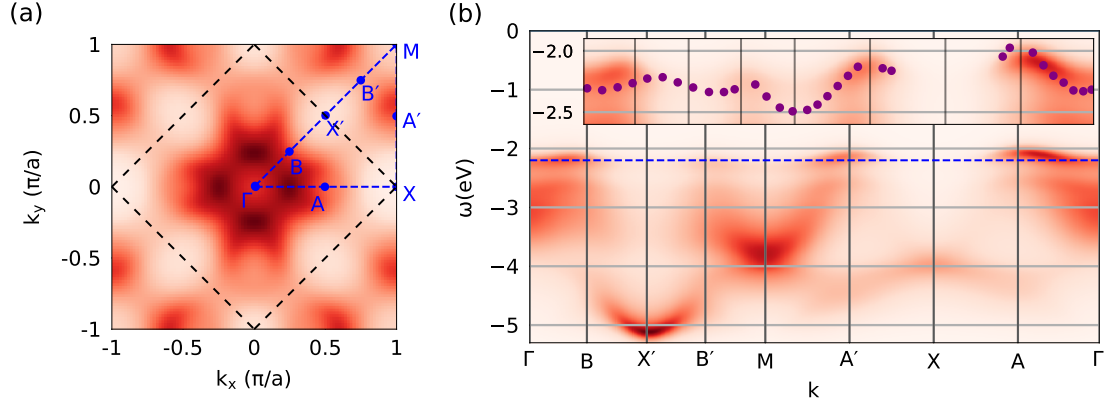


Figure 6.6: Spectral function  $A(\mathbf{k}, \omega)$ . (a) Equal energy map at  $E = -2.2$  eV where the dashed black line depicts the first BZ of a single sublattice. (b)  $A(\mathbf{k}, \omega)$  along high-symmetry  $\mathbf{k}$ -path as computed with the block-construction scheme and compared to the experimentally measured dispersion (purple circles in inset) extracted from Ref. [45] and shifted by 0.4 eV in order to align the chemical potentials. The dashed blue line in (b) depicts the energy (-2.2 eV) at which the equal energy cut was calculated.

the replica features is a hallmark of the weak coupling between the sublattices. The fact that there is only very slight asymmetry is due to electronic correlation effects. In more detail, since the inter sublattice components of the self-energy are strongly suppressed the inter sublattice hopping  $t_d$  is kept bare, while electronic correlations roughly enhance the leading order hopping by a factor of 2 (see Fig. 6.2). Comparing the correlation enhanced value of  $t$  with  $t_d$ , we find that the former is roughly 10 times larger, which explains why the asymmetry is so small even though the bare  $t_d$  is roughly one fourth of the bare  $t$ . Note that the asymmetry from choosing a cluster orientation was taken care of by the averaging procedure introduced in the last section. The remaining asymmetry between  $x$  and  $y$  direction is solely due to the antiferromagnetic stripe order. In Fig. 6.6(b) we show the momentum resolved spectral function along a high symmetry path through the BZ. Note that the path is the one depicted as dashed blue line in Fig. 6.6(a) and the spectrum was measured along the same path by ARPES (Ref. [45] Fig. 2(a)). Comparing to the latter we find good agreement. In particular the low energetic band that is separated from the rest of the Hubbard band at higher binding energy coincides quite well with the experimental data (see inset of Fig. 6.6(a)). This band stems from a spin-polaron

i.e. a hole propagating in the antiferromagnetic background. It is reasonable that this feature is well captured by our model as the hopping elements we used were obtained by fitting the magnon dispersion and in essence the spin-polaron should in some sense be a electronic hole interacting with those magnons. In addition to this low energy feature we are the first ones to reproduce the vanishing spectral weight around the  $X$  point, a feature that could not be reproduced by a self-consistent Born approximation (SCBA) calculation on a ZRS spin model [48, 182]. In addition to those features the experiment also shows a lower lying band that is labelled with  $\beta$  in the experimental work [45]. It is not possible for us to reproduce this additional band, as our model is a *single* band Hubbard model reproducing well the Zhang-Rice [48, 182] like band, while the  $\beta$  band was identified to have a different symmetry [45, 172]. We want to mention that upon hole-doping the additional holes are expected to be hosted on the oxygen p-orbitals which form Zhang-Rice-singlets with the holes in the copper d-orbitals [48, 172]. Thus as the  $\beta$  band has different character and is further removed from the Fermi level it is not expected to play a significant role upon doping. Apart from the missing  $\beta$  band the agreement of our computed spectra with experiment is quite striking.

## 6.5 Finite Temperature Analysis

In the literature there have been multiple predictions about Néel temperature for the antiferromagnetic stripe order in t-CuO [43, 173, 174, 179] which motivated us to closer investigate the finite temperature behaviour of our model. We thus perform finite temperature CDMFT calculations by the use of a continuous time quantum Monte Carlo (CTQMC) solver [53–55]. These finite temperature CDMFT+CTQMC calculations were performed by Benjamin Bacq-Labreuil.

In order to get a feeling for the cluster size dependence of our results we perform calculations using the dimer and the block construction clusters (Fig. 6.1(d,g)).

In Fig. 6.7(a) we show the staggered magnetization corresponding to the stripe order for both the dimer and block construction clusters. Our first observation is that the finite temperature curves nicely extrapolate to the zero temperature results obtained from the solver introduced in Chap. 4. Furthermore we identify the inverse temperature  $\beta_c$  at which the order melts for the dimer and the block construction cluster to be  $\beta_c^{\text{dimer}} = 14.5 \text{ eV}^{-1}$  and  $\beta_c^{\text{block}} = 18.5 \text{ eV}^{-1}$  respectively. Those correspond to critical temperatures  $T_c^{\text{dimer}} \approx 800 \text{ K}$  and  $T_c^{\text{block}} \approx 627 \text{ K}$ . In order to not disrupt the flow of this section too much we will explain details about how we obtained the critical temperature and the error bars in the next subsection. We observe that the dimer cluster still overestimates the magnetic order, while the block construction

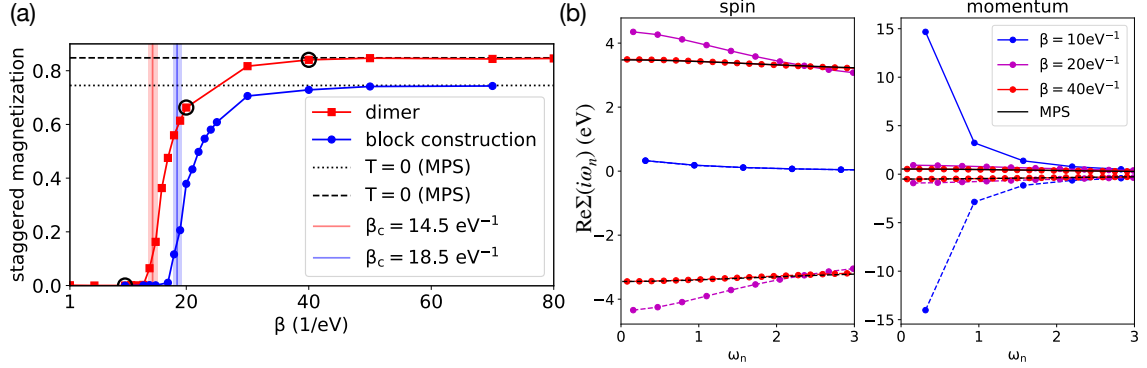


Figure 6.7: (a) Staggered magnetization calculated using the dimer cluster and the block-construction. The dashed black lines indicate the  $\beta = \infty$  result computed with the impurity solver on the imaginary axis introduced in Chap 4, while the finite temperature results were obtained by CTQMC [53–55]. The vertical lines depict the inverse critical temperature  $\beta_c = (18.5 \pm 0.7) \text{ eV}^{-1}$  ( $(14.5 \pm 0.8) \text{ eV}^{-1}$ ) for the block-construction (dimer) cluster. The shaded area depicts the error bar for  $\beta_c$ . (b) Real part of the diagonal components of the self-energy for different inverse temperatures  $\beta$  indicated by black circles in (a). The curves shown left correspond to the spin up (solid) and down (dashed) components on a cluster site. On the right, we show the self-energy at the two cluster momenta  $K_1 = (0, 0)$  (dashed) and  $K_2 = (0, \frac{\pi}{a})$  (solid) respectively.

which also includes slightly higher ranged correlations leads to a lower value. We might now be tempted to interpret these as predictions for the Néel temperature. However as we are considering a 2D model, ignoring the other layers stacked upon the  $c$ -axis there should not be a long range magnetic stripe order as fluctuations between the equivalent directions should immediately destroy the order [191]. Thus the long-range order we observe in our finite temperature calculations is rather a hallmark of choosing one of the equivalent stripe orientations in a mean-field like approach. Still, we believe that the reduction of  $T_c$  upon extending the cluster size nevertheless shows the importance of including in-plane spin fluctuations.

In Fig. 6.7(b) we show real parts of Matsubara self-energies at three characteristic temperatures, namely one in the paramagnetic (PM) regime, one in the transition region and one in the antiferromagnetic (AF) regime. Again the first observation is that the finite temperature CTQMC data seems to converge asymptotically to the MPS results for increasing  $\beta$ . We also see that the frequency dependence gets strongly suppressed as temperature decreases (that is as polarization increases). This

can be interpreted in terms of a smaller active space for the electrons (holes) which leave less room for dynamic electronic correlation effects. Please note that the static correlation effects are still sizeable though as can be seen from the large but close to constant values the self-energy takes. The smaller active space in the ordered phase can be thought of in terms of electrons being frozen in place as moving in the direction of the stripes is forbidden by Pauli's exclusion principle, and while being allowed, hopping perpendicular to stripe direction is penalized by the large Hubbard repulsion  $U$ . Even in the paramagnetic regime (here at  $\beta = 10 \text{ eV}^{-1}$ ) the material is still insulating as the Matsubara Green's function does still tend to 0 (not shown here). However in the PM case we can not argue by the means of reduced active space, here it is rather a momentum selective dynamic level splitting that suppresses electron dynamics by largely penalizing non-zero momentum states. In the following we want to elaborate in a bit more detail about how we extracted the critical temperatures.

### 6.5.1 Details on the estimation of the critical temperatures

In order to extract the estimate to the critical temperature during the last section we fitted a function of the form

$$M(T) = \theta(T_c - T)\gamma \left(1 - \frac{T}{T_c}\right)^\beta$$

to the staggered magnetization. Here  $\gamma$ ,  $T_c$  and  $\beta$  are fit parameters and  $\theta$  is the Heaviside step function, that was added in order to make the fits more stable. Note that here  $\beta$  is the critical exponent of the transition, while  $\beta_c$  in the following denotes the inverse critical temperature.

To improve our fitting procedure we inspected the Matsubara self-energies and found upper and lower boundaries for  $\beta_c$ . Namely, on the one hand we set the lower boundary such that the spin splitting vanishes since this indicates that electrons with different spins behave completely identical and thus the system is for sure not antiferromagnetic. On the other hand the upper boundary is set such that the imaginary part of the diagonal components of the self-energy tends to 0 as  $\omega_n \rightarrow 0$ . This is a reasonable choice as in the case of a paramagnetic Mott insulator the self-energy is divergent somewhere in the gap. Since our chemical potential is set such that  $\omega = 0$  roughly corresponds to the middle of the gap, the vanishing self-energy indicates that we are not anymore in the paramagnetic phase. By this criterion we identify  $\beta_c = 16 \text{ eV}^{-1}$  ( $\beta_c = 20 \text{ eV}^{-1}$ ) and  $\beta_c = 13 \text{ eV}^{-1}$  ( $\beta_c = 17 \text{ eV}^{-1}$ ) as upper and lower boundary for the dimer and block-construction clusters, respectively.

Varying the upper and lower boundaries of the fit interval we obtain a collection of fits, of which we discard those, which either display a deviation bigger than 0.05 from any data point or which do not give  $\beta_c$  in the region that was determined by inspection of the self-energies.

Thus we end up with a collection of valid fits over which we average the resulting  $\beta_c$ . The error bars in Fig. 6.7(a) correspond to the standard deviation in the set of valid fits.

The average values we obtain for the critical exponent are  $\beta = 0.44 \pm 0.15$  ( $\beta = 0.66 \pm 0.34$ ) for the block-construction (dimer) respectively. The errors are again determined as the standard deviation in the set of valid fits. Finally, we note that the exponents are in good agreement with the expected mean-field critical exponent of  $\beta = 0.5$  [192].

Having identified the driving mechanisms of the insulating phases in both regimes at half-filling, in the next section we want to move away from half-filling and investigate the consequences the sublattice decoupling has on superconductivity.

## 6.6 Superconductivity upon Hole-Doping

We investigate the behaviour upon hole doping by the use of the variational cluster approximation (VCA) [57, 193, 194], which is a well established quantum cluster technique. It is based on finding the stationary points of the self-energy functional  $\Omega(\Sigma)$ , which is a Legendre transform of the Baym-Kadanoff functional introduced in Sec. 2 and approximates the grand potential of the system in the space of cluster self-energies [56–58]. It is complementary to the DMFT techniques used in the previous section as the spirit of those is to approximate the Baym-Kadanoff functional while VCA approximates a Legendre transform of the same. Within VCA one usually solves a cluster system for its self-energy which is then used to compute the self-energy functional. The approach is then to vary the existing single particle terms of the cluster Hamiltonian to find the stationary point of the grand potential. This procedure is particularly well suited to check for stable symmetry breaking solutions as it allows for the introduction of additional symmetry breaking Weiss fields, which can also be varied. One can then check if the inclusion of said fields yields a stable stationary point with even lower grand potential, which would thereby be favoured in the thermodynamic system. The VCA computations yielding the results of this section were performed by Benjamin Lenz.

It was shown in previous studies [195, 196] on  $t - t' - U$  models at half-filling, which in our case would correspond to taking into account only  $t$  and  $t_d$ , that the competition between antiferromagnetic Néel order and superconductivity of  $d_{x^2-y^2}$  type is

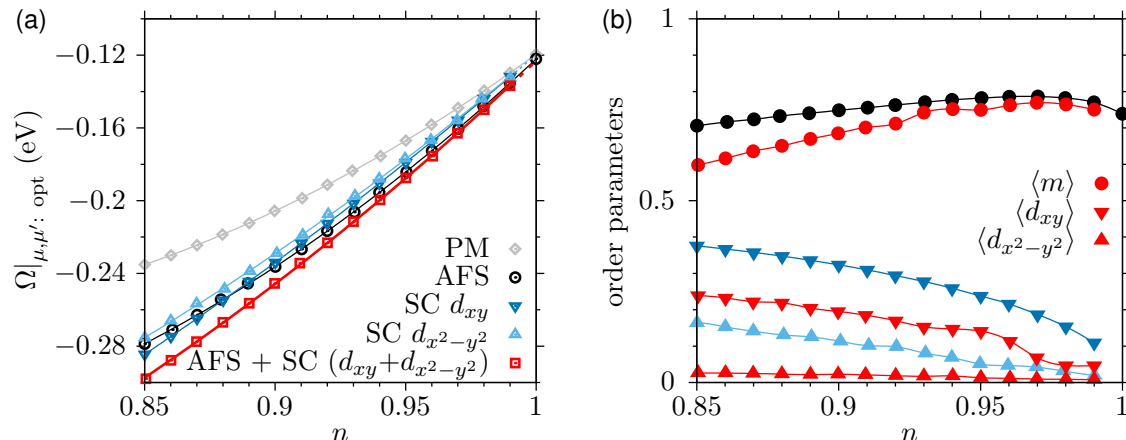


Figure 6.8: (a) Self-energy functional  $\Omega$  as a function of filling  $n$  for different solutions within VCA: Antiferromagnetic stripe order (AFS), superconductivity (SC) of  $d_{xy}$  or  $d_{x^2-y^2}$  symmetry as well as coexistence of all three. Panel (b) shows the corresponding order parameters; the colors correspond to the solutions presented in (a). The red curves in (b) are special as in the coexistence case there are different order parameters for the same solution, which is why we distinguish them via symbols.

prevalent in the case of  $t_d > t$ , while in the case of  $t_d < t$  the competition between stripe order and superconductivity of  $d_{xy}$  type is key. In our case however we are interested in the superconducting order *away* from half-filling.

We therefore included symmetry breaking fields that correspond to two kinds of superconducting order parameters namely one for  $d_{xy}$  and one for  $d_{x^2-y^2}$  order. Furthermore we also introduced an antiferromagnetic Weiss field to include the stripe order and since we wanted to perform our investigation at finite doping we also varied the chemical potential of the cluster and the lattice system  $\mu'$  and  $\mu$ . The cluster we considered is the diamond cluster depicted in Fig. 6.1(g) without the use of block construction. The latter is not possible due to the inclusion of the symmetry breaking field favouring the  $d_{x^2-y^2}$  superconductivity. Note that in principle in CDMFT we could also make the above investigation, however this would at least need us to treat a full eight site cluster with additional bath sites and without enforcing particle number conservation, which if at all possible would yield massive computation times. In Fig. 6.8(a) we show the stationary points of the self-energy functional as function of the filling per orbital  $n$  upon introduction of multiple kinds of symmetry breaking Weiss fields. While all the solutions are lower in energy than the paramagnetic normal state we find that the solution obtained by putting all the fields in competition

is the most stable over the entire range of doping checked.

In Fig. 6.8(b) we show the different order parameters. For all but the coexistence solution we simply show the order parameter of the phase that is favoured by the Weiss field, while for the coexistence solution we present the corresponding order parameter for magnetic stripe order, and both spatial symmetries of superconductivity ( $d_{xy}$  and  $d_{x^2-y^2}$ ). We observe that starting from large magnetization and almost vanishing superconducting order parameters at half filling, the magnetization decreases as we dope the system, while the  $\langle d_{xy} \rangle$  order parameter increases. Even though we include the corresponding Weiss field the  $\langle d_{x^2-y^2} \rangle$  order parameter is strongly suppressed due to an apparent competition with the former two orders.

This result is very exciting to us as in the context of sublattice decoupling the dominating  $d_{xy}$  type superconductivity can be interpreted as  $d_{x^2-y^2}$  superconductivity on every sublattice. As  $d_{x^2-y^2}$  type pairing is the one found in usual cuprates made up of a single  $\text{CuO}_2$  lattice with monotonically decreasing hopping terms, we can interpret this result as the sublattice decoupling even carrying through to the superconducting state in case of hole doping.

## 6.7 Summary

Within this chapter we investigated the tetragonal phase of CuO by the means of a single band Hubbard model of which the single particle parameters were obtained from fitting the magnon dispersion in Ref. [49]. The inspection of Matsubara self-energies revealed that electronic correlations strongly favour the hopping on a single sublattice, leading to a very weak coupling to the second sublattice. With the goal of deepening our understanding of the mechanism behind this decoupling we further investigate a minimal unit cell by the means of exact diagonalisation finding that in this simplified model the decoupling is protected by a level crossing. In order to make the jump to a simplified model in the thermodynamic limit we also study the dispersion of the non-interacting problem, finding that the Fermi surface of the non-interacting model has different topology than the one of cuprates with spatially monotonically decreasing hopping terms. Both the level splitting in the exact diagonalisation case as well as the topologically distinct Fermi surface of the non-interacting problem are interpreted as an indication for the robustness of the sublattice decoupling. Using this decoupling we motivated a block construction scheme for our cluster calculations with which we performed CDMFT calculations directly on the real axis to obtain momentum resolved spectra and compare them to the spectra measured in ARPES experiment [45], which yields excellent agreement and thereby shows that single band Hubbard model is sufficient to describe the electronic structure of t-

---

CuO as long as local and short ranged correlation effects are treated appropriately. We further investigate the behaviour at finite temperature and identify the driving mechanism behind the insulating states both in the paramagnetic and the antiferromagnetic regime. Furthermore by comparing magnetizations obtained for different cluster sizes we can conclude that in-plane spin correlations seem to be important to take into account when determining a critical temperature for the transition to the stripe ordered state. Finally, we investigated the order t-CuO exhibits upon hole doping by the means of VCA and find a coexistence of antiferromagnetic stripes with  $d_{xy}$ -type superconductivity. The latter of which can be interpreted as the sublattice decoupling carrying through to the superconducting state.



# Chapter 7

## Conclusion and Outlook

In this thesis we studied electronic correlation effects in the materials  $\text{BaOsO}_3$  and the tetragonal phase of  $\text{CuO}$  by the means of DMFT and its cluster extension CDMFT. In Chap. 1 we gave an introduction to the topic of electronic correlation effects in real materials. We discussed that band theory can break down, when atomic orbitals become closely localized around their respective atoms position. Furthermore we gave a motivation to employ DMFT as the current state of the art technique to treat electronic correlations and band structure effects on an equal footing. In Chap. 2 we introduced DMFT and CDMFT using the effective action formalism, which lead us to identify DMFT and CDMFT as approximations to the Baym-Kadanoff functional. We gave an indepth discussion of the self-consistent construction of the single particle Green's function and also introduced the concept of reperiodizing Green's functions in the case of CDMFT. In Chap. 3 we introduce the concept of matrix product states, matrix product operators together with the algorithms that are used for ground state searches and time evolutions. In Chap. 4 we introduced the MPS-based impurity solver on the imaginary axis that was implemented and optimized as a large part of this work. We gave a detailed overview of all the steps necessary to perform DMFT on the imaginary axis at effectively zero temperature by the use of MPS. In particular we discussed the importance of symmetries for the convergence of ground state searches and the block structure of dynamical quantities, such as, the impurity self-energy. We also gave a detailed description of how to further enhance the solver by addition of new symmetries and what steps have to be taken to interface it with future models. Equipped with this knowledge in Chap. 5 we presented the results obtained in our study of  $\text{BaOsO}_3$  [2]. The most notable being that  $\text{BaOsO}_3$  is a moderately correlated Hund's metal, in which strong spin orbit coupling and Hund's coupling are in competition. We identified the origin of this competition by

studying the atomic limit, and also found that the splitting of a van-Hove singularity close to the Fermi level has important consequences for the strength of electronic correlations. In Chap. 6 we discussed the results of our recent study [1] on electronic correlation effects in the tetragonal phase of CuO (t-CuO). Our key results are the formal justification of regarding t-CuO as two weakly coupled CuO<sub>2</sub> sublattices due to inter-sublattice correlations being strongly suppressed, as a consequence of the strong on-site correlation effects. In addition, by the use of variational cluster approximation we are able to identify the symmetry of the superconducting order upon hole-doping and show that the sublattice decoupling carries over to the superconducting state.

## Outlook

The author believes that the impurity solver on the imaginary axis that was set up in close collaboration with Martin Grundner is in extremely good shape and for the problems that the solver is currently able to treat there is not much room for improvement.

However, it would be of great interest to implement a finite temperature extension as the solver is currently only able to treat problems at zero temperature. Currently, one has to resort to different solvers like CTQMC to access higher temperatures as we did in the project on t-CuO (cf. Sec. 6.5). Having a finite temperature extension would be highly desirable as it would enable the study of zero and non-zero temperature by the use of a single impurity solver. To our knowledge, currently this is only possible with exact diagonalization, which, however, can not reach as large system sizes. Additionally, it would add another tool to the toolbox for multi messenger type of approaches.

Furthermore, a framework to study superconductivity within the context of DMFT would be desirable, as the origin of unconventional superconductivity is a key object of current research [16, 47, 163–166]. Possible ways to realise said framework would be partial particle hole transformation or in the case where spin-mixing single particle terms are present the Nambu formalism [197, 198]. An instructive explanation for partial particle hole transformation is presented in Benjamin Lenz’s PhD thesis [199]. The author is well aware that studying superconductivity yields the problem of no longer being able to hold on to the U(1) particle number conservation symmetry, which might yield long computation times. However, the use of the recently introduced projected purification method [200] may alleviate some of those problems.

With regard of the projects presented within this thesis, we believe that a more thorough study about the emergence of the side peaks in the spectral function of BaOsO<sub>3</sub> is a promising perspective. This could for example be done by simpler model calcu-

lations featuring a van-Hove singularity close to the Fermi-level. It might even be interesting to tune the position of the vHs as we in principle did when considering SOC in the context of  $\text{BaOsO}_3$ .

Furthermore, we believe that our results on t-CuO show the importance of achieving hole doping in the system. Not only may one be able to confirm the symmetry of the superconducting order parameter predicted in this thesis, but by growing multiple layers of t-CuO one might even be able to investigate a possible dependence as a function of the number of layers grown.

It is the authors belief that all research directions proposed in this section are worth pursuing, which underlines just how interesting strongly correlated materials really are. Investigating their intriguing properties would not be possible without sophisticated methods like DMFT and the respective impurity solvers it relies on. We therefore believe that the development and optimization of novel methods and algorithms contributes strongly towards an holistic understanding of the microscopic properties of these materials and are proud to have made a contribution towards this exciting field of research.



# Acknowledgements

This work would not have been possible, if it were not for all the wonderful people that were around to support me. I want to thank

- **Ulrich Schollwöck** for giving me the opportunity to do research in such an interesting field, always finding some time for discussions and simply for being a great supervisor.
- **Dieter Vollhardt** for being part of my committee and for examining this thesis.
- **Dieter Braun, Armin Scrinzi, Otmar Biebel and Michael Haack** for being part of my committee.
- **Martin Grundner** for being a great colleague and friend, for teaching me how to handle large code projects and for proof reading this thesis.
- **Sam Mardazad** for being a great colleague and friend, for all the time he spent teaching me the use of SYTEN and for proof reading this thesis.
- **Sebastian Paeckel** for being a wonderful supervisor, a friend, who always has an open ear, for our skateboarding sessions and for proof reading this thesis.
- **Nils-Oliver Linden** for introducing me to this awesome field of research and answering so many questions about DMFT.
- **Claudius Hubig** for teaching me many things about tensor networks and his patience regarding all the questions I had.
- **Manuel Zingl** for all the things he taught me about correlated materials, DFT+DMFT and the way papers are supposed to be written.
- **Jernej Mravlje** for the wonderful meetings we had and for sharing his vast knowledge about correlated materials with me.

- **Benjamin Lenz** for teaching me so much about CMDFT, for the great time we spent in Paris as well as proof reading this thesis.
- **Benjamin Bacq-Labreuil** for the discussions, the fun writing sessions, for proof reading this thesis, the awesome time in Paris and last, but not least, offering to find a duck for me.
- **Jonathan Karp** and **Andrew J. Millis** for the collaboration on  $\text{Sr}_2\text{RuO}_4$  and  $\text{Sr}_2\text{MoO}_4$  and the interesting discussions during our visit in New York.
- **Olivier Parcollet** for the hospitality and interesting discussions during the time in New York.
- **Silke Biermann** for the collaboration on t-CuO, the interesting discussions and for hosting us at École Polytechnique.
- **Inés de Vega** for being the supervisor of my master thesis, a great mentor and awesome office mate.
- **Carlos Parra** for being a great colleague, for the discussions and for the nice times we had.
- **Mattia Moroder** for many interesting discussions about Open Quantum Systems, methods to treat them as well as the fun we had during lunch breaks.
- **Felix Palm** for many interesting discussions about physics and the world and just for being fun to hang out with.
- **Héloïse Albot** and **Tizian Blatz** for interesting discussions within our subgroup seminar. Throughout the COVID years this seminar helped me a lot.
- **Cordula Weber** for being a wonderful colleague and helping me through all kinds of administrative struggles.
- **Ralph Simmler**, **Veronika Finsterwalder**, **Kalle Bamberg** and **Robert Redl** for all the help to keep our workstations and calculations running.
- my **mum**, **dad** and **brother** for their encouragement and having an open ear for me at all times. Your unwavering support meant a lot to me.
- **Janina** for supporting me since we met 11 years ago. The time we spent together was the most fulfilling time of my life and I want to thank you for always being there for me.

Furthermore, I want to thank for their financial support

- the international doctoral programme **Exploring Quantum Matter (ExQM)** within the **Excellence Network of Bavaria (ENB)**.
- the **German Research Foundation**, which supported me through the research unit **FOR1807**.



# Bibliography

- [1] M. Bramberger, B. Bacq-Labreuil, M. Grundner, S. Biermann, U. Schollwöck, S. Paeckel, and B. Lenz, (2022), [arXiv:2203.07880](#) .
- [2] M. Bramberger, J. Mravlje, M. Grundner, U. Schollwöck, and M. Zingl, [Phys. Rev. B \*\*103\*\*, 165133 \(2021\)](#).
- [3] C. A. Parra-Murillo, M. Bramberger, C. Hubig, and I. De Vega, [Phys. Rev. A \*\*103\*\*, 032204 \(2021\)](#).
- [4] J. Karp, M. Bramberger, M. Grundner, U. Schollwöck, A. J. Millis, and M. Zingl, [Phys. Rev. Lett. \*\*125\*\*, 166401 \(2020\)](#).
- [5] M. Bramberger and I. De Vega, [Phys. Rev. A \*\*101\*\*, 012101 \(2020\)](#).
- [6] F. Bloch, [Zeitschrift fur Physik \*\*52\*\*, 555 \(1929\)](#).
- [7] W. Pauli, [Zeitschrift für Physik \*\*31\*\*, 765 \(1925\)](#).
- [8] A. H. Wilson and P. A. M. Dirac, [Proceedings of the Royal Society of London. Series A, Containing Papers of a Mathematical and Physical Character \*\*133\*\*, 458 \(1931\)](#).
- [9] N. Ashcroft and N. Mermin, *Solid State Physics* (Saunders College, Philadelphia, 1976).
- [10] W. Kohn, [Rev. Mod. Phys. \*\*71\*\*, 1253 \(1999\)](#).
- [11] U. von Barth, [Physica Scripta \*\*T109\*\*, 9 \(2004\)](#).
- [12] R. O. Jones and O. Gunnarsson, [Rev. Mod. Phys. \*\*61\*\*, 689 \(1989\)](#).
- [13] P. J. Hasnip, K. Refson, M. I. J. Probert, J. R. Yates, S. J. Clark, and C. J. Pickard, [Philosophical Transactions of the Royal Society A: Mathematical, Physical and Engineering Sciences \*\*372\*\*, 20130270 \(2014\)](#).

- 
- [14] G. Kotliar, S. Y. Savrasov, K. Haule, V. S. Oudovenko, O. Parcollet, and C. A. Marianetti, *Rev. Mod. Phys.* **78**, 865 (2006).
- [15] J. Hubbard, *Proceedings of the Royal Society of London. Series A. Mathematical and Physical Sciences* **276**, 238 (1963).
- [16] S. Sachdev, *Rev. Mod. Phys.* **75**, 913 (2003).
- [17] M. Imada, A. Fujimori, and Y. Tokura, *Rev. Mod. Phys.* **70**, 1039 (1998).
- [18] A. Georges, L. de' Medici, and J. Mravlje, *Annu. Rev. Condens. Matter Phys.* **4**, 137 (2013).
- [19] G. H. Wannier, *Phys. Rev.* **52**, 191 (1937).
- [20] A. Georges, G. Kotliar, W. Krauth, and M. J. Rozenberg, *Rev. Mod. Phys.* **68**, 13 (1996).
- [21] V. I. Anisimov, A. I. Poteryaev, M. A. Korotin, A. O. Anokhin, and G. Kotliar, *Journal of Physics: Condensed Matter* **9**, 7359 (1997).
- [22] J. Kanamori, *Progr. Theor. Phys* **30**, 275 (1963).
- [23] M. C. Gutzwiller, *Phys. Rev. Lett.* **10**, 159 (1963).
- [24] A. Georges and W. Krauth, *Phys. Rev. Lett.* **69**, 1240 (1992).
- [25] K. Held, I. A. Nekrasov, G. Keller, V. Eyert, N. Blümer, A. K. McMahhan, R. T. Scalettar, T. Pruschke, V. I. Anisimov, and D. Vollhardt [10.48550/ARXIV.COND-MAT/0112079](https://arxiv.org/abs/10.48550/ARXIV.COND-MAT/0112079) (2001).
- [26] A. Georges, *AIP Conference Proceedings* **715** (2004).
- [27] E. Gull, A. J. Millis, A. I. Lichtenstein, A. N. Rubtsov, M. Troyer, and P. Werner, *Rev. Mod. Phys.* **83**, 349 (2011).
- [28] M. Caffarel and W. Krauth, *Phys. Rev. Lett.* **72**, 1545 (1994).
- [29] K. G. Wilson, *Rev. Mod. Phys.* **47**, 773 (1975).
- [30] R. Bulla, T. A. Costi, and T. Pruschke, *Rev. Mod. Phys.* **80**, 395 (2008).
- [31] U. Schollwöck, *Rev. Mod. Phys.* **77**, 259 (2005).

- [32] U. Schollwöck, [Ann. Phys.](#) **326**, 96 (2011).
- [33] F. A. Wolf, *Solving dynamical mean-field theory using matrix product states*, [Ph.D. thesis](#) (2015).
- [34] F. A. Wolf, A. Go, I. P. McCulloch, A. J. Millis, and U. Schollwöck, [Phys. Rev. X](#) **5**, 041032 (2015).
- [35] N.-O. Linden, M. Zingl, C. Hubig, O. Parcollet, and U. Schollwöck, [Phys. Rev. B](#) **101**, 041101(R) (2020).
- [36] D. Bauernfeind, M. Zingl, R. Triebl, M. Aichhorn, and H. G. Evertz, [Phys. Rev. X](#) **7**, 031013 (2017).
- [37] Y. Shi, Y. Guo, Y. Shirako, W. Yi, X. Wang, A. A. Belik, Y. Matsushita, H. L. Feng, Y. Tsujimoto, M. Arai, N. Wang, M. Akaogi, and K. Yamaura, [Journal of the American Chemical Society](#) **135**, 16507 (2013).
- [38] J. S. Griffith and L. E. Orgel, [Q. Rev. Chem. Soc.](#) **11**, 381 (1957).
- [39] E. Pavarini, [Crystal-Field Theory, Tight-Binding Method and Jahn-Teller Effect](#) (2012).
- [40] S. Sugano, Y. Tanabe, and H. Kamimura, *Multiplets of Transition-Metal Ions in Crystals*, Vol. 33 (1970) pp. 154 – 178.
- [41] L. Van Hove, [Phys. Rev.](#) **89**, 1189 (1953).
- [42] S. Åsbrink and L.-J. Norrby, [Acta Crystallographica Section B](#) **26**, 8.
- [43] W. Siemons, G. Koster, D. H. A. Blank, R. H. Hammond, T. H. Geballe, and M. R. Beasley, [Phys. Rev. B](#) **79**, 195122 (2009).
- [44] D. Samal, H. Tan, Y. Takamura, W. Siemons, J. Verbeeck, G. van Tendeloo, E. Arenholz, C. Jenkins, G. Rijnders, and G. Koster, [EPL \(Europhysics Letters\)](#) **105**, 17003 (2014).
- [45] S. Moser, L. Moreschini, H.-Y. Yang, D. Innocenti, F. Fuchs, N. H. Hansen, Y. J. Chang, K. S. Kim, A. L. Walter, A. Bostwick, E. Rotenberg, F. Mila, and M. Grioni, [Phys. Rev. Lett.](#) **113**, 187001 (2014).
- [46] A. Damascelli, Z. Hussain, and Z.-X. Shen, [Rev. Mod. Phys.](#) **75**, 473 (2003).

- 
- [47] P. A. Lee, N. Nagaosa, and X.-G. Wen, *Rev. Mod. Phys.* **78**, 17 (2006).
- [48] F. C. Zhang and T. M. Rice, *Phys. Rev. B* **37**, 3759 (1988).
- [49] S. Moser, N. E. Shaik, D. Samal, S. Fatale, B. Dalla Piazza, M. Dantz, J. Pellicciari, P. Olalde-Velasco, T. Schmitt, G. Koster, F. Mila, H. M. Rønnow, and M. Grioni, *Phys. Rev. B* **92**, 140404 (2015).
- [50] A. I. Lichtenstein and M. I. Katsnelson, *Phys. Rev. B* **62**, R9283 (2000).
- [51] G. Kotliar, S. Y. Savrasov, G. Pálsson, and G. Biroli, *Phys. Rev. Lett.* **87**, 186401 (2001).
- [52] T. Maier, M. Jarrell, T. Pruschke, and M. H. Hettler, *Rev. Mod. Phys.* **77**, 1027 (2005).
- [53] H. Shinaoka, E. Gull, and P. Werner, *Computer Physics Communications* **215**, 128 (2017).
- [54] A. N. Rubtsov, V. V. Savkin, and A. I. Lichtenstein, *Phys. Rev. B* **72**, 035122 (2005).
- [55] A. Gaenko, A. Antipov, G. Carcassi, T. Chen, X. Chen, Q. Dong, L. Gamper, J. Gukelberger, R. Igarashi, S. Isakov, M. Könz, J. LeBlanc, R. Levy, P. Ma, J. Paki, H. Shinaoka, S. Todo, M. Troyer, and E. Gull, *Computer Physics Communications* **213**, 235 (2017).
- [56] M. Potthoff, *The European Physical Journal B-Condensed Matter and Complex Systems* **32**, 429 (2003).
- [57] M. Potthoff, M. Aichhorn, and C. Dahnken, *Phys. Rev. Lett.* **91**, 206402 (2003).
- [58] M. Potthoff, *The European Physical Journal B-Condensed Matter and Complex Systems* **36**, 335 (2003).
- [59] W. Metzner and D. Vollhardt, *Phys. Rev. Lett.* **62**, 324 (1989).
- [60] A. Georges and G. Kotliar, *Phys. Rev. B* **45**, 6479 (1992).
- [61] G. Baym and L. P. Kadanoff, *Phys. Rev.* **124**, 287 (1961).
- [62] T. Plefka, *Journal of Physics A: Mathematical and General* **15**, 1971 (1982).
- [63] R. Fukuda, *Phys. Rev. Lett.* **61**, 1549 (1988).

- 
- [64] F. J. Dyson, *Phys. Rev.* **75**, 1736 (1949).
- [65] G. Baym, *Phys. Rev.* **127**, 1391 (1962).
- [66] P. W. Anderson, *Phys. Rev.* **124**, 41 (1961).
- [67] M. H. Hettler, A. N. Tahvildar-Zadeh, M. Jarrell, T. Pruschke, and H. R. Krishnamurthy, *Phys. Rev. B* **58**, R7475 (1998).
- [68] M. H. Hettler, M. Mukherjee, M. Jarrell, and H. R. Krishnamurthy, *Phys. Rev. B* **61**, 12739 (2000).
- [69] D. Sénéchal, D. Perez, and M. Pioro-Ladrière, *Phys. Rev. Lett.* **84**, 522 (2000).
- [70] D. Sénéchal, (2010), [arXiv:0806.2690](https://arxiv.org/abs/0806.2690) [cond-mat.str-el] .
- [71] D. R. Hartree, *Reports on Progress in Physics* **11**, 113 (1947).
- [72] S. R. White, *Phys. Rev. Lett.* **69**, 2863 (1992).
- [73] S. Paeckel, T. Köhler, A. Swoboda, S. R. Manmana, U. Schollwöck, and C. Hubig, *Ann. Physics* **411**, 167998 (2019).
- [74] P. A. M. Dirac, *Mathematical Proceedings of the Cambridge Philosophical Society* **26**, 376–385 (1930).
- [75] P. W. Langhoff, S. T. Epstein, and M. Karplus, *Rev. Mod. Phys.* **44**, 602 (1972).
- [76] J. Haegeman, J. I. Cirac, T. J. Osborne, I. Pižorn, H. Verschelde, and F. Verstraete, *Phys. Rev. Lett.* **107**, 070601 (2011).
- [77] J. Haegeman, C. Lubich, I. Oseledets, B. Vandereycken, and F. Verstraete, *Phys. Rev. B* **94**, 165116 (2016).
- [78] H. F. Trotter, *Proc. Amer. Math. Soc.* **10**, 545 (1959).
- [79] M. Suzuki, *Communications in Mathematical Physics* **51**, 183 (1976).
- [80] C. Hubig, F. Lachenmaier, N.-O. Linden, T. Reinhard, L. Stenzel, A. Swoboda, M. Grundner, and S. Mardazad, *The SYTEN toolkit*.
- [81] C. Hubig, *Symmetry-protected tensor networks*, *Ph.D. thesis* (2017).

- [82] N.-O. Linden, *Dynamical mean-field theory studies on real materials*, Ph.D. thesis (2019).
- [83] M. Grundner, *in preparation*, Ph.D. thesis (2022).
- [84] M. Grundner, M. Bramberger, S. Paeckel, U. Schollwöck, and S. Mardazad, (in preparation).
- [85] A. C. Hewson, Models of magnetic impurities, in *The Kondo Problem to Heavy Fermions*, Cambridge Studies in Magnetism (Cambridge University Press, 1993) p. 1–28.
- [86] D. Sénéchal, *Phys. Rev. B* **81**, 235125 (2010).
- [87] D. J. Wales and J. P. K. Doye, *The Journal of Physical Chemistry A* **101**, 5111 (1997).
- [88] API reference for `scipy.optimize.basinhopping`, <https://docs.scipy.org/doc/scipy/reference/generated/scipy.optimize.basinhopping.html>.
- [89] P. Virtanen, R. Gommers, T. E. Oliphant, M. Haberland, T. Reddy, D. Cournapeau, E. Burovski, P. Peterson, W. Weckesser, J. Bright, S. J. van der Walt, M. Brett, J. Wilson, K. J. Millman, N. Mayorov, A. R. J. Nelson, E. Jones, R. Kern, E. Larson, C. J. Carey, Í. Polat, Y. Feng, E. W. Moore, J. VanderPlas, D. Laxalde, J. Perktold, R. Cimrman, I. Henriksen, E. A. Quintero, C. R. Harris, A. M. Archibald, A. H. Ribeiro, F. Pedregosa, P. van Mulbregt, and SciPy 1.0 Contributors, *Nature Methods* **17**, 261 (2020).
- [90] API reference for `scipy.optimize.minimize`, <https://docs.scipy.org/doc/scipy/reference/generated/scipy.optimize.minimize.html>.
- [91] S. Kirkpatrick, C. D. Gelatt, and M. P. Vecchi, *Science* **220**, 671 (1983).
- [92] N. I. M. Gould, S. Lucidi, M. Roma, and P. L. Toint, *SIAM J. Optim.* **9**, 504 (1999).
- [93] J. Nocedal and S. Wright, *Numerical Optimization* (Springer-Verlag New York, 2006) pp. 73 – 77.
- [94] M. Karski, C. Raas, and G. S. Uhrig, *Phys. Rev. B* **72**, 113110 (2005).
- [95] M. Karski, C. Raas, and G. S. Uhrig, *Phys. Rev. B* **77**, 075116 (2008).

- 
- [96] T. Barthel, U. Schollwöck, and S. R. White, *Phys. Rev. B* **79**, 245101 (2009).
- [97] R. Bulla, A. C. Hewson, and T. Pruschke, *Journal of Physics: Condensed Matter* **10**, 8365–8380 (1998).
- [98] M. Aichhorn, L. Pourovskii, P. Seth, V. Vildosola, M. Zingl, O. E. Peil, X. Deng, J. Mravlje, G. J. Kraberger, C. Martins, M. Ferrero, and O. Parcollet, *Comput. Phys. Commun.* **204**, 200 (2016).
- [99] O. Parcollet, M. Ferrero, T. Ayrál, H. Hafermann, I. Krivenko, L. Messio, and P. Seth, *Comput. Phys. Commun.* **196**, 398 (2015).
- [100] TRIQS website, <https://triqs.github.io/triqs>.
- [101] J. S. Toll, *Phys. Rev.* **104**, 1760 (1956).
- [102] B. Y.-K. Hu, *American Journal of Physics* **57**, 821 (1989).
- [103] K. S. D. Beach, R. J. Gooding, and F. Marsiglio, *Phys. Rev. B* **61**, 5147 (2000).
- [104] J. Fei, C.-N. Yeh, and E. Gull, *Phys. Rev. Lett.* **126**, 056402 (2021).
- [105] J. E. Gubernatis, M. Jarrell, R. N. Silver, and D. S. Sivia, *Phys. Rev. B* **44**, 6011 (1991).
- [106] G. J. Kraberger, R. Triebl, M. Zingl, and M. Aichhorn, *Phys. Rev. B* **96**, 155128 (2017).
- [107] TRIQS/maxent website, <https://triqs.github.io/maxent>.
- [108] J. Mravlje and A. Georges, *Phys. Rev. Lett.* **117**, 036401 (2016).
- [109] A. A. Mostofi, J. R. Yates, Y.-S. Lee, I. Souza, D. Vanderbilt, and N. Marzari, *Comput. Phys. Commun.* **178**, 685 (2008).
- [110] TRIQS/DFTTools website, [https://triqs.github.io/dft\\_tools](https://triqs.github.io/dft_tools).
- [111] I. P. McCulloch and M. Gulácsi, *Europhysics Letters (EPL)* **57**, 852 (2002).
- [112] B. J. Kim, H. Jin, S. J. Moon, J.-Y. Kim, B.-G. Park, C. S. Leem, J. Yu, T. W. Noh, C. Kim, S.-J. Oh, J.-H. Park, V. Durairaj, G. Cao, and E. Rotenberg, *Phys. Rev. Lett.* **101**, 076402 (2008).

- 
- [113] C. Martins, M. Aichhorn, and S. Biermann, *Journal of Physics: Condensed Matter* **29**, 263001 (2017).
- [114] R. Triebl, G. J. Krabberger, J. Mravlje, and M. Aichhorn, *Phys. Rev. B* **98**, 205128 (2018).
- [115] C. Martins, M. Aichhorn, L. Vaugier, and S. Biermann, *Phys. Rev. Lett.* **107**, 266404 (2011).
- [116] R. Arita, J. Kuneš, A. V. Kozhevnikov, A. G. Eguiluz, and M. Imada, *Phys. Rev. Lett.* **108**, 086403 (2012).
- [117] O. N. Meetei, W. S. Cole, M. Randeria, and N. Trivedi, *Phys. Rev. B* **91**, 054412 (2015).
- [118] J. Bünemann, T. Linneweber, U. Löw, F. B. Anders, and F. Gebhard, *Phys. Rev. B* **94**, 035116 (2016).
- [119] Z. P. Yin, K. Haule, and G. Kotliar, *Nat. Mater* **10**, 932 (2011).
- [120] L. de' Medici, J. Mravlje, and A. Georges, *Phys. Rev. Lett.* **107**, 256401 (2011).
- [121] N. Lanatà, H. U. R. Strand, G. Giovannetti, B. Hellsing, L. de' Medici, and M. Capone, *Phys. Rev. B* **87**, 045122 (2013).
- [122] L. Fanfarillo and E. Bascones, *Phys. Rev. B* **92**, 075136 (2015).
- [123] K. M. Stadler, Z. P. Yin, J. von Delft, G. Kotliar, and A. Weichselbaum, *Phys. Rev. Lett.* **115**, 136401 (2015).
- [124] K. Stadler, G. Kotliar, A. Weichselbaum, and J. von Delft, *Ann. Physics* **405**, 365 (2019).
- [125] A. Horvat, R. Zitko, and J. Mravlje, (2019), [arXiv:1907.07100](https://arxiv.org/abs/1907.07100) .
- [126] M. W. Haverkort, I. S. Elfimov, L. H. Tjeng, G. A. Sawatzky, and A. Damascelli, *Phys. Rev. Lett.* **101**, 026406 (2008).
- [127] A. P. Mackenzie, S. R. Julian, A. J. Diver, G. G. Lonzarich, N. E. Hussey, Y. Maeno, S. Nishizaki, and T. Fujita, *Phys. C: Supercond.* **263**, 510 (1996).
- [128] Y. Maeno, K. Yoshida, H. Hashimoto, S. Nishizaki, S.-I. Ikeda, M. Nohara, T. Fujita, A. P. Mackenzie, N. E. Hussey, J. G. Bednorz, and F. Lichtenberg, *J. Phys. Soc. Jpn* **66**, 1405 (1997).

- [129] C. Bergemann, A. P. Mackenzie, S. R. Julian, D. Forsythe, and E. Ohmichi, *Adv. Phys.* **52**, 639 (2003).
- [130] Z. V. Pchelkina, I. A. Nekrasov, T. Pruschke, A. Sekiyama, S. Suga, V. I. Anisimov, and D. Vollhardt, *Phys. Rev. B* **75**, 035122 (2007).
- [131] D. Stricker, J. Mravlje, C. Berthod, R. Fittipaldi, A. Vecchione, A. Georges, and D. van der Marel, *Phys. Rev. Lett.* **113**, 087404 (2014).
- [132] M. Behrmann, C. Piefke, and F. Lechermann, *Phys. Rev. B* **86**, 045130 (2012).
- [133] A. Tamai, M. Zingl, E. Rozbicki, E. Cappelli, S. Riccò, A. de la Torre, S. McKeeown Walker, F. Y. Bruno, P. D. C. King, W. Meevasana, M. Shi, M. Radović, N. C. Plumb, A. S. Gibbs, A. P. Mackenzie, C. Berthod, H. U. R. Strand, M. Kim, A. Georges, and F. Baumberger, *Phys. Rev. X* **9**, 021048 (2019).
- [134] X. Deng, K. Haule, and G. Kotliar, *Phys. Rev. Lett.* **116**, 256401 (2016).
- [135] C. N. Veenstra, Z. H. Zhu, M. Raichle, B. M. Ludbrook, A. Nicolaou, B. Slomski, G. Landolt, S. Kittaka, Y. Maeno, J. H. Dil, I. S. Elfimov, M. W. Haverkort, and A. Damascelli, *Phys. Rev. Lett.* **112**, 127002 (2014).
- [136] M. Zingl, J. Mravlje, M. Aichhorn, O. Parcollet, and A. Georges, *npj Quantum Materials* **4**, 35 (2019).
- [137] E. Sarvestani, G. Zhang, E. Gorelov, and E. Pavarini, *Phys. Rev. B* **97**, 085141 (2018).
- [138] H. J. Lee, C. H. Kim, and A. Go, *Phys. Rev. B* **102**, 195115 (2020).
- [139] G. Zhang, E. Gorelov, E. Sarvestani, and E. Pavarini, *Phys. Rev. Lett.* **116**, 106402 (2016).
- [140] M. Kim, J. Mravlje, M. Ferrero, O. Parcollet, and A. Georges, *Phys. Rev. Lett.* **120**, 126401 (2018).
- [141] H. U. R. Strand, M. Zingl, N. Wentzell, O. Parcollet, and A. Georges, *Phys. Rev. B* **100**, 125120 (2019).
- [142] Y. Aiura, Y. Yoshida, I. Hase, S. I. Ikeda, M. Higashiguchi, X. Y. Cui, K. Shimada, H. Namatame, M. Taniguchi, and H. Bando, *Phys. Rev. Lett.* **93**, 117005 (2004).

- [143] J. Mravlje, M. Aichhorn, T. Miyake, K. Haule, G. Kotliar, and A. Georges, *Phys. Rev. Lett.* **106**, 096401 (2011).
- [144] X. Deng, K. M. Stadler, K. Haule, A. Weichselbaum, J. von Delft, and G. Kotliar, *Nat. Commun.* **10**, 2721 (2019).
- [145] F. B. Kugler, M. Zingl, H. U. R. Strand, S.-S. B. Lee, J. von Delft, and A. Georges, *Phys. Rev. Lett.* **124**, 016401 (2020).
- [146] G.-Q. Liu, V. N. Antonov, O. Jepsen, and O. K. Andersen., *Phys. Rev. Lett.* **101**, 026408 (2008).
- [147] P. Zheng, Y. G. Shi, A. F. Fang, T. Dong, K. Yamaura, and N. L. Wang, *Journal of Physics: Condensed Matter* **26**, 435601 (2014).
- [148] M.-C. Jung and K.-W. Lee, *Phys. Rev. B* **90**, 045120 (2014).
- [149] N. Marzari and D. Vanderbilt, *Phys. Rev. B* **56**, 12847 (1997).
- [150] I. Souza, N. Marzari, and D. Vanderbilt, *Phys. Rev. B* **65**, 035109 (2001).
- [151] J. Kuneš, R. Arita, P. Wissgott, A. Toschi, H. Ikeda, and K. Held, *Comput. Phys. Commun.* **181**, 1888 (2010).
- [152] D. Springer, B. Kim, P. Liu, S. Khmelevskiy, S. Adler, M. Capone, G. Sangiovanni, C. Franchini, and A. Toschi, *Physical Review Letters* **125**, 10.1103/physrevlett.125.166402 (2020).
- [153] T. Ribic, E. Assmann, A. Tóth, and K. Held, *Phys. Rev. B* **90**, 165105 (2014).
- [154] P. Blaha, K. Schwarz, F. Tran, R. Laskowski, G. K. H. Madsen, and L. D. Marks, *The Journal of Chemical Physics* **152**, 074101 (2020).
- [155] F. B. Kugler, S.-S. B. Lee, A. Weichselbaum, G. Kotliar, and J. von Delft, *Phys. Rev. B* **100**, 115159 (2019).
- [156] A. Horvat, R. Žitko, and J. Mravlje, *Phys. Rev. B* **96**, 085122 (2017).
- [157] H. Wadati, J. Mravlje, K. Yoshimatsu, H. Kumigashira, M. Oshima, T. Sugiyama, E. Ikenaga, A. Fujimori, A. Georges, A. Radetinac, K. S. Takahashi, M. Kawasaki, and Y. Tokura, *Phys. Rev. B* **90**, 205131 (2014).
- [158] Dai, Xi, *Mott transition in 5d compounds*.

- 
- [159] L. Du, X. Sheng, H. Weng, and X. Dai, *EPL (Europhysics Letters)* **101**, 27003 (2013).
- [160] M. Bremholm, S. Dutton, P. Stephens, and R. Cava, *Journal of Solid State Chemistry* **184**, 601 (2011).
- [161] Q. Han, H. T. Dang, and A. J. Millis, *Phys. Rev. B* **93**, 155103 (2016).
- [162] N. Dasari, S. R. K. C. S. Yamijala, M. Jain, T. S. Dasgupta, J. Moreno, M. Jarrell, and N. S. Vidhyadhiraja, *Phys. Rev. B* **94**, 085143 (2016).
- [163] M. R. Norman, *Science* **332**, 196 (2011).
- [164] B. Keimer, S. A. Kivelson, M. R. Norman, S. Uchida, and J. Zaanen, *Nature* **518**, 179 (2015).
- [165] M. R. Norman and C. Pépin, *Reports on Progress in Physics* **66**, 1547 (2003).
- [166] T. Timusk and B. Statt, *Reports on Progress in Physics* **62**, 61 (1999).
- [167] P. W. Anderson, *Science* **235**, 1196 (1987).
- [168] J. Zaanen, G. A. Sawatzky, and J. W. Allen, *Phys. Rev. Lett.* **55**, 418 (1985).
- [169] V. J. Emery, *Phys. Rev. Lett.* **58**, 2794 (1987).
- [170] O. Andersen, A. Liechtenstein, O. Jepsen, and F. Paulsen, *Journal of Physics and Chemistry of Solids* **56**, 1573 (1995).
- [171] M. Hirayama, Y. Yamaji, T. Misawa, and M. Imada, *Phys. Rev. B* **98**, 134501 (2018).
- [172] H. Eskes, L. H. Tjeng, and G. A. Sawatzky, *Phys. Rev. B* **41**, 288 (1990).
- [173] G. Peralta, D. Puggioni, A. Filippetti, and V. Fiorentini, *Phys. Rev. B* **80**, 140408 (2009).
- [174] X.-Q. Chen, C. L. Fu, C. Franchini, and R. Podlucky, *Phys. Rev. B* **80**, 094527 (2009).
- [175] C. Franchini, X.-Q. Chen, and R. Podlucky, *Journal of Physics: Condensed Matter* **23**, 045004 (2010).

- 
- [176] W. Fang-Fang, P. Wei, D. Xue-Yong, X. Xian-Ran, and X.-Q. Chen, *Chinese Physics Letters* **31**, 027402 (2014).
- [177] P. Grant, *Journal of Physics: Conference Series* **129**, 012042 (2008).
- [178] G. Drera, A. Giampietri, A. Febbrari, M. Patrini, M. C. Mozzati, and L. Sangaletti, *Phys. Rev. B* **99**, 075124 (2019).
- [179] K. S. Rabinovich, L. L. Samoilenko, A. S. Zhuravleva, and A. G. Shneider, *Applied Physics Letters* **104**, 182406 (2014).
- [180] B. X. Yang, T. R. Thurston, J. M. Tranquada, and G. Shirane, *Phys. Rev. B* **39**, 4343 (1989).
- [181] C. P. J. Adolphs, S. Moser, G. A. Sawatzky, and M. Berciu, *Phys. Rev. Lett.* **116**, 087002 (2016).
- [182] I. J. Hamad, L. O. Manuel, and A. A. Aligia, *Phys. Rev. Lett.* **120**, 177001 (2018).
- [183] F. A. Wolf, I. P. McCulloch, O. Parcollet, and U. Schollwöck, *Phys. Rev. B* **90**, 115124 (2014).
- [184] F. A. Wolf, I. P. McCulloch, and U. Schollwöck, *Phys. Rev. B* **90**, 235131 (2014).
- [185] D. Bauernfeind, R. Triebl, M. Zingl, M. Aichhorn, and H. G. Evertz, *Phys. Rev. B* **97**, 115156 (2018).
- [186] I. M. Lifshitz, *Soviet Physics JETP* **11**, 1130 (1960).
- [187] C. Martins, B. Lenz, L. Perfetti, V. Brouet, F. m. c. Bertran, and S. Biermann, *Phys. Rev. Materials* **2**, 032001 (2018).
- [188] B. Lenz, C. Martins, and S. Biermann, *Journal of Physics: Condensed Matter* **31**, 293001 (2019).
- [189] A. Louat, B. Lenz, S. Biermann, C. Martins, F. Bertran, P. Le Fèvre, J. E. Rault, F. Bert, and V. Brouet, *Phys. Rev. B* **100**, 205135 (2019).
- [190] S. Moser, *Journal of Electron Spectroscopy and Related Phenomena* **214**, 29 (2017).

- 
- [191] N. D. Mermin and H. Wagner, *Phys. Rev. Lett.* **17**, 1133 (1966).
- [192] T. Sato and H. Tsunetsugu, *Phys. Rev. B* **94**, 085110 (2016).
- [193] D. Sénéchal, in *2008 22nd International Symposium on High Performance Computing Systems and Applications* (2008) pp. 9–15.
- [194] M. Potthoff, in *DMFT at 25: Infinite Dimensions*, Vol. 4 (2014) pp. 271–308.
- [195] A. H. Nevidomskyy, C. Scheiber, D. Sénéchal, and A.-M. S. Tremblay, *Phys. Rev. B* **77**, 064427 (2008).
- [196] S. R. Hassan, B. Davoudi, B. Kyung, and A.-M. S. Tremblay, *Phys. Rev. B* **77**, 094501 (2008).
- [197] L. P. Gor'kov, *Soviet Physics JETP* **7(3)**, 735 (1958).
- [198] Y. Nambu, *Phys. Rev.* **117**, 648 (1960).
- [199] B. Lenz, *Unconventional Phases in Two-Dimensional Hubbard and Kondo-Lattice Models by Variational Cluster Approaches*, *Ph.D. thesis* (2017).
- [200] T. Köhler, J. Stolpp, and S. Paeckel, *SciPost Phys.* **10**, 58 (2021).